New Insights into cyclic GMP-AMP Signaling in Innate Immunity

Shivam A. Zaver

A dissertation submitted in partial fulfillment of the
requirements for the degree of

Doctor of Philosophy

University of Washington

2021

Reading Committee:

Joshua J. Woodward, Chair, Michael Lagunoff & Stephen J. Tapscott

Program Authorized to Offer Degree:

Molecular and Cellular Biology

University of Washington

ABSTRACT

New Insights into cyclic GMP-AMP Signaling in Innate Immunity

Shivam A. Zaver

Chair of the Supervisory Committee:
Joshua J. Woodward
Department of Microbiology

Second messengers are small molecules that orchestrate cellular changes in the face of altered environmental conditions. Signal transduction is mediated through the action of protein receptors whose function is modulated by second messenger binding, resulting in altered transcriptional, translational, and post-translational processes. Over the past decade, cyclic dinucleotides (CDNs) have emerged as ubiquitous second messengers in all three domains of life, where they regulate a myriad of physiological processes. Among these roles, cyclic dinucleotide signaling systems display evolutionarily conserved roles in the control of pathogen infection in both prokaryotes and eukaryotes. In response to pathogen infection, cGAS/DncV-like nucleotidyltransferases synthesize diverse cyclic oligonucleotide products which activate effector proteins to terminate the infection. Of these effectors, the receptor STING has emerged as a conserved effector protein in both prokaryotic and eukaryotic immune systems. In prokaryotes, STING domains are found fused to NAD^+ hydrolyzing TIR domains as well as putative transmembrane domains (TM). Upon engaging CDNs, STING-TIR depletes cellular NAD^+ stores resulting in loss of viability of the infected cell and termination of bacteriophage infection. In eukaryotes, STING domains contain an N-terminal transmembrane domain required for ER localization and a loosely structured C-terminal tail required for downstream signaling. Upon engaging CDNs, metazoan STING homologs trigger autophagy and downstream innate immune signaling programs to sterilize the cytosol of the infected host cell and to restrict further pathogen replication and spread. In addition to controlling pathogen infection, STING signaling systems also play key roles in restricting tumor development as well as in the pathogenesis of acquired and hereditary autoinflammatory diseases. For these reasons, there is immense interest in designing novel therapeutics that target the cGAS-STING pathway for use as immune adjuvants and treatments for various inflammatory disease processes. In this work, we leverage the latest advances in CRISPR-interference technology to identify the first metazoan transporter of cyclic dinucleotides. Next, we develop the first FRET-based biosensor for the cyclic dinucleotide 2’3’-cGAMP enabling the real time, in vitro and in vivo detection of cGAMP signaling. Finally, we develop a high throughput quantification assay for the bacterial cyclic dinucleotide 3’3’-c-di-AMP and leverage this technology to quantify the bacterial immune signaling molecule 3’3’-cGAMP. In total, the biological process uncovered in this work have important implications for cancer immunotherapy, vaccine development, host responses to pathogen infection, and the pathogenesis of autoimmune diseases. Moreover, the technologies outlined in this work will enable previously intractable questions in the fields of prokaryotic and eukaryotic innate immune signaling and will likely facilitate fundamental discoveries in CDN biology for years to come.

This is for my parents.

Table of Contents

List of Figures and Tables

Chapter 1

Chapter 2

Chapter 3

Chapter 4

Acknowledgements

I would like to thank my graduate mentor, Dr. Joshua J. Woodward, for giving me the opportunity to carry out my graduate studies in his lab. Josh gave me the creative freedom to pursue the projects that I was excited about and in the process nurtured my development as an independent scientist. Josh was ever kind, patient, understanding and supportive throughout the ups and downs of every project. Thank you for entertaining all of my wild ideas. I also want to thank Josh for fostering a kind and collaborative laboratory environment where everyone could work together to push our scientific endeavors forward. I would like to thank all of the members of the Woodward lab past and present especially Dr. Tu Anh Huynh, Dr. Adelle McFarland, Alex Pollock, Hannah Tabakh and Dr. Melissa Locke. I could not have survived graduate school without you. I will cherish all of my times in the laboratory with you, and I am excited to see where all of your careers will take you.

I would like to thank my first scientific mentor, Dr. Kislay Parvatiyar. Kislay introduced me to the field of innate immune signaling and cyclic dinucleotide biology, which became the basis for my graduate thesis. Thank you for sharing your infectious passion for innate immunity with me. I could not have gotten to where I am today without you. I always look forward to our bimonthly phone calls, which somehow always end up lasting for hours. I'm excited to see where your career as an independent investigator will take you.

I would also like to thank all of the other graduate students, postdocs, and faculty in the Department of Microbiology and University of Washington who have helped to guide and train me over the years, beginning with all of my committee members: Dr. Daniel B. Stetson, Dr. Michael Lagunoff, Dr. Stephen J. Tapscott, and Dr. Ram Savan. I want to thank you all for keeping me grounded throughout graduate school and for your unwavering support. I would especially like to thank Dr. See-Yeun Ting for his technical advice and assistance over the past four years. You were always kind and generous with your time no matter how big or small my problem. To my graduate student colleagues in the University of Washington MSTP and departments of Microbiology and Molecular and Cellular Biology, I want to thank you all for welcoming me with open arms and giving me a community within the graduate school. You all have helped to make the past four years fly by. Our work benefited from the generosity of many labs throughout the School of Medicine. I would like to thank the labs of Drs. Joseph Mougous, Michelle Reniere, Sam Miller, Michael Lagunoff, Jason Smith, Pradeep Singh, Matt Parsek, Dan Stetson, Ram Savan, David Veesler, and Keith Elkon for kindly providing equipment and reagents to help support the work in this thesis.

My acknowledgements cannot be complete without thanking my family. To my parents, thank you for sacrificing everything to allow me to pursue my passions. My father trained in biochemistry and medicine, and my mother trained in microbiology. Unfortunately, life got in the way and they had to put their career goals aside to provide for me and my brother. Tragically, my father passed away after a year and a half long struggle with cancer shortly after I began graduate school. I hope that I am able to complete your stories through my MD PhD training. I could not have gotten to where I am today without my grandmother who poured her life into raising me. I would also like to thank the rest of my family for supporting my passions and helping me to get where I am today. Finally, I would like to thank my partner for her kindness and support through all of my

accomplishments and disappointments. You are meticulous and talented in all your endeavors, and I am grateful to have you in my life. I am excited to see what the future holds for both of us.

Lastly, I would like to acknowledge all of the funding sources that have supported my training in the Woodward lab. I personally received funding from the Seattle ARCS foundation, as well as grants from the University of Washington/Fred Hutchinson Cancer Research Center Viral Pathogenesis Training Program (2T32AI083203), the University of Washington Medical Scientist Training Program (2T32GM007266), and a Ruth L. Kirschstein Predoctoral Fellowship (1F30CA239659-01A1). My work in the Woodward lab was supported by National Institutes of Health Grants 5R01AI139071-02, 1R21AI137758-01 and 1R21AI153820-01.

Chapter 1

Cyclic Dinucleotides at the Forefront of Innate Immunity

The majority of this chapter was published in:

Zaver, S. A. & Woodward, J. J. Cyclic dinucleotides at the forefront of innate immunity. *Current Opinion in Cell Biology* **63**, 49–56 (2020).

Summary

Cyclic dinucleotides (CDNs) have emerged as ubiquitous signaling molecules in all domains of life. In eukaryotes, CDN signaling systems are evolutionarily ancient and have developed to sense and respond to pathogen infection. On the other hand, dysregulation of these pathways has been implicated in the pathogenesis of autoimmune diseases. Thus, CDNs have garnered major interest over recent years for their ability to elicit potent immune responses in the eukaryotic host. Similarly, ancestral CDN-based signaling systems also appear to confer immunological protection against infection in prokaryotes. Therefore, a better understanding of the host processes regulated by CDNs will be of tremendous value in many areas of research. In this chapter, we aim to review the latest discoveries and recent trends in CDN research with a particular focus on the molecular mechanisms by which these small molecules mediate innate immunity.

Introduction

Immunity is the physiological process whereby organisms detect and defend themselves against disease by infectious agents. Within this working definition, the immune system has classically been divided into two branches: the innate arm and the adaptive arm. In contrast to adaptive or acquired immune defenses, which are often delayed and involve genetic rearrangement events, innate immunity is considered the first and immediate line of defense against invading pathogens[1]. This is accomplished by a suite of invariant, germline-encoded receptors that recognize general, conserved, molecular features of infectious agents that are rarely or never found in the healthy host and, hence, does not confer any lasting, immunological memory[1]. Upon sensing the infectious insult, receptors of the immune system must then relay signals to effector proteins, culminating in pathogen elimination. In the context of innate immunity, this is often mediated by the employment of second messengers—small molecules that orchestrate key shifts in cellular function in response to altered environmental conditions. An emerging paradigm in prokaryotic and eukaryotic innate immune systems is the use of cyclic dinucleotide (CDN) second messengers[2–6]. As their name implies, CDNs are heterocyclic compounds synthesized by cyclases or nucleotidyltransferases (NTases) through the cyclization of two ribonucleoside triphosphate moieties via two "canonical" (3′,5′) and/or "noncanonical" (2′,5′) phosphodiester linkages. CDN signaling is resolved by the tightly regulated action of phosphodiesterase enzymes (PDEs), which catalyze the metal-dependent hydrolysis of one or both phosphodiester bonds, yielding a linear (pNpN) dinucleotide intermediate or two nucleoside monophosphates, respectively.

While a number of CDN-based signaling systems have been identified to date (reviewed in detail by Krasteva and Sondermann[7]), innate immune sensing of pathogen infection is mediated by a conserved family of NTases, including the dinucleotide cyclase in *Vibrio cholerae* (DncV) and its metazoan homolog cyclic GMP-AMP synthase (cGAS)[4,6,8,9]. This family of proteins was hence given the name cGAS/DncV-like nucleotidyltransferases (CD-NTases)[9]. Upon activation, CD-NTases catalyze the synthesis of CDN second messengers, including cyclic GMP-AMP (cGAMP), which function as immune "alarmones" produced in the context of pathogen infection. Notably, prokaryotic 3′3′-CDNs (c[N(3′,5′)pN(3′,5′)p]) contain two "canonical" (3′,5′) phosphodiester linkages; however, as this signaling system emerged in eukaryotes, it eventually transitioned to the use of 2′3′-cGAMP (c[G(2′,5′)pA(3′,5′)p]) containing mixed phosphodiester bonds in higher metazoans including humans[7,10–12]. While the biochemical underpinnings for this transition still

remain unclear, it is intriguing to hypothesize that this may afford some degree of immune discrimination between exogenous and endogenous sources of CDNs in higher eukaryotes. Despite this dissimilarity, cGAMP-based signaling systems constitute an ancient immune signaling pathway with evolutionary origins in prokaryotes[6]. This chapter will highlight the most recent discoveries and emerging themes in CDN-based innate immune signaling with an emphasis on CDN effectors, the regulation of CDN levels, and the strategies used by viruses to subvert this important signaling axis.

A broad family of CD-NTases in bacteria synthesizes diverse nucleotide second messengers

cGAS and DncV are the founding members of a large class of nucleotidyltransferases in both prokaryotes and eukaryotes. Whereas, the evolutionary origins of cGAS in metazoans can be traced as far back as the sea anemone, Nemostella vectensis, CD-NTases have recently been found in more than 10% of bacterial genomes spanning nearly every bacterial phylum, including human commensal and pathogenic microorganisms[6,9,13,14]. Although these enzymes are divergent at the amino acid level, they display common structural features including a DNA polymerase β-like nucleotidyltransferase fold[9]. Unlike other CDN cyclase families, CD-NTases display extreme diversity in their capacity to synthesize cyclic dinucleotides; moreover, cyclic trinucleotide products have also been observed including cyclic AMP-AMP-GMP produced by a CD-NTase from Enterobacter cloacae[9]. In addition to utilizing purines, bacterial CD-NTases can synthesize a number of pyrimidine containing 3′3′-CDNs, including c-di-UMP and cyclic UMP-CMP, as well as pyrimidine-purine hybrids (cyclic UMP-AMP and cyclic UMP-GMP)[9]. Although synthetic pyrimidine-based CDNs have been described, pyrimidine containing nucleotide second messengers have not been observed anywhere else in nature[15,16]. Intriguingly, a CD-NTase from *A. baumannii*, CdnD, synthesizes a cyclic trinucleotide product containing mixed 3',5' and 2',5' phosphodiesterase linkages, suggesting that 2'3'-cGAMP signaling may have directly been transferred to metazoans[17]. Remarkably, the substrate specificity of these enzymes can be reprogrammed by single amino acid substitutions within the active site lid[9]. Such plasticity in CD-NTases may have conferred a fitness advantage, for example in the context of evolutionary arms races between bacteria and the phages that infect them.

CD-NTases and Innate Anti-phage Immunity

In bacteria, CD-NTases are found within the genomic context of a cyclic oligonucleotide-based antiphage signaling system (CBASS) comprised of a core CD-NTase-effector unit and two accessory proteins with domains commonly found in eukaryotic ubiquitination machinery, including an E1/E2-containing enzyme and a JAB de-ubiquitinase[6,13]. CBASS systems confer marked resistance against a wide array of DNA-phages in a manner dependent on both CD-NTase and effector enzyme activity[6]. Interestingly, the accessory proteins appear to be conditionally essential during infection with select phages, raising the intriguing possibility that these proteins may counteract viral immune evasion strategies[6]. Similar to metazoans, CD-NTase enzymatic activity appears to be triggered by bacteriophage infection as 3′3′-cGAMP is undetectable in uninfected cells[4,6]. The ligand and/or activation mechanism for bacterial CD-NTases remains to be fully elucidated, but because bacteria do not compartmentalize their DNA, it is unlikely to be viral nucleic acids as is the case for metazoan CD-NTases[4]. Intriguingly, some CD-NTases appear

to become activated following recognition of specific, bacteriophage peptide motifs by Hop1, Rev7, and Mad2 (HORMA) domain containing receptors[18]. Although several, nonredundant 3′3′-cGAMP-selective PDEs have been identified in V. cholerae, the roles of these enzymes, if any, in CBASS signaling are unclear[19]. One possibility is that PDEs may function as a rheostat to control CBASS activation; alternatively, because canonical CBASS signaling ultimately results in cell death, as discussed below, resolution of CDN signaling may not be necessary.

A number of CBASS effector proteins have been identified, but the best characterized effector to date is a CDN-activated patatin-like phospholipase originally identified in V. cholerae and hence given the name CapV (Figure 1.1)[6,20]. Upon activation by 3′3′-CDNs, CapV-like phospholipases hydrolyze phospholipids in the bacterial inner cell membrane resulting in loss of membrane integrity and cell lysis[6,20]. Thus, the CD-NTase-phospholipase signaling axis constitutes a "cellular suicide" program intended to protect the bacterial community through abortive phage infection[6]. In lieu of a phospholipase, a number of alternative effectors have been identified in CBASS systems, including HNH-type endonucleases, a membrane spanning protein, a domain of unknown function, as well as a toll interleukin receptor (TIR) domain, which also appear to mediate innate antiphage immunity[6,18,21].

Interestingly, in a few cases, the CBASS systems contain a hybrid effector containing an N-terminal TIR domain fused to a C-terminal domain resembling the metazoan cGAMP effector stimulator of interferon genes or STING (see below)[6,22–24]. In plant and animal immune systems, TIR domains hydrolyze β–nicotinamide adenine dinucleotide molecules (NAD^+) to nicotinamide and adenine diphosphate ribose[25]. Activation of NAD^+ hydrolysis by TIR domain containing PRRs results in cell death of infected cells and restriction of pathogen infection[25]. Similarly, upon CBASS activation, prokaryotic STING-TIR homologs oligomerize and deplete cellular NAD^+ resulting in loss of viability of the infected cell[26]. In addition to TIR domains, STING sensor domains have also been found fused to putative transmembrane domains[26]. Although the mechanisms of STING-TM proteins in CBASS-mediated immunity have not been elucidated, it is likely that these proteins form membrane pores following activation resulting in dissipation of cellular ion gradients and subsequent cell death. Interestingly, STING-TIR homologs have been found in some metazoan species including the Pacific oyster *Crassostrea gigas*[26]. Thus, it is possible that metazoan cGAS-cGAMP-STING signaling systems originated from these ancestral bacterial CBASS systems and have retained their role in innate antiviral defense along the way.

cGAS-STING–mediated innate immune responses

As CD-NTase–based innate immune systems made their way into eukaryotes, they increasingly became specialized to detect foreign nucleic acid species as is the case for cGAS, a double-stranded (ds)DNA sensor, and its homolog 2′-5′ oligo-adenylate synthase, a dsRNA sensor[4,9]. Upon engaging foreign or mislocalized self dsDNA species, cGAS oligomerizes and forms phase-separated droplet-like structures that function as "microreactors" for the production of 2′3′-cGAMP[27–30]. This ultimately activates the ER-resident, transmembrane effector STING (also known as TMEM173, MITA, ERIS, and MPYS)[4,5,22,23]. Structurally, STING consists of an N-terminal four-pass transmembrane domain followed by a cytosolic CDN binding domain and a loosely structured C-terminal tail (CTT)[22]. In addition to binding 2′3′-cGAMP, STING can also recognize 3′3′-CDNs of bacterial origin including 3′3′-cGAMP, 3′3′-c-di-AMP, and 3′3′-c-di-

GMP, albeit with reduced affinities; pyrimidine-containing CDNs appear to be much weaker inducers of STING-mediated responses[7,9,15,24].

Unlike in prokaryotes where CDNs promote anti-phage immunity at the posttranslational level, in metazoans, CDN-mediated activation of STING fosters innate antimicrobial immunity through both posttranslational and transcriptional responses. In the inactive state, STING is held in an autoinhibited state by its CTTs[31]. Upon engaging CDNs, the CTTs of STING are released thereby exposing a polymerization interface that triggers the formation of STING homo-oligomers, which are stabilized further by intermolecular disulfide bonds[31,32]. Activated STING eventually traffics to a perinuclear compartment, where exposure of the CTTs subsequently facilitates the recruitment, activation, and oligomerization of the kinase, tank-binding kinase 1 (TBK1)[33,34]. Finally, the phosphorylation of STING on its CTT at a conserved motif by TBK1 recruits the transcription factor, interferon regulatory factor 3 (IRF3), resulting in its subsequent phosphorylation and activation[33,34]. IRF3 then dimerizes and translocates to the nucleus where it induces the expression of type I interferons and other innate immune gene programs to restrict viral replication and spread (Figure 1.2).

As mentioned above, cGAS-STING signaling systems in eukaryotes can be found as far back as early metazoans, including the sea anemone, *N. vectensis*[14]. Interestingly, *nv*STING was shown to lack the CTT domain required for signaling by TBK1, hinting at the possibility of interferon-independent functions of the CDN-STING axis[14,35,36]. It is now apparent that this evolutionarily ancient function of STING is the transcription-independent induction of autophagy, a process that allows the cell to remove cytosolic pathogens, including viruses and bacteria[36–38]. Indeed, STING-induced autophagy is sufficient to promote the clearance of cytosolic DNA and herpes-simplex virus-1 (HSV-1); interestingly, full-length STING displays a much stronger antiviral activity, suggesting that interferons may cooperate with autophagy to restrict viral infection (Figure 1.2)[36].

In addition to inducing autophagy, STING is a functionally plastic immune-signaling scaffold, the downstream signaling specificity of which can be modified through discrete signaling modules linearly organized along its CTT[39]. Interestingly, the STING-CTT domains found in higher vertebrates only contain modules for recruiting TBK1 and IRF3 and, thus, inducing type I interferons[39]. On the other hand, the CTT of STING from ray-finned fish has undergone an expansion to include modules to recruit and activate TNF receptor-associated factor 6 (TRAF6) to promote signaling by nuclear factor kappa-light-chain-enhancer of activated B cells (NFkB), a transcription factor that induces the expression of proinflammatory cytokines[39]. It has been postulated that acquisition of the TRAF6-module may have provided a strong selective advantage in ray-finned fish, perhaps against a pathogen that is not well controlled by type I interferons[39]. It remains to be understood why higher vertebrates including humans lack this signaling module.

2′3′-cGAMP transporters and phosphodiesterases

One advantage of second messenger signaling systems is that they allow for the amplification of input signals. In higher eukaryotes, this is of particular significance as cyclic dinucleotides can potentially function as “alarmones” or “immunotransmitters” to signal the threat of infection to neighboring cells. Indeed, 2′3′-cGAMP can be transferred to neighboring “bystander” cells through gap-junctions as well as by being packaged into virions[40–42]. In addition to direct transfer,

2′3′-cGAMP can also be secreted into the extracellular milieu, where it can be sensed by patrolling immune cells[43,44]. This was recently shown to be important for restricting tumor growth *in vivo* through the activation of tumor-associated natural killer (NK) and dendritic cells[43,44]. While the mechanism of 2′3′-cGAMP export are still unclear, the reduced folate carrier, also known as SLC19A1, moonlights as an importer of CDNs in human immune cells[45,46]. SLC19A1 appears to indiscriminately transport all CDNs tested, and this may be of importance for the field of tumor immunotherapy, where nonhydrolyzable CDNs are currently being developed and tested[45,46]. Interestingly, SLC19A1 does not appear to be the sole CDN transporter as *SLC19A1*-deficient cells can still respond to exogenous CDNs, albeit to a lesser extent[45,46]. Indeed, the volume regulated anion channel (LRRC8) was recently shown to facilitate cGAMP transport in *SLC19A1*-deficient human macrophages as well as in human vasculature cells and several different murine cell types[47,48]. In addition to facilitating cGAMP influx, LRRC8 channels also permit cGAMP efflux[47,48]. A role for P2X7R channels in cGAMP influx was also recently demonstrated; however, as these channels are primarily small ion channels, it is possible that this effect is indirect[49]. Follow-up studies will be necessary to identify the other CDN transporter(s) and to elucidate the role (if any) of cGAMP transport in the control of viral infection and tumorigenesis.

CDN export also provides a unifying mechanism for resolution of 2′3′-cGAMP signaling in higher metazoans[44]. Indeed, the catalytic domain of the only known mammalian 2′3′-cGAMP PDE, ectonucleotide pyrophosphatase phosphodiesterase 1 or ENPP1, is found in the extracellular space either as a transmembrane protein or as a soluble secreted factor[50,51]. Thus, 2′3′-cGAMP secretion may function to promote infiltrating immune cell activation as well as to return 2′3′-cGAMP levels to preinduction homeostasis through ENPP-1-mediated degradation (Figure 1.3)[43,44,50,51]. While ENPP1 appears to be the major cGAMP hydrolase in mammals, a new class of 2′3′-cGAMP-selective phosphodiesterases was recently identified in some lower metazoans. These enzymes were initially identified in mammalian poxviruses and were hence given the name poxvirus immune nucleases or poxins[52]. Subsequent bioinformatic analysis then identified poxin homologs with conserved 2′3′-cGAMP hydrolase activity in the genomes of insects, particularly moths and butterflies[52]. Interestingly, poxin homologs can also be found in the alphabaculoviruses that infect these insect hosts, raising the intriguing hypothesis that poxins may have been domesticated by these viruses and eventually transferred to pathogenic, mammalian viruses to antagonize the cGAS-STING pathway[52].

Viral evasion of cGAMP-STING signaling

While cGAMP is critical for controlling virus infection, many viruses appear to have developed countermeasures including degradation mechanisms to evade this signaling system, highlighting the evolutionary arms race that exists between viruses and their hosts[53–62]. One such strategy, commonly employed by herpesviruses, is to limit cGAMP production by inhibiting cGAS activation[55–58]. This can be accomplished through the use of tegument proteins that directly bind to cGAS and trigger its dissociation from viral DNA as is the case for Kaposi-sarcoma herpesvirus and human cytomegalovirus[55–57]. Interestingly, HSV-1 has developed a sophisticated strategy for the species-specific inhibition of cGAS-signaling involving the tegument protein, UL37[58]. Mechanistically, UL37 was found to possess deamidase activity, which allows it to inactivate cGAS through the deamidation of a single asparagine residue on its activation loop[58]. Interestingly,

UL37 can deamidate mouse and human cGAS isoforms but not isoforms from non-human primates, again underscoring how evolutionary arms races may specify host tropism[58]. Thus, direct targeting of cGAS appears to be a common strategy employed by herpesviruses to evade host DNA-sensing pathways. While we aimed to highlight some of the recent publications and common themes, this is certainly not an exhaustive list of the strategies used by DNA viruses to evade cGAMP-STING signaling, some of which involve directly antagonizing STING (for a more detailed review on this topic please see Ni et al.)[59–62]. It is possible that the mechanisms for bystander cell activation discussed above may have developed out of a necessity to counteract these viral immune evasion strategies in infected cells. It will be interesting to see whether bacteriophages may employ similar mechanisms for evading CBASS-mediated immunity, perhaps through use of poxin homologs.

Concluding remarks

In summary, CD-NTase signaling networks constitute an evolutionarily ancient form of innate antiviral defense originating as prokaryotic antiphage systems. It is possible that as bacteria fused with archaea, they brought along these antiviral defense mechanisms ultimately giving rise to the cGAS-STING pathway in metazoans as we know it today. Although pathogens have developed strategies to evade these signaling systems, sensing of foreign and damaged or misplaced-self DNA species by the enzyme cGAS has proven to be essential for the control of pathogen infection and tumorigenesis, respectively, both in vitro and in vivo. Although much is now known about the mechanisms of cGAS and STING activation, as cGAS indiscriminately binds DNA, a more thorough understanding of self-versus non–self-discrimination by cGAS will be necessary. Several recent studies have begun to shed light on this process, which will likely be an active area of research over the coming years[63–68]. Indeed, cyclic dinucleotides are a rapidly expanding class of signaling molecules in all domains of life with many exciting biological roles to be uncovered ahead.

Figures

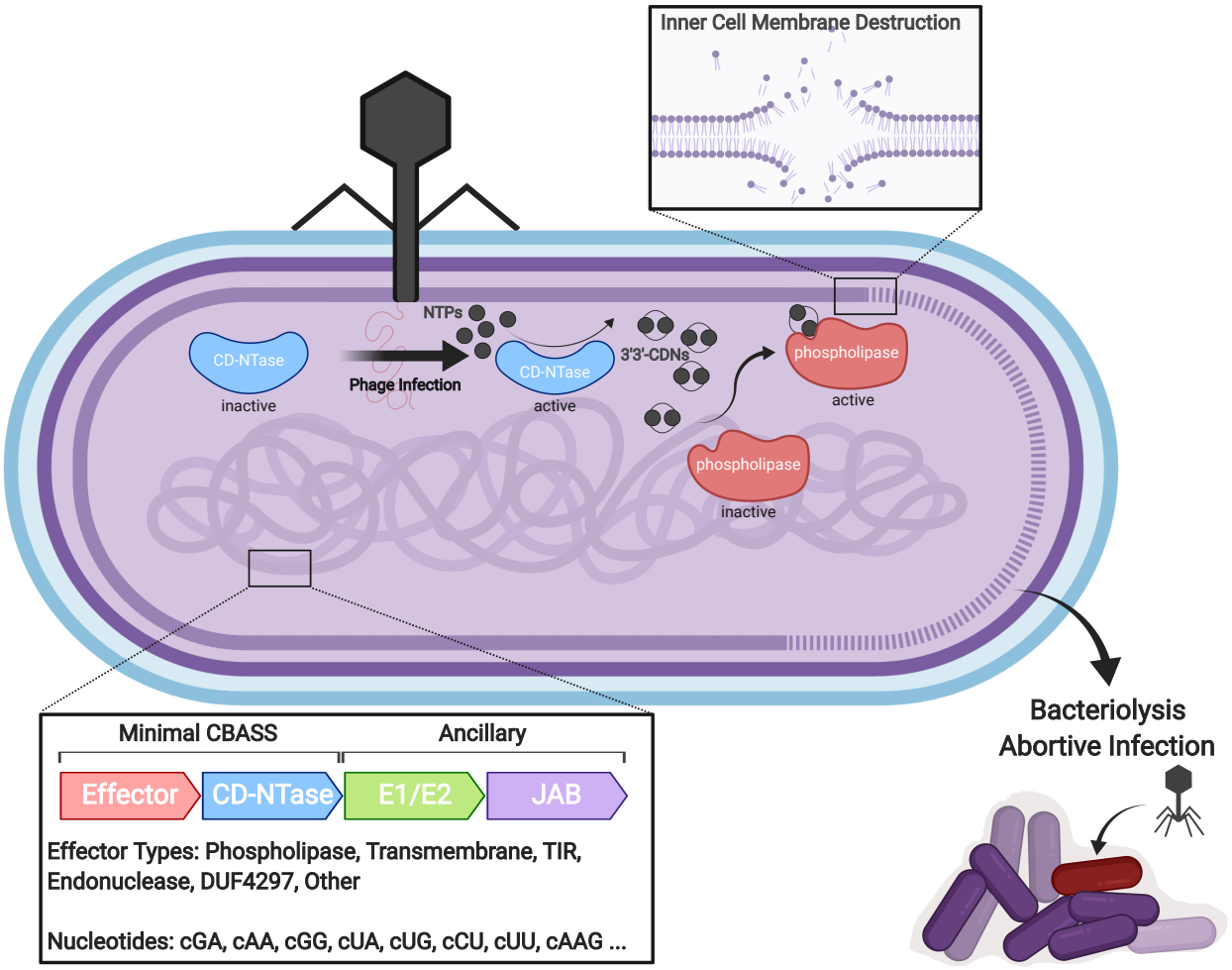

Figure 1.1: Overview of CBASS signaling.
Following bacteriophage infection, activation of CD-NTases results in the production of diverse cyclic oligonucleotide species (cNNs or cNNNs, where N is any NMP) including 3′3′-CDNs. Binding of 3′3′-CDNs to a latent phospholipase results in its activation and the subsequent hydrolysis of the bacterial inner cell membrane. Dissolution of the inner membrane results in bacteriolysis, abortive infection, and ultimately protection of the larger bacterial community. Alternative CBASS effectors include endonucleases, transmembrane effectors, Toll interleukin receptor (TIR)-like effectors, domains of unknown function (DUFs), among others, although these are less well characterized. CBASS, cyclic oligonucleotide-based antiphage signaling system; CD-NTase, cGAS/DncV-like nucleotidyltransferases; CDNs, cyclic dinucleotides

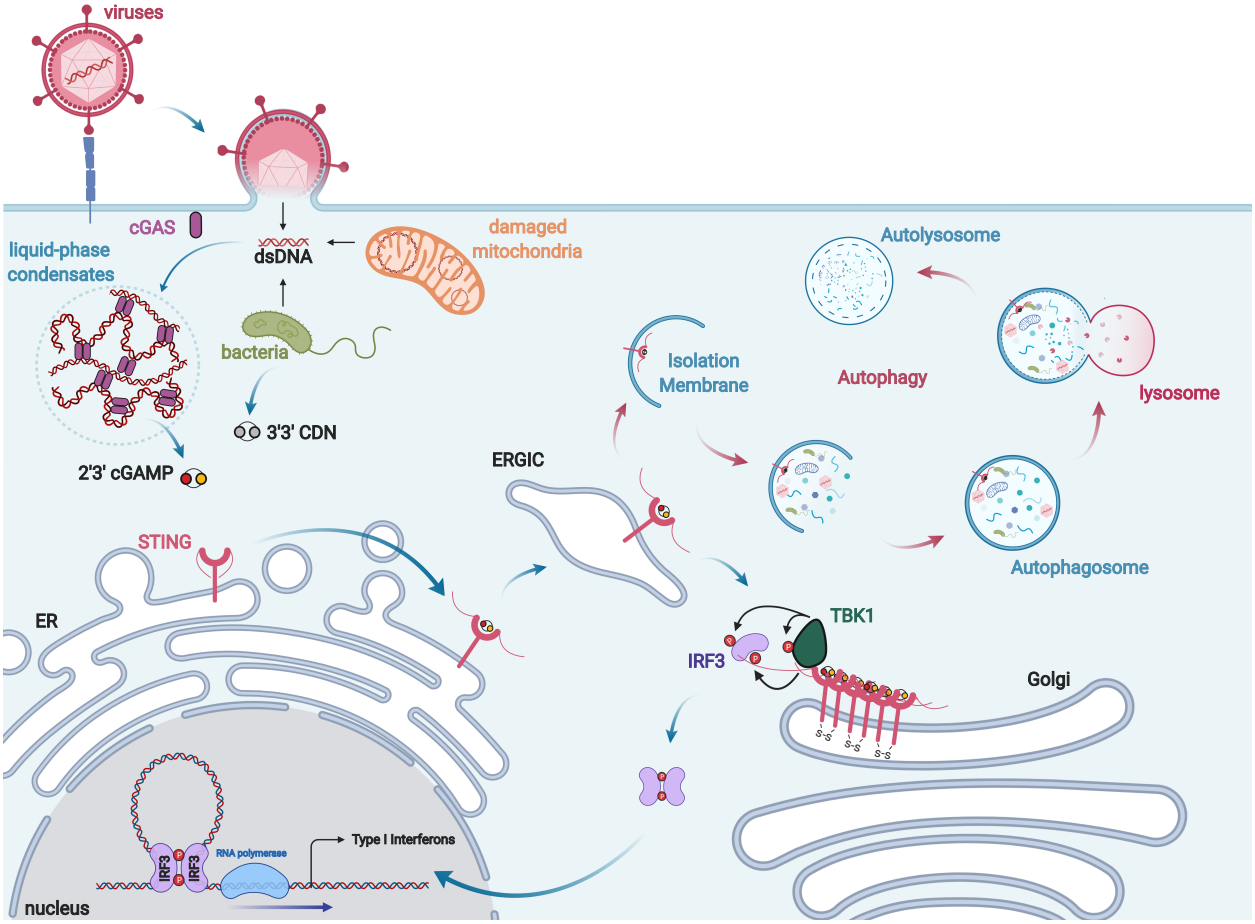

Fig. 1.2: Schematic of the cGAS-cGAMP-STING signaling axis.
Accumulation of pathogenic or mislocalized self dsDNA species in the host cell cytosol activates cGAS, resulting in the formation of cGAS-DNA liquid-phase condensates and the production of 2′3′-cGAMP. Binding of 2′3′-cGAMP or 3′3′-CDNs from bacterial sources to STING results in its activation culminating in STING oligomerization and translocation to the perinuclear Golgi. There STING recruits the kinase TBK1 to the transcription factor IRF3 via its C-terminal tails ultimately resulting in IRF3 phosphorylation, dimerization, and nuclear translocation. In the nucleus IRF3 induces type I interferon antiviral gene programs to foster an antiviral state. In addition, STING can traffic to the ER-Golgi Intermediate Compartment (ERGIC), where it promotes the formation of autophagosomes to remove microbial pathogens from the cytosol through autophagy. CDNs, cyclic dinucleotides.

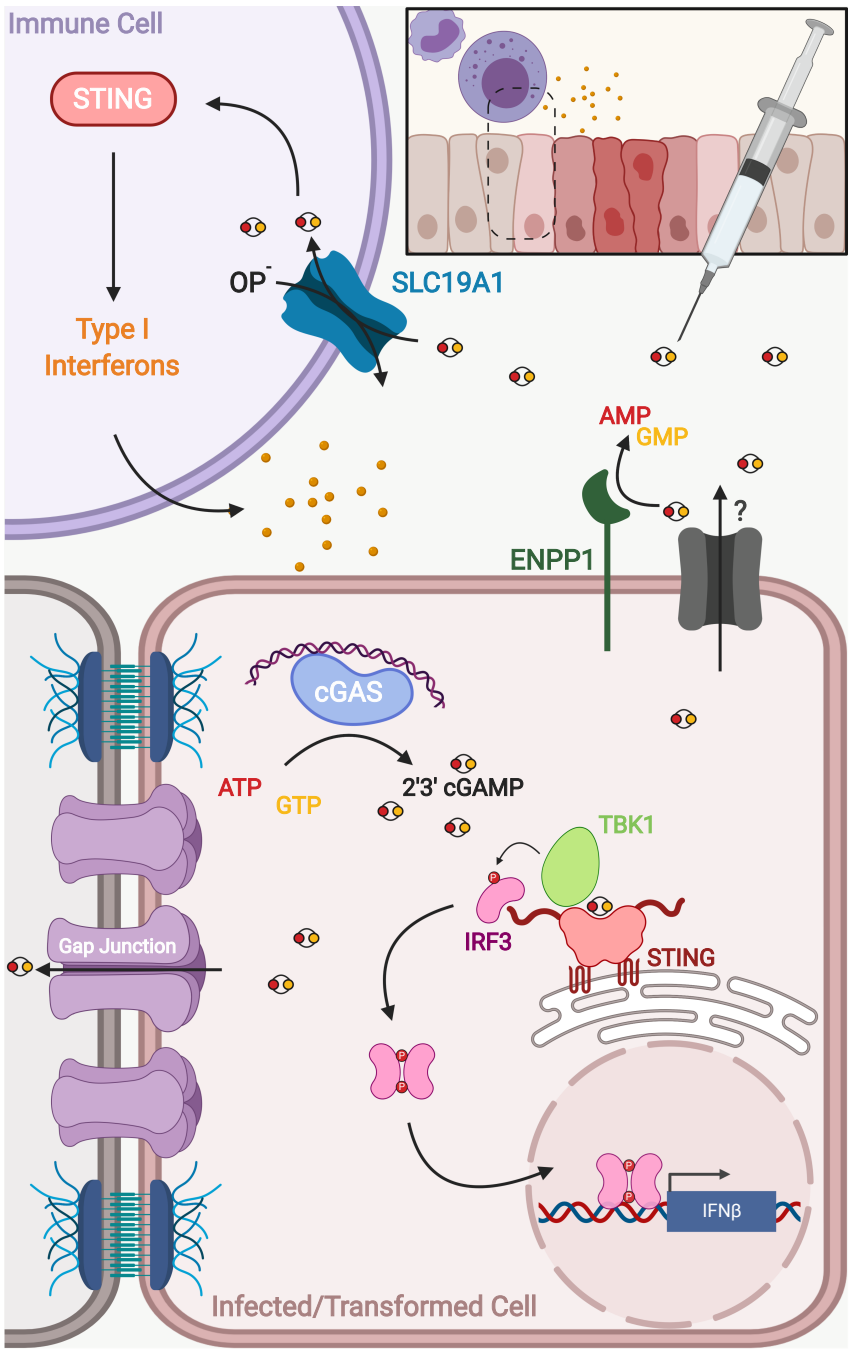

Figure 1.3: cGAMP transport and homeostasis.
Following activation by cytosolic dsDNA species, cGAS catalyzes the *in-situ* formation of 2′3′-cGAMP resulting in STING and type I interferon activation within the infected or transformed cell. Transfer of 2′3′-cGAMP to neighboring bystander cells via gap junctions propagates STING-mediated signaling across the infected or damaged tissue. 2′3′-cGAMP levels can return to their preinduction state through secretion via an unidentified transporter followed by ENPP-1 mediated hydrolysis. Secreted or exogenous CDNs can also be taken up by immune cells via a folate/organic phosphate (OP^-) antiporter, SLC19A1, to further amplify the innate immune response. CDNs, cyclic dinucleotides.

Chapter 2

SLC19A1 Transports Immunoreactive Cyclic Dinucleotides

The majority of this chapter was published in:

Luteijn, R. D., Zaver, S. A., Gowen, B. G., Wyman, S. K., Garelis, N. E., McWhirter, S. M., Katibah, G. E., Corn, J. E., Woodward, J. J. & Raulet, D. H. SLC19A1 transports immunoreactive cyclic dinucleotides. *Nature* 573, 434–438 (2019).

Summary

The accumulation of DNA in the cytosol serves as a key immunostimulatory signal associated with infections, cancer and genomic damage[69,70]. Cytosolic DNA triggers immune responses by activating the cyclic GMP–AMP synthase (cGAS)–stimulator of interferon genes (STING) pathway[71]. The binding of DNA to cGAS activates its enzymatic activity, leading to the synthesis of a second messenger, cyclic guanosine monophosphate–adenosine monophosphate (2′3′-cGAMP)[4,10,12,72]. This cyclic dinucleotide (CDN) activates STING[22], which in turn activates the transcription factors interferon regulatory factor 3 (IRF3) and nuclear factor κ-light-chain-enhancer of activated B cells (NF-κB), promoting the transcription of genes encoding type I interferons and other cytokines and mediators that stimulate a broader immune response. Exogenous 2′3′-cGAMP produced by malignant cells[43] and other CDNs, including those produced by bacteria[2,3,24] and synthetic CDNs used in cancer immunotherapy[73,74] , must traverse the cell membrane to activate STING in target cells. How these charged CDNs pass through the lipid bilayer is unknown. Here, we used a genome-wide CRISPR-interference screen to identify the reduced folate carrier SLC19A1, a folate–organic phosphate antiporter, as the major transporter of CDNs. Depleting SLC19A1 in human cells inhibits CDN uptake and functional responses, and overexpressing *SLC19A1* increases both uptake and functional responses. In human cell lines and primary cells ex vivo, CDN uptake is inhibited by folates as well as two medications approved for treatment of inflammatory diseases, sulfasalazine and the antifolate methotrexate. The identification of SLC19A1 as the major transporter of CDNs into cells has implications for the immunotherapeutic treatment of cancer[73], host responsiveness to CDN-producing pathogenic microorganisms[2] and—potentially—for some inflammatory diseases.

Introduction

The innate immune system is the first and immediate line of defense against invading microorganisms[1,75]. This is mediated by a suite of invariant, germ-line encoded sentinel proteins termed Pattern Recognition Receptors (PRRs) that survey the cellular milieu for highly conserved, often essential microbe or pathogen associated molecular patterns, MAMPs/PAMPs[1]. PRRs can also sense cellular perturbations caused by pathogen activities, for example cleavage of cellular proteins or disruption of ion flux. In addition to sensing PAMPs, some PRRs also sense and respond to damage associated molecular patterns (DAMPs)—endogenous ligands produced in the context of tissue damage or injury—to instigate sterile inflammatory responses[1]. Upon sensing PAMPs and DAMPs, PRRs transduce signals to downstream transcription factors culminating in the activation of pro-inflammatory and innate immune gene programs to eliminate the pathogen or damaged cells[1].

Indeed, the accumulation of aberrant double-stranded DNA (dsDNA) species in the cytosol serves as a key immunostimulatory signal associated with infections, cancer, and genomic damage[4,69,70]. While several DNA sensors have been identified, the enzyme cyclic GMP–AMP synthase (cGAS) has emerged as the primary DNA sensing PRR in most cell types[4,5]. Upon sensing dsDNA, cGAS cyclizes ATP and GTP to produce the second messenger, 2’3’-cGAMP[5,10–12,72]. Binding of cGAMP to the downstream adaptor molecule STING results in its subsequent oligomerization and translocation to the perinuclear Golgi[22]. There, STING serves as a scaffold to recruit the kinase, TBK1, resulting in its autophosphorylation and activation[33,34]. TBK1 in turn phosphorylates the

C-terminal tail of STING to generate a binding surface for the transcription factor IRF3 where it is subsequently phosphorylated by TBK1[33,34]. Phosphorylation of IRF3 results in its dimerization and nuclear translocation culminating in the induction of a type I interferon (IFN-I) innate immune response. STING activation can also trigger NF-κB driven pro-inflammatory gene expression, but the exact mechanisms for NF-κB activation remain poorly understood[33,34].

In addition to sensing endogenous 2'3'-cGAMP, STING can also sense bacterial 3'3'-cyclic dinucleotides produced in the context of bacterial infection[3,24]. While STING has low nanomolar affinity for 2'3'-cGAMP, its affinity for 3'3'-CDNs is two to three orders of magnitude weaker, suggesting that higher, sustained levels of 3'3'-CDNs are required for STING activation[15]. The presence of phosphodiester linkages makes CDNs susceptible to cleavage by phosphodiesterase enzymes; however, these bonds can be replaced with phosphorothioate linkages to yield synthetic CDNs that are resistant to nuclease cleavage. Several such synthetic CDNs have been generated among which 2′3′ RR-S2 cyclic di-AMP (2′3′-RR CDA) is the most potent inducer of STING-dependent IFN-I responses[50,73,74].

Because of their ability to induced potent innate immune responses, cyclic dinucleotides and other related STING agonists are currently in development for use as adjuvants for vaccine development and cancer immunotherapy[43,44,73,74]. In these contexts, CDNs are administered exogenously, often through intra-venous or intra-tumoral injection, and must traverse the plasma membrane to gain access to the cytosol. While mechanisms of 2'3'-cGAMP transfer to bystander cells through gap junctions and packaging into virions have been identified[40–42], how these charged molecules traverse the lipid bilayer remains poorly understood. In this chapter, we perform a genome-wide CRISPR-interference screen to identify cellular factors involved in extracellular CDN mediated IFN-I activation. This screen identified the reduced folate carrier, SLC19A1, as a key protein involved in extra- but not intra-cellular CDN signaling. Using a combination of genetic and biochemical approaches, we provide evidence that SLC19A1 is a direct CDN transporter in human but not in murine immune cells. Taken together, these results may have important implications for cancer immunotherapy, vaccine development, host responses to pathogen infection, and the treatment of autoinflammatory diseases.

Results

Genome-wide CRISPRi screen for host factors necessary for stimulation by CDNs.

To systematically identify genes involved in intracellular transport of CDNs, we performed a genome-wide CRISPR interference (CRISPRi) forward genetic screen in the monocytic THP-1 cell line. To visualize STING activation, THP-1 cells were transduced with a CDN-inducible reporter construct (Figure 2.1a, b). Consistent with previous results, the synthetic CDN 2′3′ RR-S2 cyclic di-AMP (2′3′-RR CDA, Figure 2.2a) induced a more potent response than 2′3′-cGAMP[73], and the response to both CDNs was severalfold higher than the response to human interferon-β (IFN-β). The response to CDNs was completely dependent on STING expression (Figure 2.1b), implying that the reporter primarily reported cell-intrinsic STING activity. For the screen, THP-1 cells expressing a catalytically inactive Cas9 (dCas9) fusion with blue fluorescent protein (BFP) and the transcriptional repression domain KRAB (dCas9–BFP–KRAB), and transduced with a genome-wide guide-RNA (gRNA) library, were stimulated separately with 2′3′-

RR CDA or 2′3′-cGAMP, and the highest and lowest quartiles of reporter-expressing cells were sorted by flow cytometry before deep-sequencing to identify gRNAs enriched in each population (Figures 2.1c-e, 2.2b, c and 2.3). The two screens yielded many common hits but there were differences, such as numerous hits in the 2′3′-cGAMP screen—including *STAT2*, *IRF9*, *IFNAR1* and *IFNAR2*. Hence, the 2′3′-RR CDA screen may have mostly been dependent on intrinsic STING signaling, whereas the 2′3′-cGAMP screen may have been partly dependent on autocrine–paracrine IFN-β signaling.

In both screens, the top hits in the hypo-responsive population (that is, the genes that are most important for robust responses to CDNs) included the gene for the transcription factor IRF3, which acts directly downstream of STING. A gRNA for *STING* (also known as *TMEM173*) was also enriched in hypo-responsive cells from both screens, but other STING gRNAs were not enriched—presumably because they were ineffective at interfering with *STING* expression.

SLC19A1 was one of the most significant hits in both screens. SLC19A1 is a folate–organic phosphate antiporter that transports folates, structurally similar antifolates and a variety of organic phosphates encompassing (among others) thiamine derivatives and nucleotides[76,77]. Folate import is coupled to organic phosphate export and many inhibition and exchange phenomena have previously been demonstrated[78–80].

SLC19A1 is required for CDN-induced reporter expression.

To validate the role of *SLC19A1* in CDN stimulation, the top two enriched *SLC19A1*-targeting gRNAs from the 2′3′-RR CDA screen were used to stably deplete *SLC19A1* in THP-1 cells expressing dCas9–KRAB (Figure 2.4a). *SLC19A1*-depleted cells grew normally, but uptake of the SLC19A1 substrate methotrexate was nearly abolished in these cells[81] (Figure 2.4c). Similar to *IRF3*-depleted cells, *SLC19A1*-depleted THP-1 or U937 cells (Figure 2.4b) were defective in reporter responses induced by 2′3′-cGAMP, 2′3′-RR CDA and 3′3′-CDA (a bacterial CDN that stimulates STING), but responded normally to IFN-β stimulation (Figures 2.4d-f and 2.5a, b). *SLC19A1* depletion—similar to depletion of *IRF3* or *STING*—also inhibited CDN-induced expression of direct downstream target genes in the STING pathway, including *IFNB1* and the chemokine genes *CCL5* and *CXCL10*[82,83] (Figures 2.4g-i and 2.5c). Transduction of *SLC19A1* into depleted THP-1 cells rescued CDN responsiveness (Figure 2.5d). *SLC19A1* disruption using the conventional CRISPR–Cas9 system similarly decreased responsiveness to CDNs in THP-1 cells (Figure 2.5e).

SLC19A1 overexpression robustly increased CDN responsiveness in wild-type THP-1 cells and in cell lines that normally respond poorly (or not at all) to CDN stimulation, including C1R, K562 and 293T cells (pre-transduced with STING) (Figures 2.4j, 2.5f, and 2.6). Together, our data show reduced CDN responses in *SLC19A1*-deficient cells and amplified responses in cells that overexpress *SLC19A1*.

Inhibitor experiments showed that the known SLC19A1 substrates methotrexate and 5-methyl-tetrahydrofolic acid (5-me-THF)[76] blocked stimulation of THP-1 cells by 2′3′-cGAMP or 2′3′-RR CDA at concentrations only modestly higher than those that inhibit uptake of folate derivatives[84], but did not inhibit reporter responses to IFN-β (Figure 2.5g). At high concentrations, the non-

competitive SLC19A1 inhibitor sulfasalazine[84] blocked responses to CDNs and to IFN-β stimulation, which suggests a broader effect on reporter activation (Figure 2.4k).

SLC19A1 is critical for STING-dependent responses to exogenous CDNs but not when CDNs are provided intracellularly.

To directly assess the effect of SLC19A1 on STING pathway activation (Figure 2.8a), we used immunoblotting to evaluate phosphorylation of STING, IRF3 and TBK1 induced by a 2-h exposure to 2′3′-RR CDA in control (non-targeting gRNA) versus CRISPRi-depleted cells (Figure 2.7a). As expected, *STING* depletion inhibited phosphorylation of both TBK1 and IRF3, whereas *IRF3* depletion did not inhibit phosphorylation of TBK1 or STING. By contrast, *SLC19A1* depletion resulted in major defects in phosphorylation of STING, TBK1 and IRF3, which indicates that *SLC19A1* acts upstream of STING.

Protein levels of STING, TBK1 and IRF3 were unaltered in *SLC19A1*-depleted cells. Notably, *SLC19A1*-depleted cells responded normally when transfected with DNA (Figure 2.7b). Furthermore, when transport was bypassed by permeabilizing *SLC19A1*-depleted cells with digitonin, STING exhibited a normal phosphorylation response to CDNs (Figure 2.7c). Similarly, the inhibitory effects on CDN-induced STING phosphorylation and gene expression of SLC19A1 blockers—including methotrexate, 5-me-THF and the irreversible, covalent SLC19A1 inhibitor *N*-hydroxysuccinimide (NHS)–methotrexate (see Materials and Methods section)—were bypassed when the cells were permeabilized with digitonin (Figures 2.7d and 2.8b-f). Thus, STING functioned normally in *SLC19A1*-depleted or inhibited cells when CDNs or DNA were introduced directly into the cytosol, consistent with a role for SLC19A1 in CDN transport.

SLC19A1 transports CDNs.

To directly test the effect of SLC19A1 on transport, we monitored cellular uptake of ^{32}P-labelled CDNs (Figure 2.9 a-h). *SLC19A1* overexpression resulted in a two-to-threefold enhancement of [^{32}P]2′3′-cGAMP uptake by THP-1, K562 and C1R cells (Figures 2.10a, b and 2.9i). Conversely, *SLC19A1* depletion reduced the uptake of [^{32}P]2′3′-cGAMP in THP-1 and K562 cells (Figures 2.9 j-m and 2.10a, b). Furthermore, we observed reduced 2′3′-cGAMP influx in THP-1 and K562 cells treated with NHS–methotrexate (Figure 2.10c). Uptake of 2′3′-cGAMP by THP-1 cells was also inhibited by excess unlabelled 2′3′-cGAMP as well as by the bacterial CDNs 3′3′-cGAMP, 3′3′-CDA and 3′3′ c-di-GMP. Thus, CDN interactions with the transporter are not highly specific for the 2′3′ linkage or the specific nucleotides (Figure 2.10d). The nucleoside monophosphates AMP and GMP—the major ENPP1 hydrolysis products of 2′3′-cGAMP—slightly inhibited uptake of [^{32}P]2′3′-cGAMP[50,51] (Figure 2.10d), consistent with previous observations that AMP, other nucleotides and organic phosphates in general inhibit SLC19A1-mediated transport[78,79]. Our findings indicate that SLC19A1 broadly interacts with CDNs irrespective of the phosphodiester linkages or the base content, but that breakdown products of CDNs have a limited effect on CDN uptake.

Sustained inhibition of 2′3′-cGAMP uptake occurred when folic acid, 5-me-THF, methotrexate or sulfasalazine were added to the culture medium of various cell lines (Figures 2.9n-o and 2.10e). In terms of half-maximum inhibitory concentration (IC_{50}), sulfasalazine (IC_{50} = 2.1 μM) and folic

acid (IC_{50} = 4.8 μM) were in the same range as 2′3′-cGAMP (IC_{50} = 1.89 μM) (Figure 2.9p) similar to the dosage of 2′3′-cGAMP required for STING activation and interferon responses (10–20 μM) (Figure 2.4d). Consistent with their much higher affinity for SLC19A1 binding compared with folic acid, 5-me-THF (IC_{50} = 4.1 nM) and methotrexate (IC_{50} = 54.8 nM) were much more potent inhibitors of CDN uptake[78] (Figure 2.9p). Notably, 5-me-THF incompletely inhibited [^{32}P]2′3′-cGAMP uptake, unlike the other folates or antifolates. Consistent with an antiporter mechanism of uptake, preloading the cells with 5-me-THF—which *trans*-stimulates SLC19A1 import[85]—augmented 2′3′-cGAMP influx (Figure 2.9q). These observations establish that CDN import is altered by known substrates and inhibitors of the SLC19A1 transporter in a wide range of human cell lines.

We next monitored 2′3′-cGAMP uptake in primary healthy adult human peripheral blood mononuclear cells (PBMCs). Treatment of PBMCs with NHS–methotrexate, or excess, unlabelled 5-me-THF, methotrexate or sulfasalazine strongly inhibited [^{32}P]2′3′-cGAMP uptake (Figures 2.9r and 2.10f). These data generalize our findings to normal human blood cells.

In contrast to these results in human cells, neither CDN uptake nor CDN-induced *Cxcl10* expression was inhibited by depleting *Slc19a1* expression in the mouse C1498 or L1210 cell lines, the latter of which has extensively been studied in the context of SLC19A1-mediated transport[78,79,86] (Figure 2.11a-h). *Slc19a1* depletion in mouse bone-marrow-derived macrophages or dendritic cells also did not block *Ifn* gene expression induced by CDNs (Figure 2.11i-l). Furthermore, antifolates that inhibit SLC19A1, including methotrexate, did not inhibit 2′3′-cGAMP uptake by mouse splenocytes (Figure 2.11m-o). Collectively, these results suggested that SLC19A1 expression and function are essential for uptake of the metazoan CDN 2′3′-cGAMP by human cell lines and human primary cells ex vivo, but not by the mouse cells we studied. Therefore, mouse cells probably express another potent CDN transporter.

SLC19A1-mediated import of CDNs would require a direct interaction with the CDN. Consistent with this hypothesis, His-tagged SLC19A1 was precipitated by 2′3′-cGAMP immobilized on Sepharose beads (Figures 2.10g and 2.12a, b). This interaction was competitively disrupted by free, unbound 2′3′-cGAMP and 3′3′-CDA (Figure 2.10h, Figure 2.12c) or by 5-me-THF and methotrexate (Figure 2.10h). These data suggest that CDNs interact with SLC19A1, consistent with its proposed role as a CDN transporter. Taken together, our results demonstrate that SLC19A1 is a CDN transporter in human cells, which is required for activation of type I interferon mediated by exogenous CDNs.

The response to CDNs was relatively weak in most cell lines that we tested and was increased by overexpression of *SLC19A1* or permeabilization of cells (Figures 2.5f and 2.7c). Among a large set of cell lines, THP-1 cells are among the highest in expression of both *SLC19A1* and *STING* (Figure 2.13). It is likely that expression of *SLC19A1* and *STING* are each important predictors of the responsiveness of cell lines and tumors to CDN stimulation.

Methotrexate, folic acid and sulfasalazine almost completely blocked CDN uptake and/or stimulation, whereas CDN stimulation was not completely inhibited in *SLC19A1*-null cells. This implies that another transporter sensitive to these drugs may have a role in CDN uptake. Although it was not a hit in our screen, overexpression of *SLC46A1*, which encodes the only other known

folate transporter[76], increased responses to CDNs (Figure 2.14a). However, depletion of *SLC46A1* (approximately 90% reduction in mRNA) had little or no effect on CDN stimulation, even when combined with depletion of *SLC19A1* (Figure 2.14c). Overexpression of *SLC46A3*, another hit in our screen, increased the response to CDNs (Figure 2.14b) and depletion of *SLC46A3* (90% effective) had a minor effect on reporter induction by both CDNs (Figure 2.14d). However, depleting both *SLC19A1* and *SLC46A3* together did not reduce responses more than depletion of *SLC19A1* alone (Figure 2.14d), which suggests that neither SLC46A3 nor SLC46A1 is responsible for most of the residual CDN transport in *SLC19A1*-depleted cells.

Concluding Remarks

Our findings extend the spectrum of organic phosphates that use SLC19A1 to 2′3′-cGAMP, 2′3′-RR CDA and probably other CDNs, by the direct measurement of their transport and the effect of extracellular and intracellular folates on their uptake in human cells by this route. In this context, SLC19A1 could have an important role in the antitumor and adjuvant effects of CDNs administered to patients. It may also be important in cell-to-cell transport of CDNs in immune responses or immune pathology. For example, the SLC19A1 inhibitors methotrexate and sulfasalazine are first-line treatments in rheumatoid arthritis and are widely used to treat inflammatory bowel diseases, including ulcerative colitis and Crohn's disease[87–89]. Although no direct evidence for this is available in humans, studies in mouse models of inflammatory bowel disease raise the possibility that host cells import CDNs produced by intestinal bacteria, activating STING in a cGAS-independent fashion[90]. It remains to be determined whether SLC19A1 has a role in such processes in humans. In conclusion, we have identified SLC19A1—in humans—as a CDN transporter with potential relevance in the context of cancer immunotherapy and immunopathology.

Materials and Methods

Cell culture

All cell lines were cultured at 37 °C in humidified atmosphere containing 5% CO_2 with medium supplemented with 100 U ml^{-1} penicillin, 100 µg ml^{-1} streptomycin, 0.2 mg ml^{-1} glutamine, 10 µg ml^{-1} gentamycin sulfate, 20 mM HEPES and 10% FCS. THP-1, C1R, and K562 cells were cultured in RPMI medium, and 293T, 293T transfected with human STING (293T+hSTING), MDA-MBA-453 (MDA) and RAW 264.7 macrophages were cultured in DMEM medium. Human embryonic kidney 293F cells (HEK293F) were grown in FreeStyle 293 medium supplemented with GlutaMax (GIBCO) at 37 °C in the presence of 5% CO_2 in a shaking incubator.THP-1, K562, 293T cells, and RAW 264.7 macrophages were from existing stocks in the laboratory. MDA-MB-231 cells were obtained from the Berkeley Cell Culture Facility. C1R cells were a gift from V. Spies (Fred Hutchinson Cancer Center). HEK293F cells were a gift from D. Veesler (University of Washington). The 293T+hSTING cells were generated as previously described[73]. L1210 cells were obtained from ATCC (CCL-219) and cultured in DMEM including 10% horse serum (Gibco, cat. no. 26-050-088). L1210 cells were authenticated by ATCC. MDA-MBA-453 were authenticated by the Berkeley Cell Culture Facility using karyotyping and/or PCR; other cell lines were not authenticated. All cell lines were negative for mycoplasma contamination.

Antibodies and reagents

The following antibodies were obtained from Cell Signaling Technology: rabbit-anti-human TBK1 monoclonal (clone D1B4; 1:500 for immunoblot), rabbit-anti-human p-TBK1 monoclonal (clone D52C2; 1:1,000 for immunoblot), rabbit-anti-human STING monoclonal (clone D2P2F; 1:2,000 for immunoblot), rabbit-anti-human p-STING monoclonal (clone D7C3S; 1:1,000 for immunoblot), rabbit-anti-human p-IRF3 monoclonal (clone 4D4G, 1:1,000 for immunoblot). Antibodies obtained from LI-COR Biosciences: goat-anti-mouse IgG IRDye 680RD conjugated (cat. no. 926-68070; used at 1:5,000), donkey-anti-rabbit IgG IRDye 800CW conjugated (cat. no. 926-32213; used at 1:5,000), donkey-anti-rabbit IgG IRDye 680RD (cat. no. 926-68073; used at 1:5,000). Other antibodies: rabbit-anti-human IRF3 monoclonal (Abcam, cat. no. EP2419Y; 1:2,000 for immunoblot), mouse-anti-human transferrin receptor monoclonal (Thermo Fisher Scientific, clone H68.4; 1:1,000 for immunoblot), rabbit-anti-human SLC19A1 polyclonal (BosterBio, cat. no. PB9504; 0.4 µg ml^{-1} for immunoblot), APC-conjugated mouse-anti-human CD55 monoclonal (BioLegend, clone JS11; 1:50 for flow cytometry), mouse-anti-human CD59 monoclonal (BioLegend clone p282; 1:250 for flow cytometry), APC-conjugated goat-anti-mouse IgG (BioLegend, cat. no. 405308; 1:100 for flow cytometry). Reagents used: 5-methyl THF (Cayman Chemical, cat. no. 16159), methotrexate (Cayman Chemical, cat. no. 13960), folic acid (Cayman Chemical, cat. no. 20515), sulfasalazine (Sigma-Aldrich, cat. no. S0883), polybrene (EMD Millipore, cat. no. TR1003G), 3′3′-cyclic-di-AMP (3′3′ CDA) (Invivogen, cat. no. tlrl-nacda), 2′3′-RR c-di-AMP (2′3′-RR-S2 CDA) and 2′3′- cyclic-di-GMP-AMP (2′3′-cGAMP) (gifts from Aduro Biotech), human IFN-β (PeproTech, cat. no. 300-02B), mouse IFN-β1 (BioLegend, cat. no. 581302). Antibiotic selection: puromycin (Sigma-Aldrich, cat. no. P8833), blasticidin (Invivogen, cat. no. ant-bl-1; used at 10 µg ml^{-1}), zeocin (Invivogen, cat. no. ant-zn-1; used at 200 µg ml^{-1}).

Plasmids

A gBLOCK gene fragment (Integrated DNA Technologies) encoding the tdTomato reporter gene driven by the ISREs and the minimal mouse IFN-β promoter was cloned into a dual-promoter lentiviral plasmid using Gibson assembly. This lentiviral plasmid co-expressed the zeocin resistance gene and GFP via a T2A ribosomal-skipping sequence controlled by the human EF1A promoter, and was generated as previously described[91].

For rescue and overexpression of the folate-organic phosphate antiporter *SLC19A1*[76,86,92–95], the proton-coupled folate transporter *SLC46A1*[76] or the maytansine transporter *SLC46A3*[96], a gBLOCK gene fragment encoding *SLC19A1* (gene ID 6573, transcript 1), *SLC46A1* (gene ID 113235) or *SLC46A3* (gene ID 283537) was cloned by Gibson assembly into a dual-promoter lentiviral plasmid co-expressing the blasticidin resistance gene and the fluorescent gene mAmetrine.

For CRISPRi-mediated depletions, cells were transduced with a lentiviral dCas9-HA-BFP-KRAB-NLS expression vector (Addgene plasmid no.102244).

For screen validation using individual gRNAs, gRNAs (Table 3.1) were cloned into the same expression plasmid used for the gRNA library (pCRISPRia-v2, Addgene plasmid no. 84832, a gift from J. Weissman). The lentiviral gRNA plasmid co-expressed a puromycin resistance gene and blue fluorescence protein (BFP) via a T2A ribosomal skipping sequence controlled by the human EF1A promoter. The CRISPRi gRNAs introduced into this vector by Gibson assembly were expressed from a mouse U6 promoter. For expression of multiple gRNAs, additional gRNAs were introduced in a separate vector that co-expressed the blasticidin resistance gene and mAmetrine via a T2A ribosomal skipping sequence under the control of a human EF1A promoter.

Conventional CRISPR gRNAs (see Table 2.1) were cloned into a selectable lentiviral CRISPR–Cas9 vector. This lentiviral vector included a human codon-optimized *Streptococcus pyogenes* Cas9 co-expressing the puromycin resistance gene via a T2A ribosome-skipping sequence under the control of a minimal human EF1A promoter[91,97].

Lentiviral production and transduction

Lentivirus was produced by transfecting lentiviral plasmids and second-generation packaging and polymerase plasmids into 293T cells using TransIT-LT1 Reagent (Mirus Bio). Virus-containing supernatants were collected 72 h later, centrifuged to remove cell debris and filtered using a 0.45-μm polyethersulfone filter. Filtered virus supernatant was used to transduce target cells by spin-infection (800*g* for 90 min at 33 °C) in the presence of 8 μg ml polybrene. After spin infection, virus and polybrene-containing medium was diluted 1:1 with fresh medium. Seventy-two hours after transduction, cells were sorted on the basis of fluorescence expression using a BD FACSAria cell sorter or selected with the relevant selection reagent for at least seven days.

2′3′-RR CDA and 2′3′-cGAMP screens

THP-1 cells co-expressing the tdTomato reporter, GFP and dCas9–BFP were single-cell-sorted to select for a THP-1 cell clone with efficient dCas9–BFP-knockdown capacity. Clones were transduced with lentiviral vectors encoding gRNAs targeting GFP, *CD55* or *CD59*. After one week with puromycin (2 μg ml^{-1}) selection, CD55, CD59 and GFP expression were quantified using the BD LSR Fortessa flow cytometer. A clone that showed the highest reduction in all three marker genes was selected for the screens.

Two separate cultures of THP-1 cells were transduced with the human genome-wide CRISPRi v2 library[98]. Each culture was divided in two and screened separately after treatment with 2′3′-RR CDA or 2′3′-cGAMP, followed by selection and analysis. Hence, each screen was performed twice, with independent library transductions. For each transduction, the THP-1 clone was expanded to 3.2×10^8 cells and transduced with the human genome-wide CRISPRi v2 library[98], which contains approximately 100,000 gRNAs targeting around 20,000 genes. Sufficient cells were transduced and propagated to maintain at least 5×10^7 transduced (BFP^+) cells, representing 500× coverage of the gRNA library. The transduction efficiency was around 20% to minimize the chance of multiple lentiviral integrations per cell. Two days after transduction, cells were cultured in the presence of puromycin for two days and for one additional day without puromycin. Cells (4×10^8) were seeded to a density of 10^6 cells per ml and stimulated with 2′3′-RR CDA (2 μg ml^{-1}) or 2′3′-cGAMP (15 μg ml^{-1}). Twenty hours later, cells were collected, washed in PBS and sorted on the basis of BFP expression (presence of gRNAs), GFP expression (presence of reporter) and tdTomato expression using the BD Influx cell sorter and BD FACSaria Fusion cell sorter. The cells were sorted into two populations on the basis of tdTomato expression: the highest 25% of tdTomato expressing cells (hyper-responsive population) and lowest 25% of tdTomato expressing cells (hypo-responsive population). During sorting, all cells were kept at 4 °C. After sorting, cells were counted: the sorted populations contained $1.5–2 \times 10^7$ cells, and the unsorted control contained $1–1.5 \times 10^8$ cells. Cells were washed in PBS and cell pellets were stored at −80 °C until further processing.

gDNA isolation and sequencing

Genomic DNA was isolated from sorted cells using NucleoSpin Blood kits (Macherey-Nagel). PCR was used to amplify gRNA cassettes with Illumina sequencing adapters and indexes as previously described[99]. Genomic DNA samples were first digested for 18 h with *SbfI*-HF (NEB) to liberate a ~500-bp fragment containing the gRNA cassette. The gRNA cassette was isolated by gel electrophoresis as previously described[99] using NucleoSpin Gel and PCR Clean-up kits (Macherey-Nagel), and the DNA was then used for PCR. Indexed samples were pooled and sequenced on an Illumina HiSeq-2500 for the 2′3′RR CDA screen and an Illumna HiSeq-4000 for the 2′3′-cGAMP screen using a 1:1 mix of 2 custom sequencing primers. Sequencing libraries were pooled proportional to the number of sorted cells in each sample. The target sequencing depth was at least 2,000 reads per gRNA in the library for unsorted 'background' samples, and at least 10 reads per cell in sorted samples.

Screen data analysis

CRISPRi samples were analysed using the Python-based ScreenProcessing pipeline (https://github.com/mhorlbeck/ScreenProcessing). Normalization using a set of negative control

genes and calculations of phenotypes and Mann–Whitney *P* values were performed as previously described[98,100]. In brief, Illumina 50-bp single-end sequencing reads for pooled sublibraries 1 to 4 and 5 to 7 were trimmed to 29 bp and guides were quantified by counting exact matches to the CRISPRi v.2 human library guides. Phenotypes were calculated as the $\log_2$ fold change in enrichment of an sgRNA in the high and low samples versus background as well as high versus low, normalized by median subtracting non-targeting sgRNAs[100,101]. Phenotypes from sgRNAs targeting the same gene were collapsed into a single-sensitivity phenotype for each gene using the average of the top three scoring sgRNAs (by phenotype absolute value). For genes with multiple independent transcription start sites (TSSs) targeted by the sgRNA libraries, phenotypes and *P* values were calculated independently for each TSS and then collapsed to a single score by selecting the TSS with the lowest Mann–Whitney *P* value. Counts from the ScreenProcessing pipeline were then used as input to the MAGeCK program to obtain FDR scores for filtering. We integrated multiple gRNAs per gene comparing the hypo-responsive and hyper-responsive populations calculated as RRA scores as depicted in Figure 1.1d, e. Similar results were obtained when each sorted population was compared to unsorted cells.

Genes were also ranked by individual gRNAs with the greatest enrichment or depletion between the hypo-responsive and hyper-responsive libraries. gRNA read counts were normalized to library sequencing depth by converting to read counts per million total reads. For each gRNA, the ratio between the read counts for the hypo-responsive and hyper-responsive libraries was determined and averaged between replicates. For hypo-responsive gene rankings, each gene was ranked by the single corresponding gRNA with the highest hypo-to-hyper ratio. For hyper-responsive gene rankings, each gene was ranked by the single corresponding gRNA with the lowest hypo-to-hyper ratio.

CDN and IFN-β stimulation assays

The week before stimulation experiments, cells were cultured at the same density. The day before stimulation, cells were seeded to 0.5×10^6 cells per ml. Cells were stimulated with CDNs or IFN-β in 48-well plates using 50,000 cells per well in 300 µl medium. After 18–24 h, cells were transferred to a 96-well plate and tdTomato expression was measured by flow cytometry using a high-throughput plate reader on a BD LSR Fortessa. For stimulations in the presence of sulfasalazine, 5-me-THF or methotrexate, cells were stimulated in 48-well plates using 20,000 cells per well in 300 µl medium. Cells were incubated with compounds or DMSO as vehicle before stimulations with CDNs or IFN-β. 18–24h after stimulation, tdTomato reporter expression was quantified by flow cytometry using a high-throughput plate reader on a BD LSR Fortessa.

Production of *SLC19A1*-knockout cell lines

As an alternative approach to corroborate the role of *SLC19A1* in CDN responses, *SLC19A1* was disrupted in THP-1 cells using the conventional CRISPR–Cas9 system. THP-1 cells expressing the tdTomato reporter were transduced with a CRISPR–Cas9 lentiviral plasmid encoding a control gRNA or a gRNA targeting *SLC19A1* at a region critical for transport[102] (Table 2.1). Transduced cells were selected using puromycin for two days and single-cell-sorted using a BD FACSAria cell sorter. Control cells and *SLC19A1*-targeted cells were selected that had comparable forward and side scatter by flow cytometry analysis. Genomic DNA was isolated from clones using the

Qiamp DNA minikit (Qiagen), and the genomic region surrounding the *SLC19A1* gRNA target site was amplified by PCR using primers 5′-TTCTCCACGCTCAACTACATCTC-3′ and 5′-CAGCATCCGCGCCAGCACTGAGT-3′. PCR product was cloned into 5-alpha competent bacteria (New England Biolabs, cat. no. C2987) using a TOPO TA cloning kit (Thermo Fisher Scientific, cat. no. 450641) according to the manufacturer's instructions. After blue/white screening, a minimum of ten colonies were sequenced per THP-1 clone, and sequences were analysed using SeqMan (Lasergene DNASTAR). Nine independent THP-1 clones with out-of-frame mutations at the *SLC19A1* gRNA target site were selected for further experiments. These clones were all significantly less sensitive to CDN stimulation when compared to seven control clones that received a non-targeting gRNA (Figure 2.5e).

shRNA knockdown

For shRNA knockdown experiments, shRNA sequences were cloned into the pLKO.1 lentiviral expression vector. Cells were transduced with lentivirus and selected using 2 μg ml^{-1} puromycin for at least 5 days. As controls, shRNAs targeting GFP (shRNA1; TRCN0000231753) and luciferase (shRNA2 TRCN0000231737) were used. Mouse SLC19A1 targeting shRNA sequences: GCAGGTGACTAACGAGATCAT (shRNA 4), and CCGTATCTACTTCATATACTT (shRNA 6); human SLC19A1 targeting shRNA (shRNA 9): CGACGGTGTTCAGAATGTGAA. All shRNA knockdowns were confirmed by real-time qPCR. Depletion of SLC19A1 function was confirmed by showing decreased uptake of [^{3}H]-methotrexate (see below and Figures 2.9l and 2.11c, g)

RT–qPCR

Cells were collected and washed in ice-cold PBS. Cells were transferred to RNase-free microcentrifuge tubes and RNA was isolated using the RNeasy mini kit (Qiagen, cat. no. 74104) including a DNase I step (Qiagen, cat. no. 79254). RNA concentration was measured by NanoDrop (Thermo Fisher), and 1 μg of RNA was used as input for cDNA synthesis using the iScript cDNA synthesis kit (Bio-rad, cat. no. 1708890). cDNA was diluted to 20 ng μl^{-1} and 2.5 μl per reaction was used as input for the qPCR reaction. qPCR reactions were set up using SSOFast EvaGreen Supermix (Bio-Rad, cat. no. 1725200) according to the manufacturer's recommendations, using 500 nM of each primer and following cycling conditions on a Bio-Rad C1000 Thermal Cycler: 2 min at 98 °C, 40 repeats of 2 s at 98 °C and 5 s at 55 °C. Primers used to amplify the *HPRT1, YWHAZ, CCL5*, *CXCL10*, *STING*, *IRF3*, *SLC19A1*, *SLC46A1* and *SLC46A3*-specific PCR products are listed in Table 2.2. The housekeeping genes *HPRT1* and *YWHAZ* served as endogenous controls for human cDNA samples and *Gapdh* and *Ubc* served as endogenous control for mouse cDNA samples.

For quantification of human *IFNB1, OASL*, or *ISG15* mRNA, RNA was extracted with the Nucleospin RNA Isolation Kit (Machery-Nagel) and reverse-transcribed with the iScript cDNA synthesis kit (Bio-Rad). TaqMan real-time qPCR assays were used for quantification of human *IFNB1* (Hs01077958_s1), human *OASL* (Hs00984387_m1), and human *ISG15* (Hs01921425_s1). *Actb* (Hs01060665_g1) served as an endogenous control.

Synthesis of [^{32}P]2′3′-cGAMP and [^{32}P]3′3′-CDA

Radiolabelled 2′3′-cGAMP was enzymatically synthesized by incubating 0.33 μM α-[^{32}P]ATP (Perkin-Elmer) with 250 μM unlabelled GTP, 1 μg of interferon stimulatory DNA 100mer (provided by D. Stetson) and 1 μM of recombinant His-tagged 2′3′-cGAMP synthase (cGAS) in binding buffer (40 mM Tris pH 7.5, 100 mM NaCl and 20 mM $MgCl_2$) at 37 °C overnight. The reaction was confirmed to have gone to completion by thin layer chromatography (TLC) analysis (Figure 2.9 a, b). In brief, the 2′3′-cGAMP synthesis reaction was separated on Polygram CEL300 PEI TLC plates (Machery-Nagel) in buffer containing 1:1.5 (v/v) saturated $(NH_4)_2SO_4$ and 1.5 M NaH_2PO_4 pH 3.6. The TLC plates were then air-dried and exposed to a PhosphorImager screen for visualization using a Typhoon scanner (GE Healthcare Life Sciences). Next, the sample was incubated with HisPur Ni-NTA resin (Thermo Scientific) for 30 min to remove recombinant cGAS. The resultant slurry was transferred to a minispin column (Thermo Scientific) to elute crude [^{32}P]2′3′-cGAMP. Recombinant mSTING-CTD protein was used for further purification of synthesized [^{32}P]2′3′-cGAMP. mSTING-CTD (100 μm) was bound to HisPur Ni-NTA resin and incubated with the remaining crude 2′3′-cGAMP synthesis reaction mixture for 30 min on ice. Following removal of the supernatant, the Ni-NTA resin was washed three times with cold binding buffer. The resin was then incubated with 100 μl of binding buffer for 10 min at 95 °C, and transferred to a minispin column to elute [^{32}P]2′3′-cGAMP. The resulting STING-purified [^{32}P]2′3′-cGAMP was evaluated by TLC analysis and determined to be about 99% pure (Figure 2.9c).

Radiolabelled 3′3′-CDA was synthesized as previously described[103]. In brief, 1 μM α-[^{32}P]ATP (Perkin-Elmer) was incubated with 1 μM of recombinant DisA in binding buffer at 37 °C overnight. The reaction mixture was boiled for 5 min at 95 °C and DisA was removed by centrifugation. Recombinant His-tagged RECON was then used to further purify the 3′3′-CDA reaction mixture. One hundred micromolar His-tagged RECON was bound to HisPur Ni-NTA resin for 30 min on ice. The resin was washed three times with cold binding buffer and then incubated with 100 μl of binding buffer for 5 min at 95 °C. The slurry was then transferred to a minispin column to elute [^{32}P]c-di-AMP. The purity of the radiolabelled 3′3′-CDA was assessed by TLC and determined to be about 98%.

Nucleotide-binding assays

The ability of radiolabelled 2′3′-cGAMP and 3′3′-CDA to bind recombinant STING was evaluated by differential radial capillary action of ligand assay (DRaCALA) analysis, as previously described[104] (Figure 2.9d). In brief, varying concentrations of recombinant STING were incubated with about 1 nM of radiolabelled CDN in binding buffer for 10 min at room temperature. The reaction mixtures were blotted on nitrocellulose membranes and air-dried for 15 min. The membranes were then exposed to a PhosphorImager screen and visualized using a Typhoon scanner.

NHS–methotrexate synthesis and affinity labelling

NHS– methotrexate was prepared as previously described[105]. In brief, methotrexate (2.2 mg) was acidified by the addition of HCl and dried under vacuum. Next, acidified methotrexate, 1-ethyl-3-(3-dimethylaminopropyl) carbodiimide (EDC) (7.8 mg), and NHS (5.8 mg) were dissolved in 1 ml of anhydrous, tissue-culture grade dimethylsulfoxide and incubated for 2 h at 23 °C. The

activated reagent was used immediately by incubating cells with 5 μM NHS–methotrexate in RPMI 1640 medium (GIBCO) supplemented with 10 mM HEPES, 1 mM sodium pyruvate and 2 mM L-glutamine (Thermo Fisher) for 30 min at 37 °C. The cells were then recovered by centrifugation, washed twice in treatment medium and re-suspended in pre-warmed RPMI 1640 medium (GIBCO) containing 10% (v/v) heat-inactivated FBS (HyClone) and supplemented with 10 mM HEPES, 1 mM sodium pyruvate and 2 mM L-glutamine (Thermo Fisher) to a final cell density of 1×10^6 to 1×10^7 cells per ml.

Nucleotide-uptake assays

For transport assays, cells were collected by centrifugation and washed in Dulbecco's phosphate-buffered saline (DPBS) (Life Technologies). The cell pellets were re-suspended in pre-warmed RPMI 1640 medium (GIBCO) containing 10% heat-inactivated FBS (HyClone) and supplemented with 10 mM HEPES, 1 mM sodium pyruvate and 2 mM L-glutamine (Thermo Fisher) to a final cell density of 1×10^7 cells per ml. Uptake of 1 nM [^{32}P]2′3′-cGAMP and 3′3′-CDA was assayed in cell suspensions at 37 °C over the indicated time points. At the end of each time point, transport was quenched by the addition of cold DPBS. Cells were washed three times with cold DPBS, followed by lysis in 50 μl of cold deionized water. The cell lysates were then transferred to 5 ml of liquid scintillation cocktail (National Diagnostics) and the associated radioactivity was measured by liquid scintillation counting using a LS6500 Liquid Scintillation Counter (Beckman Coulter). For each sample, [^{32}P]2′3′-cGAMP (counts per minute) was normalized to cell count (10^6 cells per sample). For competition experiments, cells were pre-incubated with indicated concentrations of 'cold' unlabelled ligand or inhibitor for 15 min before the addition of 1 nM 'hot' [^{32}P]2′3′-cGAMP. Cells were then collected at the indicated time points and processed as described above.

2′3′-cGAMP was incorporated into THP-1 cells at a linear rate over at least three hours of incubation (Figure 2.9e), during which time the [^{32}P]2′3′-cGAMP was not hydrolyzed or modified (Figure 2.9f). 2′3′-cGAMP uptake was most efficient at a pH range of 7.5 to 8.0 in both THP-1 and U937 cells (Figure 2.9g, h), consistent with a neutral pH optimum for SLC19A1[102,103,105].

[^{3}H]-methotrexate uptake assays

Tritium-labelled methotrexate (Vitrax cat. no. VT 145) had a specific activity of 40.6 Ci/mmole. Uptake of [^{3}H]-methotrexate in SLC19A1-knockdown and SLC19A1-overexpressing cells was performed in RPMI complete medium. [^{3}H]-methotrexate competition assays were performed in MHS buffer (20 mM HEPES, 235 mM sucrose adjusted to pH7.4 using MgO). Cells were washed and resuspended in the appropriate buffer to 4×10^6 cells per ml. Cells (10^6 per condition) were exposed to 12.3 nM [^{3}H]-methotrexate (1.25 μCi) at 37 °C and 5% CO_2 for the duration indicated in the figure legends. Cells were subsequently washed four times in ice cold PBS to stop uptake and remove extracellular [^{3}H]-methotrexate. Cells were lysed in 250 μl ice cold water and 200 μl was mixed with 4 ml scintillation liquid. Fifty microlitres was used for protein quantification using the bicinchoninic acid (BCA) assay (Thermo Scientific cat. no. 23235). Radioactivity (counts per minute) was measured for 3 min per sample using by liquid scintillation counting using a LS6500 Liquid Scintillation Counter (Beckman Coulter). Counts per minute were normalized to total

protein. For competition assays, cells were incubated for 15 min at 37 °C and 5% CO_2 with the indicated ligand in MHS buffer before addition of [^{3}H]-methotrexate.

Enzyme-linked immunosorbent assay

Cells were stimulated with 2′3′-RR CDA (2 μg ml^{-1}) for 20 h. Supernatant was collected and centrifuged to remove cells. CXCL10 was quantified in the supernatant using the CXCL10 ELISA kit (BioLegend cat. no. 439904) according to the manufacturer's recommendations.

Digitonin permeabilization

Cells were counted, washed and resuspended to 2 × 10^6 cells per ml. Cells (10^6 per condition) were permeabilized using 5 μg ml^{-1} digitonin (Sigma cat. no. D-141; stock dissolved in H_2O) and stimulated with 2′3′-RR CDA (10 μg ml^{-1}) and the indicated SLC19A1 (competitive) inhibitor for 2 h at 37 °C and 5% CO_2. Cells were subsequently washed in ice cold PBS, lysed in RIPA buffer and used for western blot protein analysis.

Protein expression and purification

Full-length human SLC19A1 cDNA with a C-terminal 8× His-tag was subcloned into a dual promoter lentiviral vector (see above). Recombinant His-tagged SLC19A1 was expressed using a FreeStyle 293 Expression System. In brief, 293F cells (1 × 10^6 cells per ml) grown in FreeStyle 293 medium supplemented with GlutaMax (GIBCO) were transfected with the SLC19A1 expression construct (1 μg plasmid DNA per ml of cells) using PEI transfection reagent. Transfected cells were grown for 72 h in a shaking incubator at 37 °C in 5% CO_2. Three days after transfection, the cells were collected by centrifugation and washed in DBPS. Cell pellets were then re-suspended in lysis buffer (25 mM Tris pH 8.0, 150 mM NaCl, 1 mM phenylmethylsulfonyl fluoride) supplemented with HALT Protease and Phosphatase Inhibitor Cocktail (Thermo Scientific) and lysed by sonication. The cell lysate was supplemented with 2% (w/v) *n*-dodecyl-β-D-maltoside (DDM) and rotated for 2 h at 4 °C. The cell lysates were centrifuged at 15,000 r.p.m. for 1 h at 4 °C to remove cell debris, and the detergent-soluble fraction was incubated with HisPur Ni-NTA resin for 1 h at 4 °C. The resin was washed with 100 column volumes of wash buffer (25 mM Tris pH 6.0, 150 mM NaCl, 30 mM imidazole, 5% glycerol (v/v) and 0.05% DDM (w/v)), and bound proteins were eluted in elution buffer (25 mM Tris pH 6.0, 150 mM NaCl, 300 mM imidazole, 5% glycerol (v/v) and 0.05% DDM (w/v)). The resulting proteins were analysed by SDS–PAGE followed by Coomassie staining and immunoblotting to confirm expression and purification of His-tagged SLC19A1.

Recombinant cGAS, DisA, mSTING-CTD, and mRECON were expressed and purified as previously described[103,104,106]. In brief, plasmids for cGAS, DisA, mSTING-CTD, and mRECON expression were transformed into Rosetta (DE3) pLysS chemically competent cells. Overnight cultures of the resulting transformed bacteria were inoculated into 1.5 l of LB broth at a 1:100 dilution. Bacterial cultures were grown at 37 °C to OD_{600} 0.5 followed by overnight induction at 18 °C with 0.5 mM isopropyl β-D-1-thiogalactopyranoside. Cells were collected and lysed in PBS supplemented with 1 mM PMSF and soluble protein was purified using nickel-affinity chromatography followed by gel-filtration chromatography (S-300, GE Healthcare). After SDS–

PAGE analysis, the purified proteins were concentrated in storage buffer (40 mM Tris pH 7.5, 100 mM NaCl, 20 mM $MgCl_2$ and 25% glycerol (v/v)) and stored at –80 °C.

Synthesis of 2′3′-cGAMP Sepharose

2′3′-cGAMP was enzymatically synthesized using recombinant cGAS as previously described[12,104]. Approximately, 100 mg of purified 2′3′-cGAMP was dissolved in PBS to 200 μM. The pH of the solution was adjusted to 7.5 with NaOH, and the resulting solution was added directly to washed epoxy-activated Sepharose and incubated at 56 °C for 2 days. The Sepharose was washed and the absorbance spectrum of 50% slurry was measured to ensure nucleotide coupling. HPLC analysis of the remaining uncoupled nucleotide ensured no degradation of 2′3′-cGAMP occurred during the two-day incubation. The remaining epoxy groups were blocked with ethanolamine following the instructions provided by GE. In parallel with this blocking step, fresh epoxy-activated Sepharose was also treated with ethanolamine to generate control resin.

2′3′-cGAMP pulldowns

Following nickel affinity purification, recombinant His-tagged SLC19A1 was incubated with 100 μl of ethanolamine- or 2′3′-cGAMP-conjugated Sepharose beads for 4 h at 4 °C with rotation, as previously described[104,106]. Beads were washed three times with wash buffer (25 mM Tris pH 6.0, 150 mM NaCl, 5% glycerol (v/v) and 0.05% DDM (w/v)), and bound proteins were eluted by boiling in SDS–PAGE sample loading buffer for 5 min at 95 °C. The soluble fraction was then removed and analysed by SDS–PAGE followed by Coomassie blue staining and immunoblotting. As a positive control, recombinant His-tagged mSTING-CTD was incubated with ethanolamine- or 2′3′-cGAMP-conjugated Sepharose beads, as described above (Figures 2.10g and 2.11d). Beads were washed three times with binding buffer, and then boiled in SDS–PAGE sample loading buffer for 5 min at 95 °C. The soluble fraction was then analysed by SDS–PAGE followed by Coomassie blue staining.

Cell lysis and immunoblotting

For immunoblotting of SLC19A1, cells were lysed and proteins were separated by SDS–PAGE as described in '2′3′-cGAMP pulldowns'. Proteins separated by SDS–PAGE were transferred onto nitrocellulose membranes (Bio-Rad) at 30 V overnight at 4 °C. Membranes were then air-dried for 1 h and blocked in 5% Blotto, non-fat milk (NFM, Santa Cruz Biotechnology) in 1× TBS. Membranes were probed in 5% bovine serum albumin (Fisher) in 1× TBS-T with SLC19A1 Picoband antibody (Boster Bio).

For protein detection using all other antibodies, cells were counted, washed with PBS and lysed in RIPA buffer (25 mM Tris-HCl pH 7.5, 150 mM NaCl, 1 mM EDTA, 1% NP-40 and 0.1% SDS) including cOmplete ULTRA protease inhibitors (Sigma-Aldrich cat. no. 05892791001), phosphatase inhibitors (Biomake, cat. no. B15001) and 50 mM DTT. Cell lysates were mixed with 4× NuPage LDS sample buffer (Invitrogen cat. no. NP0007), pulse sonicated and incubated at 75 °C for 5 min. Lysates were loaded onto Bolt 4–12% Bis-Tris Plus SDS–PAGE gels (Invitrogen cat. no. NW04125BOX). Proteins separated by SDS–PAGE were transferred onto Immobilon-FL PVDF membranes (EMD Millipore) at 100 V for 1 h at 4 °C. Membranes were blocked in 4%

NFM,and probed in 1% NFM overnight at 4 °C with primary antibody. Membranes were subsequently washed three times in 1× TBS-T and probed with secondary antibody for 1 h at room temperature while protected from light. Membranes were washed two times in TBS-T, once in TBS and blots were imaged using an Odyssey CLx System (LI-COR).

Mice

Male and female C57BL/6J mice (4–20 weeks old) were obtained from The Jackson Laboratory. All of the mice were maintained in specific-pathogen-free conditions by the Department of Comparative Medicine at the University of Washington School of Medicine or at the University of California, Berkeley. All experimental procedures using mice complied with all relevant ethical regulations and were approved by the Institutional Animal Care and Use Committee of the University of Washington or the University of California, Berkeley, and were conducted in accordance with institutionally approved protocols and guidelines for animal care and use.

Isolation of mouse splenocytes and bone-marrow-derived dendritic cells and macrophages

For isolation of mouse splenocytes, spleens were removed from mice, strained through a 70-μm cell strainer, and homogenized into a single-cell suspension using ice-cold PBS supplemented with 3% FCS. Red blood cells were lysed by resuspending spleen cells in Red Blood Cell Lysing Buffer (Sigma) and incubating on ice for 10 min. Splenocytes were washed, resuspended in RPMI 1640 medium (GIBCO) supplemented with 10% (v/v) heat-inactivated FBS (HyClone), 10 mM HEPES, 1 mM sodium pyruvate, 2 mM L-glutamine (Thermo Fisher), 100 U ml^{-1} penicillin and 100 μg ml^{-1} streptomycin, and used immediately for [^{32}P]2′3′-cGAMP uptake assays.

For generation of bone-marrow-derived macrophages (BMMs) and dendritic cells (BMDCs), bones from the hind legs were removed and crushed to release the bone marrow. Bone marrow was washed in complete RPMI medium and filtered using a 70-μm cell strainer. Cells were incubated in ammonium–chloride–potassium buffer for 2 min to remove red blood cells. Cells were subsequently resuspended in RPMI 1640 supplemented with 10% (v/v) heat-inactivated FBS (HyClone), 10 mM HEPES, 1 mM sodium pyruvate, 2 mM L-glutamine (Thermo Fisher), 100 U ml^{-1} penicillin, 100 μg ml^{-1} streptomycin, and 5 ng ml^{-1} GM-CSF (Preprotech, cat. no. 315-03) to generate BMDCs or M-CSF conditioned medium to generate macrophages. Cells were transduced with shRNA-encoding lentiviruses on day 2 and 3 after bone-marrow isolation and selected using 7 μg ml^{-1} puromycin for 3 days starting at day 5 after bone marrow isolation. Medium was refreshed every other day. Nine days after bone marrow isolation, non-adherent BMDCs or adherent BMM cells were collected. Cells were stimulated with 5 μg ml^{-1} 2′3′-RR CDA for 5 h before RNA extraction.

Isolation of human peripheral blood mononuclear cells

Whole blood from healthy, human donors was collected in 10-ml EDTA blood tubes (Beckton Dickinson) from healthy adults with written informed consent. Bulk PBMCs were isolated using SepMate tubes (STEMCELL Technologies) according to the manufacturer's instructions. The remaining cells were washed in PBS, resuspended in RPMI 1640 medium (GIBCO) supplemented with 10% (v/v) heat-inactivated FBS (HyClone), 10 mM HEPES, 1 mM sodium pyruvate, 2

mM L-glutamine (Thermo Fisher), 100 U ml^{-1} penicillin, 100 μg ml^{-1} streptomycin, and used immediately for [^{32}P]2′3′-cGAMP uptake assays. The isolation of primary human cells complied with all relevant ethical regulations and was conducted under a protocol from K. B. Elkon which was approved by the University of Washington Institutional Review Board.

Figures

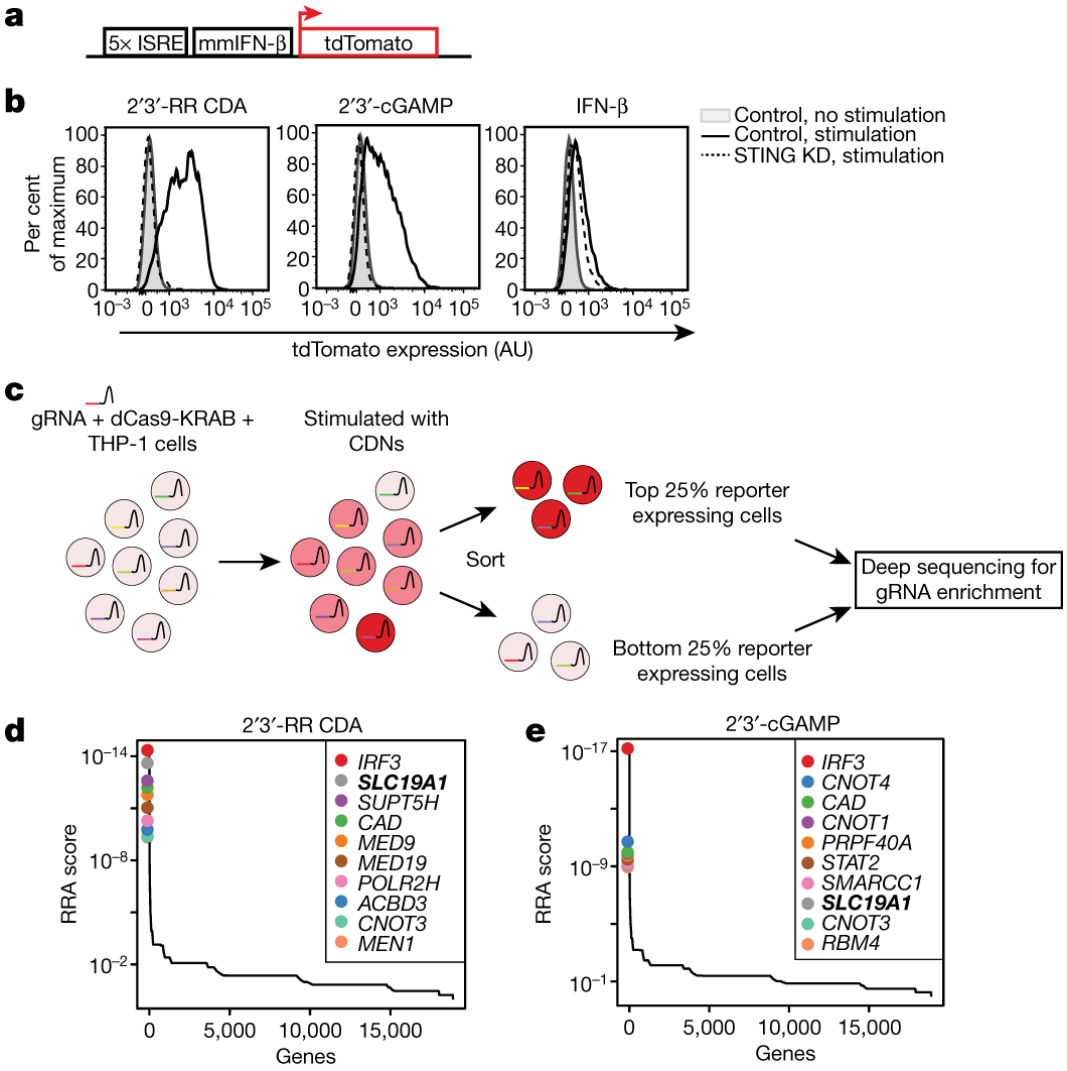

Fig. 2.1: Genome-wide CRISPRi screen for host factors necessary for stimulation by CDNs. **(a)** Schematic overview of the tdTomato reporter construct. tdTomato expression is driven by interferon-stimulatory response elements (ISRE) followed by a mouse minimal interferon-β (mmIFN-β) promoter. **(b)** Control THP-1 cells and *STING*-depleted (STING KD) THP-1 cells were incubated with 2′3′-RR CDA (1.67 μg ml^{-1}), 2′3′-cGAMP (10 μg ml^{-1}) or human IFN-β (100 ng ml^{-1}). After 20 h, tdTomato reporter expression was analysed by flow cytometry. Data are representative of three independent experiments with similar results. **(c)** Schematic overview of the genome-wide CRISPRi screen. A genome-wide library of CRISPRi gRNA-expressing THP-1 cells was stimulated with CDNs. Twenty hours after stimulation, cells were sorted into a tdTomato^{low} group (lowest 25% of cells) and a tdTomato^{high} group (highest 25% of cells). DNA from the sorted cells was deep-sequenced to reveal gRNA enrichment in the two groups. **(d-e)** Distribution of the robust rank aggregation (RRA) score in the comparison of hits enriched in the tdTomato^{low} versus tdTomato^{high} groups of THP-1 cells stimulated with 2′3′-RR CDA (d) or 2′3′-cGAMP (e). Each panel represents combined results of two independent screens. AU, arbitrary units.

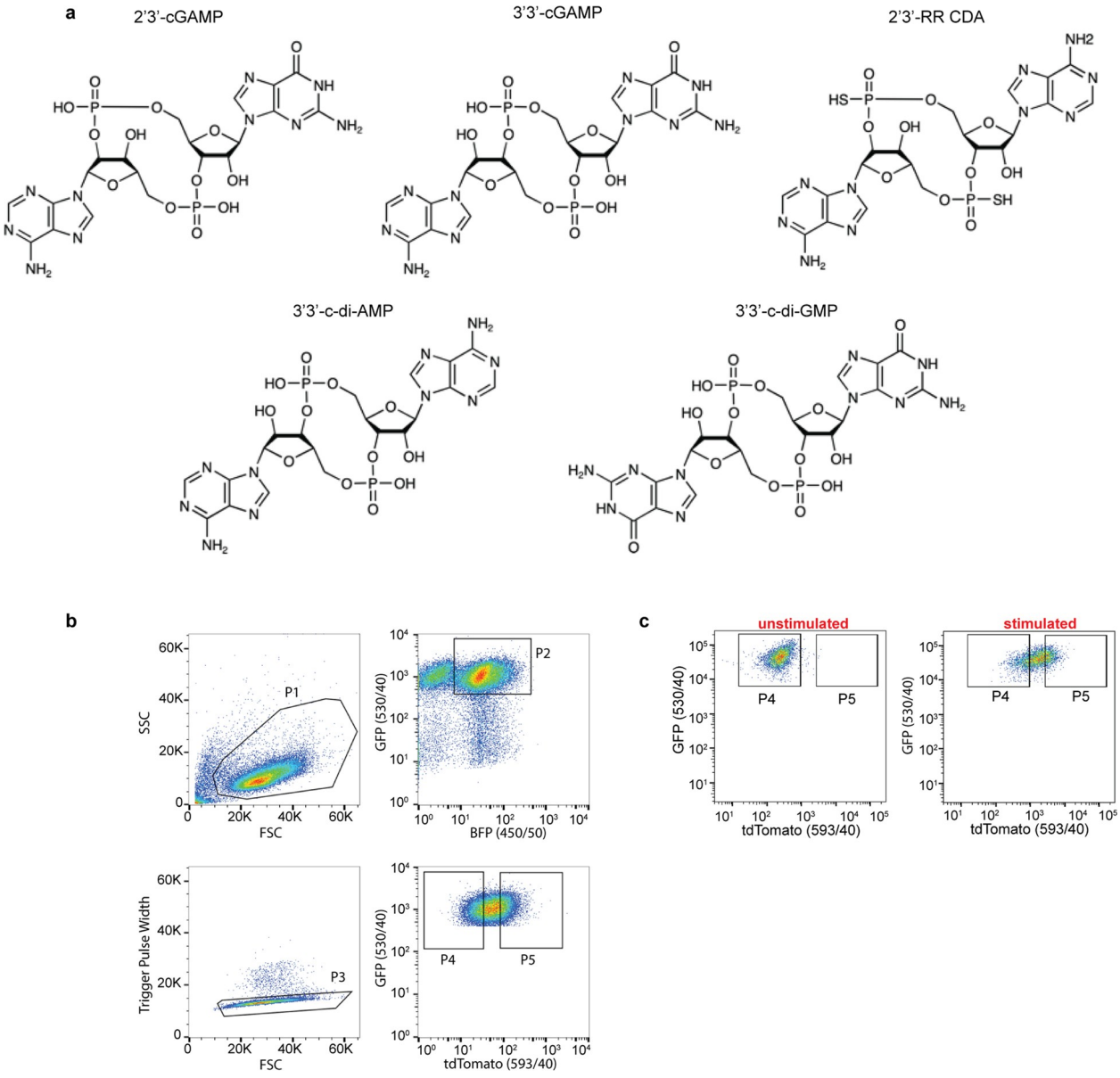

Fig. 2.2: Structures of CDNs used in this study and gating strategy for the genome-wide CRISPRi screens.

(**a**) Structures of the CDNs used in this study. (**b**) Representative gating strategy for flow-cytometry-based sorting of the CRISPRi library of reporter-expressing THP-1 cells stimulated with CDNs. Cells were gated on the basis of their forward scatter (FSC) and side scatter (SSC) using gate P1. The P1 cells were subsequently selected for co-expression of BFP (fluorescent marker for the CRISPRi gRNAs) and GFP (marker for the expression of the reporter construct) (gate P2). Gate P3 excluded cell doublets present among P2 cells. Gate P4 selected for the lowest 25% of cells with respect to tdTomato expression and gate P5 selected for the highest 25%. **c**, Representative flow cytometry dot plots showing tdTomato expression in unstimulated cells or in cells stimulated for 20 h with cells for 20 h with CDN (2′3′-RR CDA). Data are representative of $n = 3$ biological replicates.

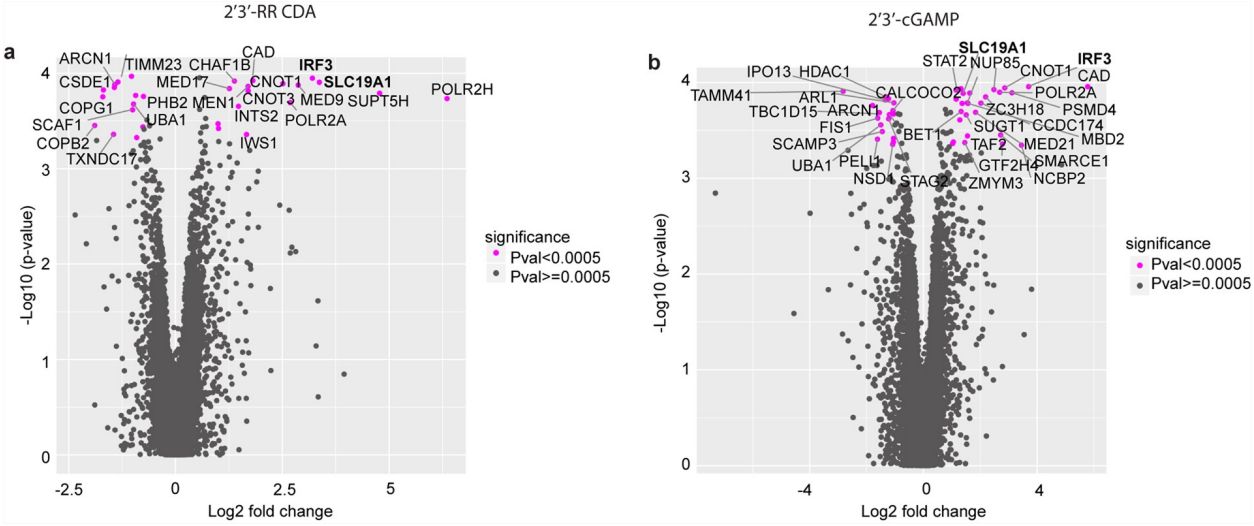

Fig. 2.3: Results of genome-wide CRISPRi screens for host factors crucial for CDN stimulation.

(a-b) Volcano plots of the gRNA-targeted genes enriched or depleted in the tdTomato reporter-low versus reporter-high groups after stimulation with 2′3′-RR CDA (a), or 2′3′-cGAMP (b). Each panel represents the combined results of two independent screens. Calculations of phenotypes and Mann–Whitney P values were performed as described in Methods.

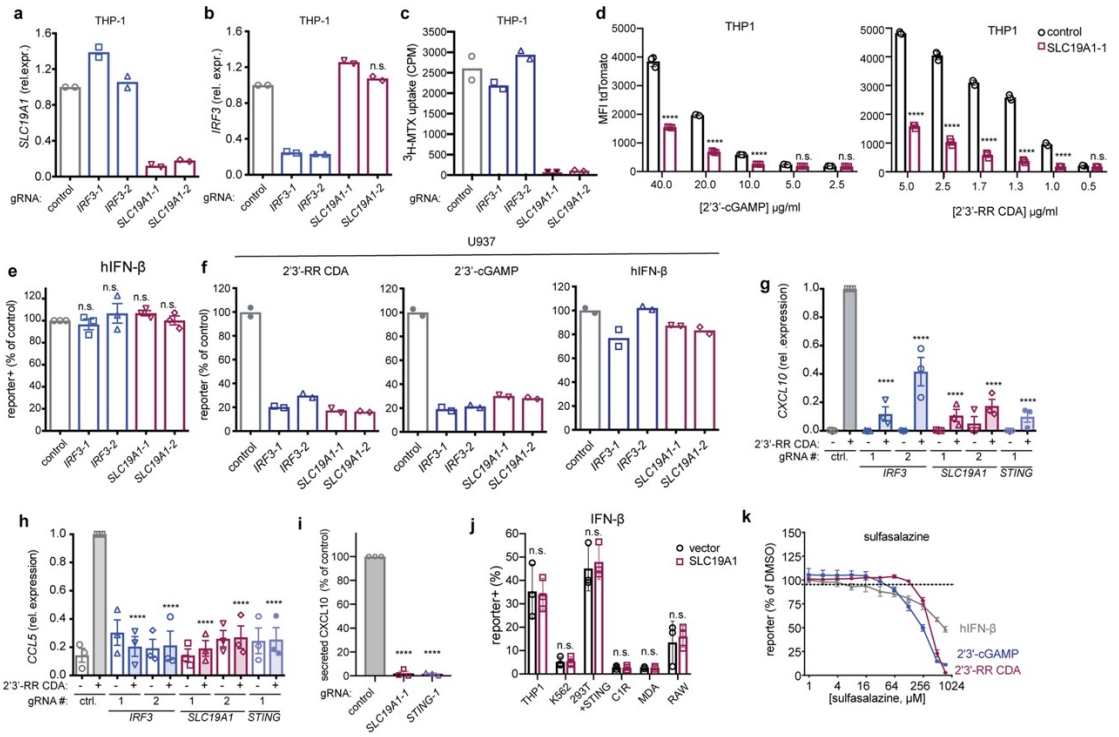

Fig. 2.4: SLC19A1 is critical for CDN-induced gene expression.

(**a**-**b**) mRNA expression levels of *SLC19A1* (a) or *IRF3* (b) in THP-1 cells expressing a CRISPRi vector and a control non-targeting gRNA or gRNAs targeting *IRF3* or *SLC19A1* (two gRNAs each). (**c**) THP-1 cells described in a and b were exposed to [^{3}H]-methotrexate. After 1 h, radioactivity (in counts per minute, cpm) in lysates of cell pellets was measured. Counts were normalized to protein concentrations in the lysate. (**d**) THP-1 cells expressing a control gRNA or *SLC19A1*-targeting gRNA were exposed to indicated concentrations of 2′3′-RR CDA or 2′3′-cGAMP. After 20 h, the mean fluorescence intensity (MFI) of tdTomato was quantified by flow cytometry. (**e**) THP-1 cells expressing the indicated CRISPRi gRNAs or non-targeting gRNA (control), were stimulated with IFN-β (100 ng ml^{-1}). After 18–22 h, tdTomato expression was quantified as in Fig. 2.5a. (**f**) U937 cells expressing the indicated CRISPRi gRNAs or non-targeting gRNA (control), were stimulated with 2′3′-RR CDA (1.67 μg ml^{-1}), 2′3′-cGAMP (15 μg ml^{-1}) or IFN-β (100 ng ml^{-1}). After 18–22h, tdTomato expression was quantified as in Fig. 2.5a. (**g**-**h**) Induction of *CXCL10* mRNA (g) or *CCL5* mRNA (h) in control (non-targeting gRNA) THP-1 cells or THP-1 cells expressing the indicated CRISPRi gRNAs after 5 h stimulation with 5 μg ml^{-1} 2′3′-RR CDA. (**i**) CXCL10 protein expression in the supernatant of indicated gRNA-expressing THP-1 cells after exposure to 2 μg ml^{-1} 2′3′-RR CDA for 20 h. (**j**) Various cell lines expressing a control vector or an *SLC19A1* expression vector were stimulated with IFN-β (100 ng ml^{-1}). After 18–22 h, tdTomato expression was quantified as in Fig. 2.5a. (**k**) THP-1 cells were incubated with increasing concentrations of the non-competitive inhibitor sulfasalazine or DMSO as vehicle control, before stimulation with 2′3′-RR CDA (1.25 μg ml^{-1}), 2′3′-cGAMP (15 μg ml^{-1}) or IFN-β (100 ng ml^{-1}). After 18–22 h, tdTomato expression was quantified as in Fig. 2.5a. The data were normalized to the DMSO controls. In a–c and e–f, mean of $n = 2$ biological replicates are shown. In d, g–k, mean ± s.e.m. of $n = 3$ biological replicates are shown. Statistical analyses were performed to compare each cell line to the control using a one-way ANOVA followed by post hoc Dunnett's test (d, g–i) or two-way ANOVA followed by uncorrected Fisher's least significant difference tests (j). ****$P \leq 0.0001$; n.s., not significant.

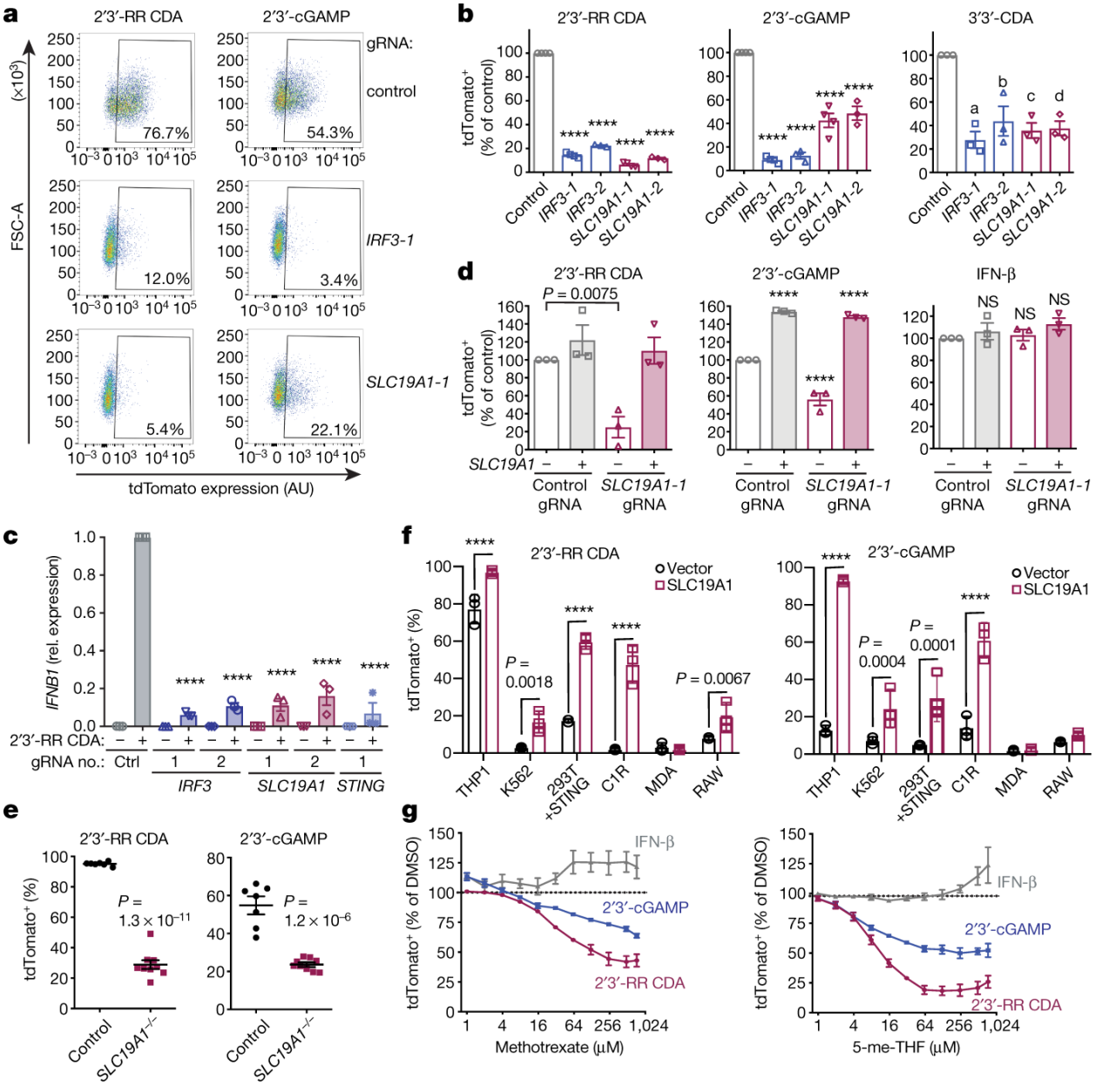

Fig. 2.5: SLC19A1 is required for CDN-induced reporter expression.
(a) dCas9–KRAB-expressing THP-1 cells transduced with non-targeting gRNA (control), IRF3-1 gRNA or SLC19A1-1 gRNA were exposed to 2′3′-RR CDA (1.67 μg ml−1) or 2′3′-cGAMP (15 μg ml−1). Twenty hours later, tdTomato expression was analysed by flow cytometry. Representative dot plots of three independent experiments are shown. **(b)** THP-1 cells expressing the indicated CRISPRi gRNAs or non-targeting gRNA (control), were stimulated with 2′3′-RR CDA (1.67 μg ml−1), 2′3′-cGAMP (10 μg ml−1), or 3′3′-CDA (20 μg ml−1). After 18–22 h, tdTomato expression was quantified as in a. **(c)** Induction of IFNB mRNA in control (non-targeting gRNA) THP-1 cells or THP-1 cells expressing the indicated CRISPRi gRNAs after 5 h stimulation with 5 μg ml−1 2′3′-RR CDA. Rel., relative. **(d)** Control THP-1 cells and THP-1 cells expressing SLC19A1-1 gRNA transduced with SLC19A1 were stimulated with 2′3′-RR CDA (1.67 μg ml−1), 2′3′-cGAMP (15 μg ml−1) or IFN-β (100 ng ml−1) and analysed as in a. **(e)** Control THP-1 cells

(n = 7 independent clonal lines) and SLC19A1−/− cells (n = 9 independent clonal lines) were exposed to 2′3′-RR CDA (2.22 μg ml−1) or 2′3′-cGAMP (10 μg ml−1) and reporter tdTomato expression was analysed as in a. Data are mean ± s.e.m. **(f)** Various cell lines expressing a control vector or an SLC19A1 expression vector were stimulated and analysed as in b. **(g)** THP-1 cells were incubated with increasing concentrations of the competitive inhibitors methotrexate, 5-me-THF or DMSO as vehicle control, before stimulation with 2′3′-RR CDA (1.25 μg ml−1), 2′3′-cGAMP (15 μg ml−1) or IFN-β (100 ng ml−1). Cells were analysed as in a. For each stimulant, the data were normalized to the DMSO controls. In b–d, f, g, data are mean ± s.e.m. of n = 3 biological replicates. Statistical analyses were performed using one-way analysis of variance (ANOVA) followed by post hoc Dunnett's test for the comparison to stimulated control cells (b–d), unpaired two-tailed Student's t-tests (e) or two-way ANOVA followed by uncorrected Fisher's least significant difference tests (f). aP = 0.0002, bP = 0.0013, cP = 0.0005, dP = 0.0006 and ****P ≤ 0.0001. NS, not significant.

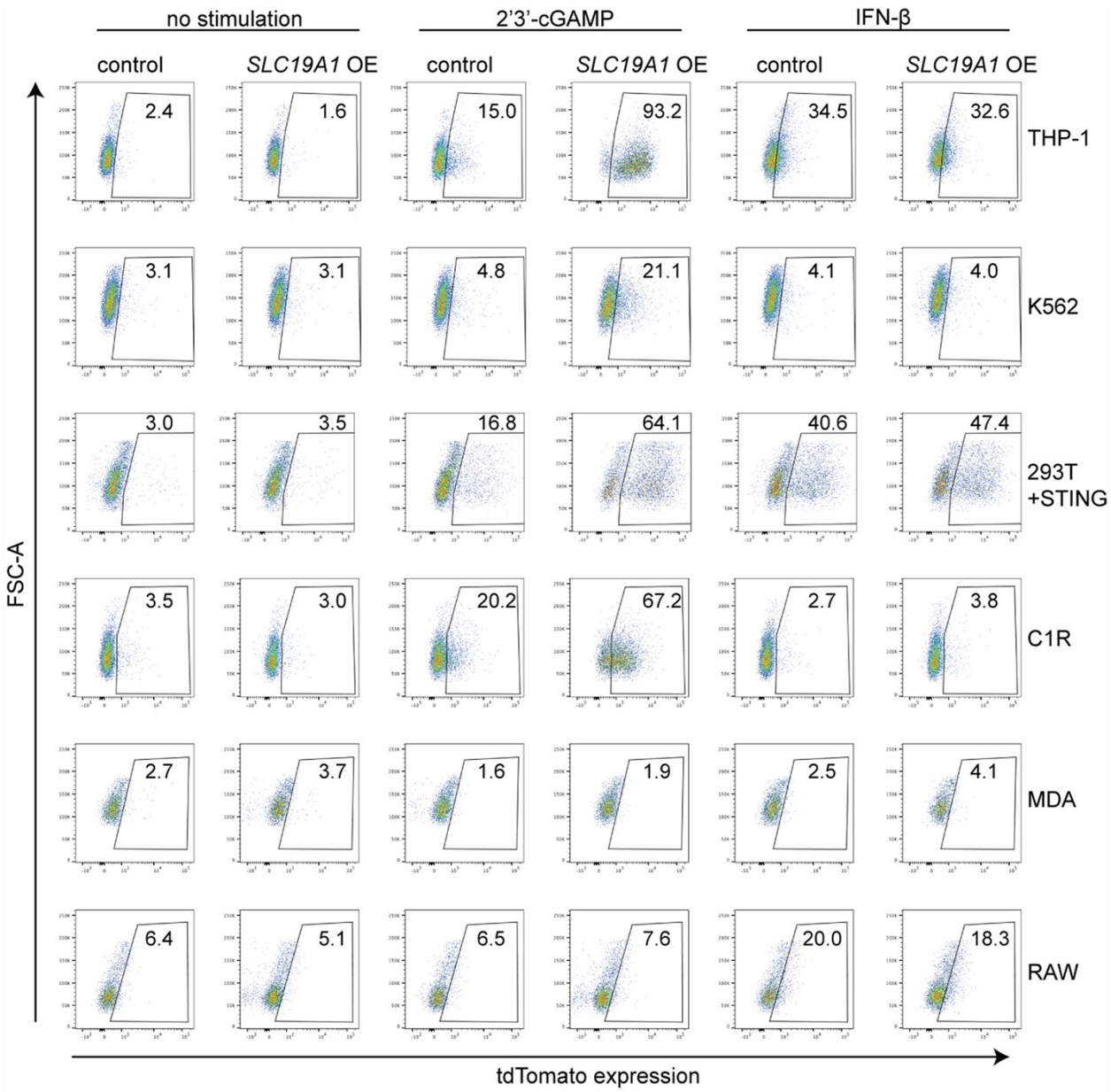

Figure 2.6: SLC19A1 overexpression increases the response to CDNs in various cell lines. Various cell lines expressing a control vector or an SLC19A1 expression vector (SLC19A1 OE) stimulated with 2′3′-cGAMP (10 μg ml−1) (e) or IFN-β (100 ng ml−1) (or 100 ng ml−1 mouse IFN-β in the case of RAW cells). After 20 h, reporter expression was quantified by flow cytometry. Representative flow plots of n = 3 biological replicates shown in Fig. 2.4j and Fig. 2.5f.

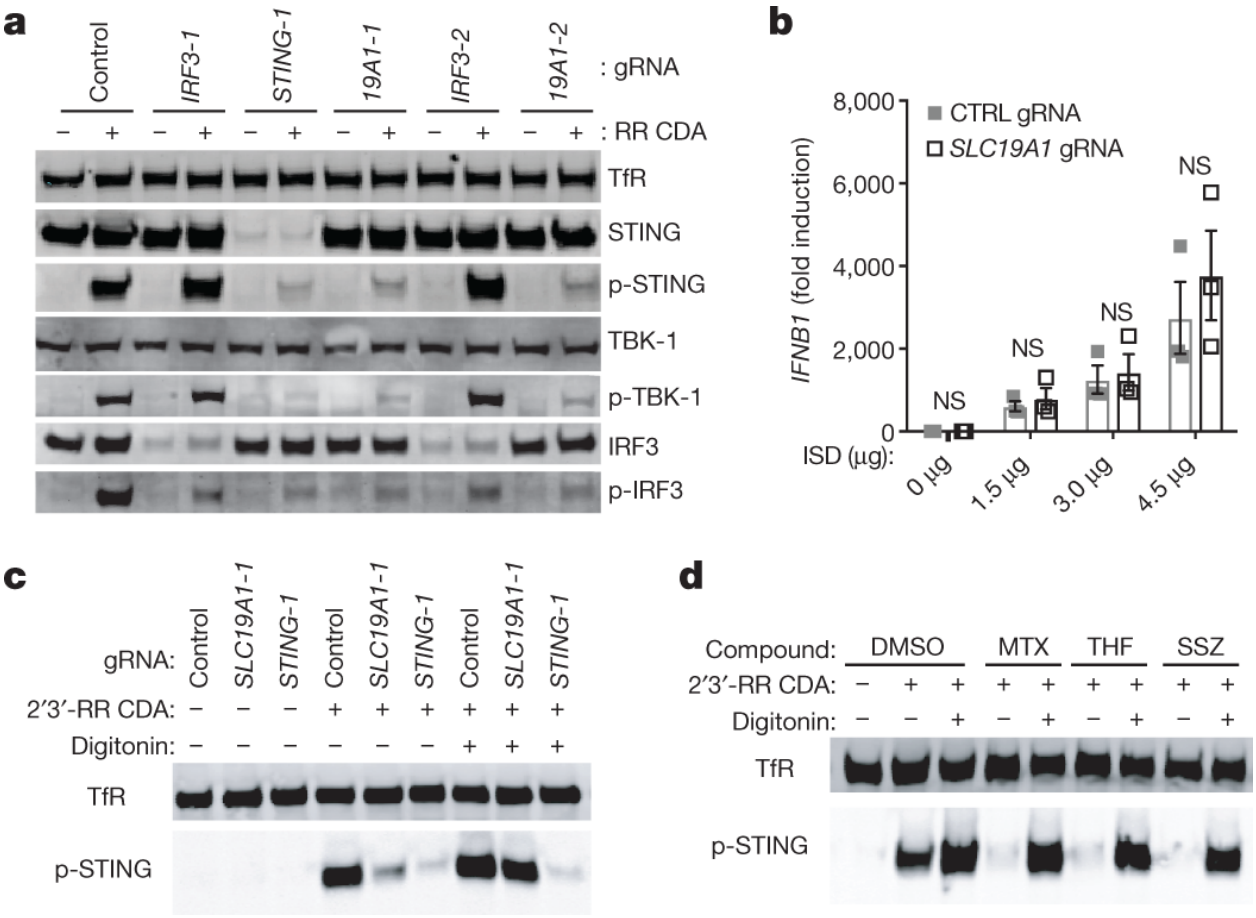

Figure 2.7: SLC19A1 is critical for STING-dependent responses to exogenous CDNs but not when CDNs are provided intracellularly.

(**a**) Immunoblot analysis of protein expression and phosphorylation in control THP-1 cells or THP-1 cells expressing the indicated CRISPRi gRNAs. Cells were stimulated for 2 h with 10 μg ml^{-1} 2′3′-RR CDA (RR CDA) or left unstimulated. p-TBK1, TKB1 phosphorylated on Ser172; p-IRF3, IRF3 phosphorylated on Ser396; p-STING, STING phosphorylated on Ser366. (**b**) Control (CTRL) THP-1 cells or SLC19A1-depleted THP-1 cells were transfected with increasing amounts of interferon-stimulatory DNA (ISD) for 3 h and induction of *IFNB1* mRNA was measured by quantitative PCR with reverse transcription (RT–qPCR). (**c**) Cells were stimulated as in a in the absence or presence of digitonin (5 μg ml^{-1}). (**d**) Control THP-1 cells were stimulated as in c, with the addition of the indicated SLC19A1 inhibitors (all at 750 μM): methotrexate (MTX), 5-me-THF (THF), sulfasalazine (SSZ) or DMSO (as vehicle control). TfR, transferrin receptor. Data in a, c, and d are representative of $n = 3$ biological replicates. In b, data are mean ± s.e.m. of $n = 3$ biological replicates and statistical analyses were performed using two-way ANOVA followed by post hoc Sidak's test.

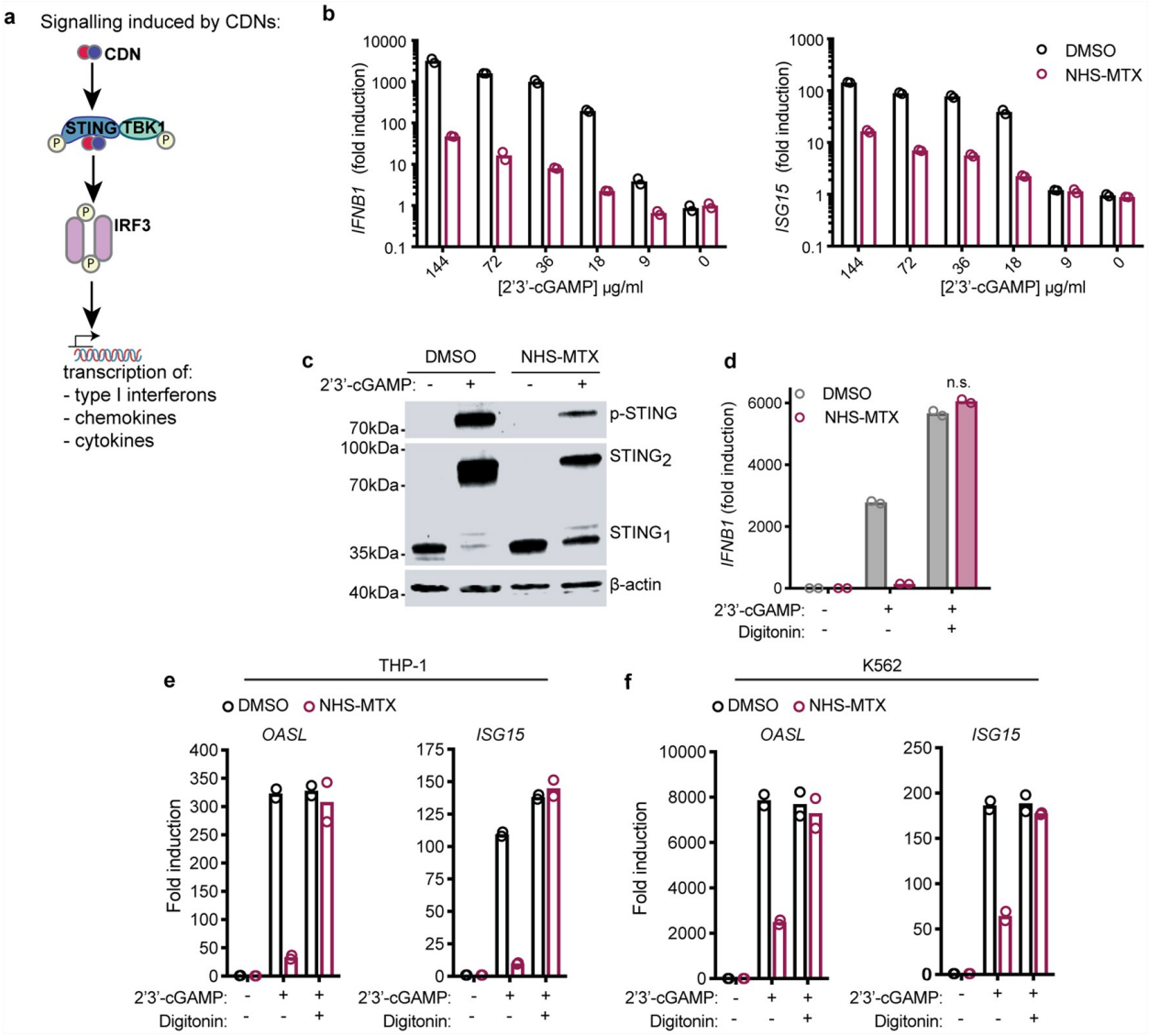

Figure 2.8: Covalent inhibition of SLC19A1 by NHS–methotrexate blocks STING activation. **(a)** Schematic overview of CDN-induced phosphorylation (P) of STING and downstream effectors TBK1 and IRF3. **(b)** THP-1 monocytes pre-treated with DMSO or NHS–methotrexate (5 µM) were treated with varying concentrations of 2′3′-cGAMP for 4 h, and the amounts of IFNB1 or ISG15 transcripts were measured by RT–qPCR. **(c)** Semi-native PAGE and immunoblot analysis of STING dimerization and phosphorylation in DMSO and NHS–methotrexate (5 µM) pre-treated THP-1 monocytes stimulated with 100 µM 2′3′-cGAMP for 4 h. **(d)** DMSO and NHS–methotrexate (5 µM)-treated THP-1 monocytes were treated with 100 µM 2′3′-cGAMP in the presence and absence of digitonin (5 µg ml−1) for 4 h and the induction of *IFNB1* mRNA was measured by RT–qPCR. **(e-f)** DMSO and NHS–methotrexate (5 µM) pre-treated THP-1 monocytes (e) or K562 cells (f) were stimulated for 4 h with 100 µM 2′3′-cGAMP, or not, in the presence or absence of digitonin (5 µg ml^{-1}), and the induction of *OASL* and *ISG15* mRNA was measured by RT–qPCR. In b, d–f, data are mean of n = 2 technical replicates and are representative of 3 independent experiments with similar results. In c, data are representative of three independent experiments with similar results.

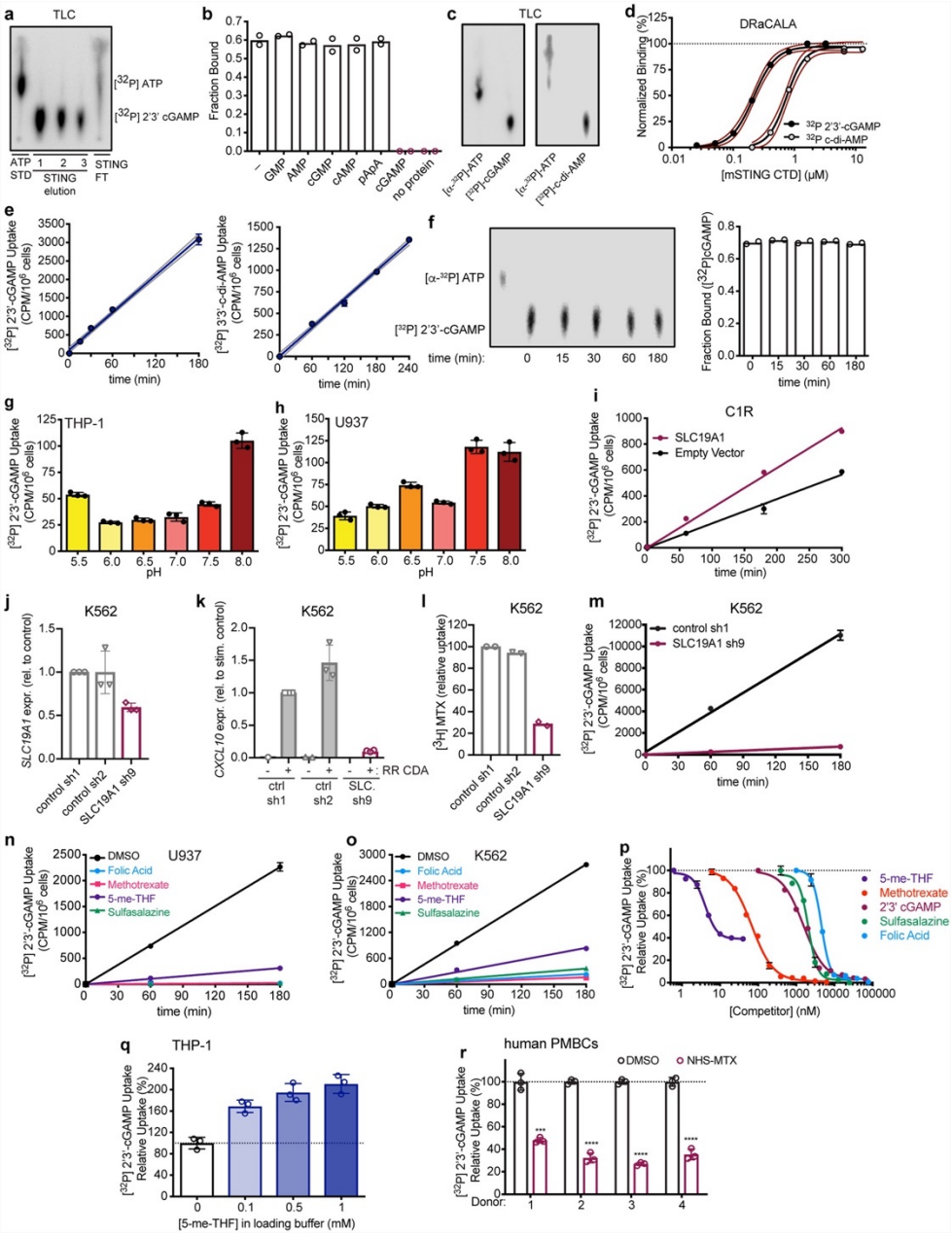

Figure 2.9: SLC19A1 is critical for CDN uptake in human cell lines and primary cells.
(**a**) TLC analysis of [^{32}P]ATP standard (STD) and enzymatically synthesized [^{32}P]2′3′-cGAMP (2′3′-cGAMP was purified on STING resin). Unbound nucleotides flowed through the resin (STING FT). Following four washes, the bound [^{32}P]2′3′-cGAMP was eluted over three fractions. (**b**) DRaCALA binding analysis of [^{32}P]2′3′-cGAMP to STING C-CTD in the presence of competing unlabelled nucleotides (200 μM). (**c**) TLC analysis of [^{32}P]ATP and enzymatically synthesized [^{32}P]2′3′-cGAMP and [^{32}P]-c-di-AMP. (**d**) Binding titration of [^{32}P]2′3′-cGAMP or [^{32}P]c-di-AMP to mSTING CTD, determined with DRaCALA assays. Red lines represent the 95% confidence interval for the nonlinear regression. (**e**) Time course of [^{32}P]2′3′-cGAMP (left) or [^{32}P]3′3′-CDA (right) uptake in THP-1 monocytes. (**f**) TLC analysis (left) and STING-binding (DRaCALA) (right) of [^{32}P]ATP standard, or [^{32}P]2′3′-cGAMP recovered from supernatants of

THP-1 monocytes at the indicated time points. **(g-h)**, Effect of cell culture medium pH on [^{32}P]2′3′-cGAMP uptake in THP-1 monocytes (g) or U937 monocytes (h). **(i)** Time course of [^{32}P]2′3′-cGAMP uptake by CIR cells transduced with empty vector or *SLC19A1* expression vector. **(j)** mRNA expression levels of *SLC19A1* (SLC.) in K562 cells expressing control shRNAs (sh1 and sh2) or an *SLC19A1*-targeting shRNA (sh9). (**k**) mRNA expression levels of *CXCL10* in K562 cells described in j, stimulated with 5 μg ml^{-1} 2′3′-RR CDA (RR CDA) for 5 h. (**l**) [^{3}H]-methotrexate uptake in K562 cells described in **j**, 1 h after exposure to [^{3}H]-methotrexate. (**m**) Time course of [^{32}P]2′3′-cGAMP uptake in K562 cells described in j. (**n**) Time course of [^{32}P]2′3′-cGAMP uptake in U937 monocytes in the presence or absence of 500 μM competing, unlabelled (anti-)folates and sulfasalazine. (**o**) Time course of [^{32}P]2′3′-cGAMP uptake in K562 cells in the presence or absence of 500 μM competing, unlabelled (anti-)folates or sulfasalazine. (**p**) Competition uptake assay of [^{32}P]2′3′-cGAMP uptake in THP-1 cells in the presence of varying concentrations of competing, unlabelled 5-me-THF (IC_{50} = 4.10 ± 0.16 nM), methotrexate (IC_{50} = 54.83 ± 5.08 nM), 2′3′-cGAMP (IC_{50} = 1.89 ± 0.11 μM), sulfasalazine ((IC_{50} = 2.06 ± 0.17 μM), and folic acid (IC_{50} = 4.79 ± 0.08 μM). (**q**) *Trans*-stimulation of [^{32}P]2′3′-cGAMP influx in THP-1 cells by 5-me-THF. Cells were preloaded with indicated concentrations of 5-me-THF for 30 min. Cells were washed and incubated with [^{32}P]2′3′-cGAMP for one hour. (**r**) Normalized [^{32}P]2′3′-cGAMP uptake after 1 h in DMSO or NHS–methotrexate (5 μM)-treated human PBMCs from four healthy donors. In a, c, data are representative of three independent experiments with similar results. In b, data are mean of n = 2 technical replicates and are representative of 3 independent experiments. In d, f, data are mean of n = 2 technical replicates and are representative of 2 independent experiments. In e, m, data are mean ± s.d. of n = 3 technical replicates and are representative of 3 independent experiments. In g–i and n–r, data are means ± s.d. of n = 3 technical replicates and are representative of 2 independent experiments. In j, k, data are mean ± s.e.m. of n = 3 biologically independent experiments. In l, data are mean of n = 2 biologically independent experiments.

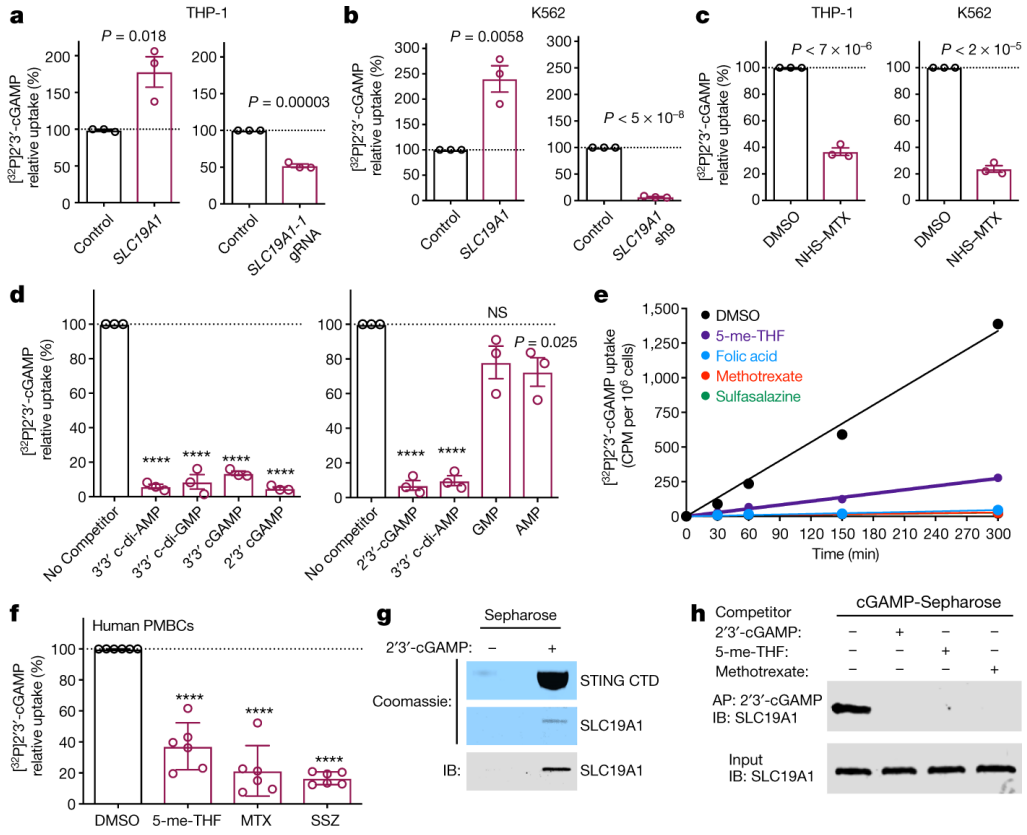

Fig. 2.10: SLC19A1 transports CDNs.

(**a**) Normalized [^{32}P]2′3′-cGAMP uptake after 1 h by THP-1 monocytes transduced with empty vector (control) or *SLC19A1* expression vector (left) or with a non-targeting control CRISPRi gRNA or *SLC19A1* CRISPRi gRNA (right). (**b**) Normalized [^{32}P]2′3′-cGAMP uptake after 1 h by K562 cells transduced with empty vector (control) or SLC19A1 expression vector (left) or with a non-targeting control shRNA (control) or *SLC19A1* shRNA (right). (**c**) Normalized [^{32}P]2′3′-cGAMP uptake in THP-1 (left) and K562 (right) cells after 1 h in DMSO or NHS–methotrexate (NHS–MTX, 5 μM)-treated. (**d**) Normalized [^{32}P]2′3′-cGAMP uptake after 1 h by THP-1 monocytes in the presence and absence of 100 μM competing, unlabelled CDNs (left) or 200 μM competing, unlabelled nucleotides (right). (**e**) Time course of [^{32}P]2′3′-cGAMP uptake in THP-1 monocytes in the presence and absence of 500 μM competing, unlabelled folates, antifolates or sulfasalazine. CPM, counts per minute. (**f**) Normalized [^{32}P]2′3′-cGAMP uptake after 3 h in human PBMCs from 6 healthy donors in the presence or absence of 500 μM competing, unlabelled folates, antifolates or sulfasalazine. (**g**) Coomassie staining and immunoblot (IB) analysis of pulldowns by 2′3′-cGAMP–Sepharose or control Sepharose of STING C-terminal domain (CTD) or hSLC19A1. (**h**) Western blot analysis of hSLC19A1 affinity purification (AP) with 2′3′-cGAMP–Sepharose in the absence or presence of free, unbound 2′3′-cGAMP, 5-me-THF or methotrexate (250 μM). In a–d, data are mean ± s.e.m. of $n = 3$ biological replicates. In e, data are mean ± s.d. of $n = 3$ technical replicates and representative of 3 independent experiments. In f, data are mean ± s.d. of $n = 6$ healthy donors over 2 independent experiments. g and h are representative of two independent experiments. Statistical analyses were performed using unpaired, two-tailed Student's *t*-tests (a–d), or one-way ANOVA followed by post hoc Tukey's test (f). ****$P \leq 0.0001$.

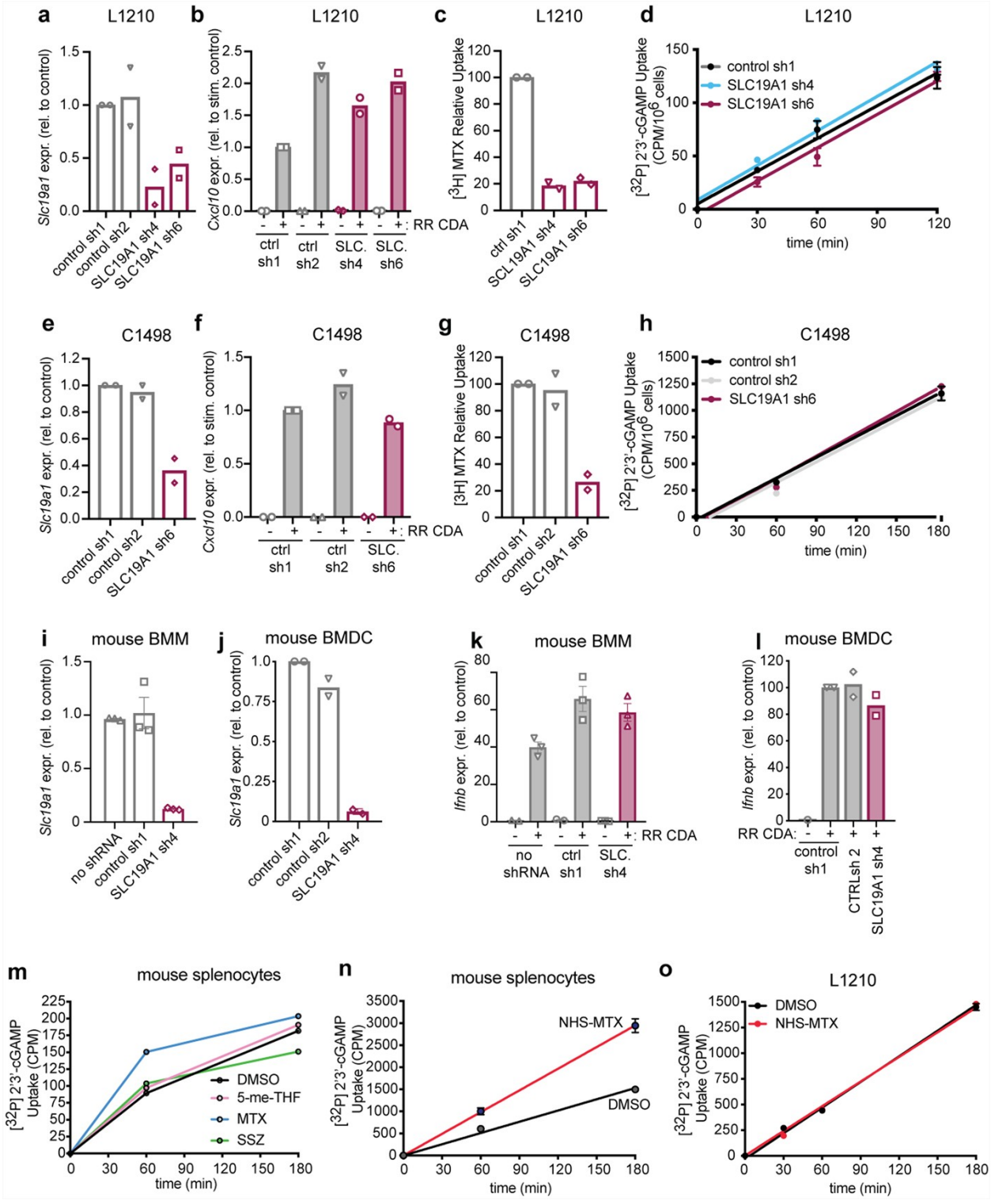

Figure 2.11: SLC19A1 expression or inhibition has no effect on CDN uptake and signaling in mouse cells.

(**a**) mRNA expression levels of *Slc19a1* in mouse L1210 cells expressing control shRNAs (sh1 and sh2) or *Slc19a1*-targeting shRNA (sh4 and sh6). (**b**) mRNA expression levels of *Cxcl10* in

L1210 cells described in a stimulated with 5 μg ml^{-1} 2′3′-RR CDA (RR CDA) for 5 h. (**c**) [^{3}H]-methotrexate uptake in L1210 cells described in a 1 h after exposure to [^{3}H]-methotrexate. (**d**) Time course of [^{32}P]2′3′-cGAMP uptake in L1210 cells described in a. (**e**) mRNA expression levels of *Slc19a1* in mouse C1498 cells expressing control shRNAs (sh1 and sh2) or *Slc19a1*-targeting shRNA (sh6). (**f**) mRNA expression levels of *Cxcl10* in the C1498 cells described in **e**, stimulated with 5 μg ml^{-1} 2′3′-RR CDA (CDN) for 5 h. (**g**) [^{3}H]-methotrexate uptake in C1498 cells described in **e** 1 h after exposure to [^{3}H]-methotrexate. (**h**) Time course of [^{32}P]2′3′-cGAMP uptake in C1498 cells transduced with a non-targeting control shRNA or *Slc19a1* shRNA. **i**, **j**, mRNA expression levels of *Slc19a1* in mouse BMMs (i) or BMDCs (j) not transduced or transduced with control shRNAs (sh1 and 2) or an shRNA targeting *Slc19a1*. (**k-l**) mRNA expression of the *Cxcl10* in cells described in i, j stimulated with 5 μg ml^{-1} 2′3′-RR CDA (CDN) for 5 h. (**m**) Time course of [^{32}P]2′3′-cGAMP uptake in primary mouse splenocytes in the presence and absence of 500 μM competing, unlabelled (anti-) folates and sulfasalazine. (**n**) Time course of [^{32}P]2′3′-cGAMP uptake in primary mouse splenocytes pretreated or not with NHS–methotrexate (5 μM). (**o**) Time course of [^{32}P]2′3′-cGAMP uptake in L1210 cells pretreated or not with NHS–methotrexate (5 μM). In a–c, e–g, j, l, data are mean of $n = 2$ biologically independent experiments. In d, h, i, k, n, o, data are mean ± s.d. of $n = 3$ technical replicates and are representative of 2 independent experiments. In m, data are mean of $n = 2$ technical replicates and are representative of 2 independent experiments. In time-course experiments (d, h, m–o), data are presented as counts per minute normalized to cell count.

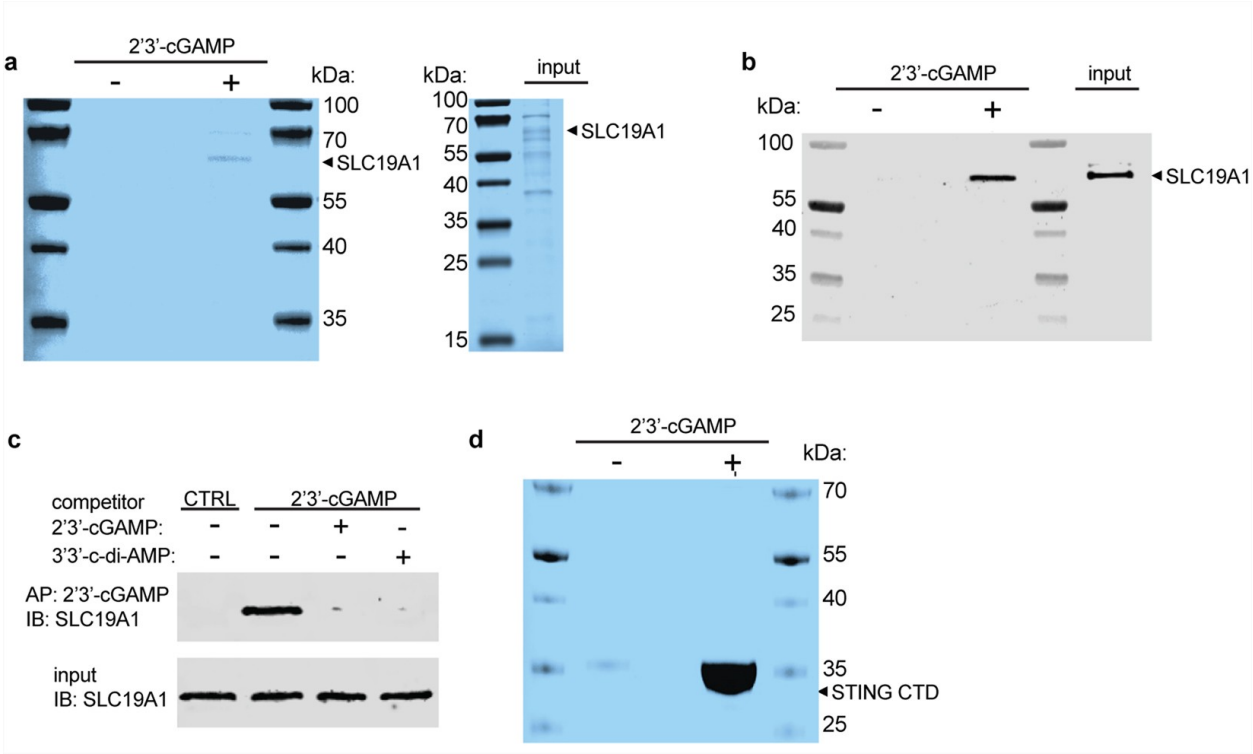

Figure 2.12: 2′3′-cGAMP binds to SLC19A1.
(**a**) Left, SDS–PAGE analysis followed by Coomassie blue staining of His-tagged human SLC19A1 (purified on Ni-NTA) pull-downs with Sepharose beads coupled with 2′3′-cGAMP (+) or control Sepharose beads (−). Input is shown on the right. (**b**) Western blots of the samples in a with SLC19A1 antibody. (**c**) Pull-downs of SLC19A1 competed with CDNs. His-tagged SLC19A1 was incubated with no CDN or with the indicated competing CDNs (250 µM) before pull-downs with 2′3′-cGAMP-Sepharose, followed by SDS–PAGE and western blotting with SLC19A1 antibody. A pulldown with control Sepharose is shown for comparison. (**d**) SDS–PAGE analysis followed by Coomassie blue staining of pull-downs of mSTING CTD with 2′3′-cGAMP (+) or control (−) Sepharose. In all panels, data are representative of two independent experiments with similar results.

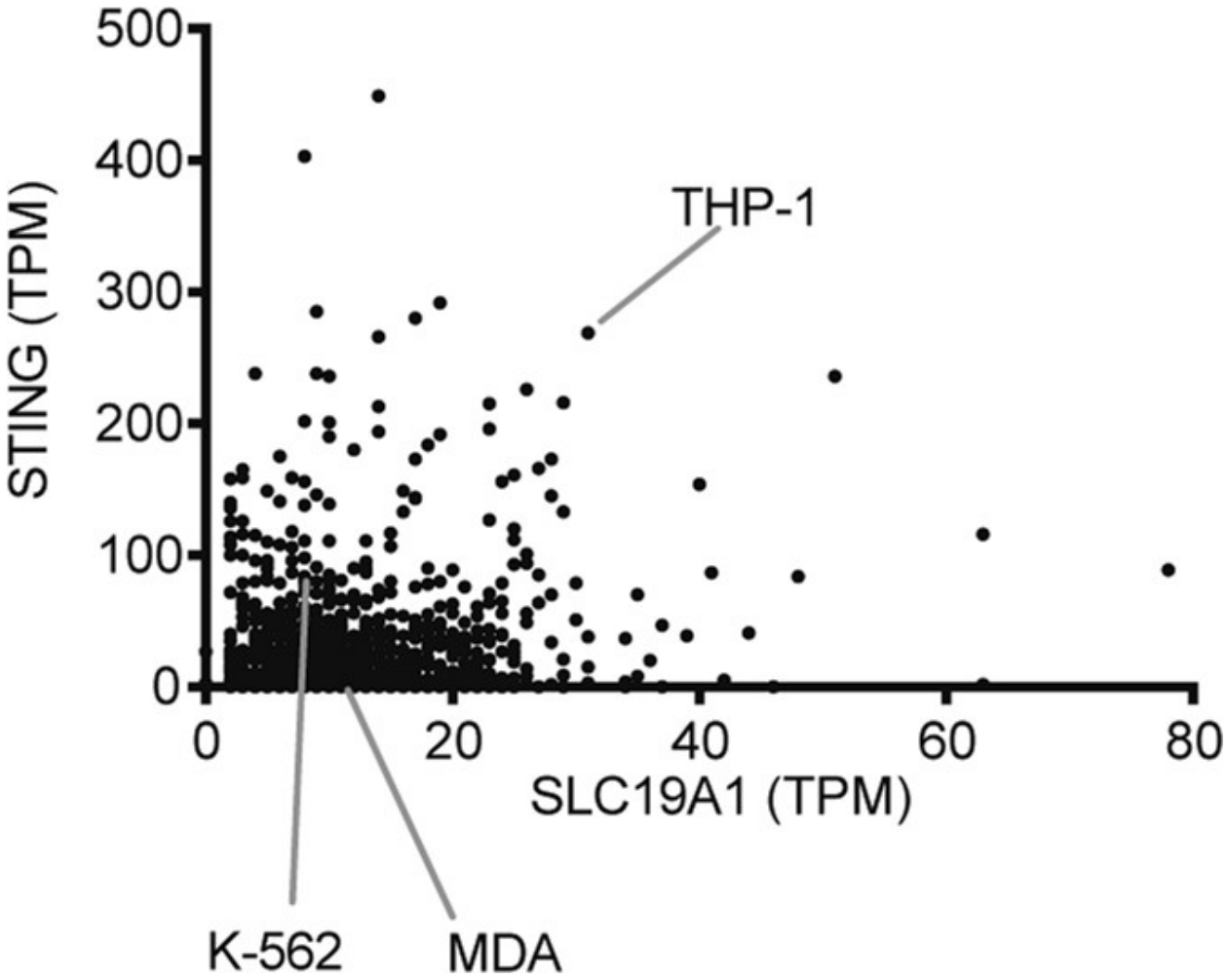

Figure 2.13: RNA sequencing data of *STING* and *SLC19A1* mRNA expression in 934 human cancer cell lines available at the Cancer Cell Line Encyclopedia website.
Expression is presented as transcripts per kilobase million (TPM). Data are downloaded from the European Bioinformatics Institute Gene expression Atlas (https://www.ebi.ac.uk/gxa/home). The dataset included three of the cell lines we examined, as shown.

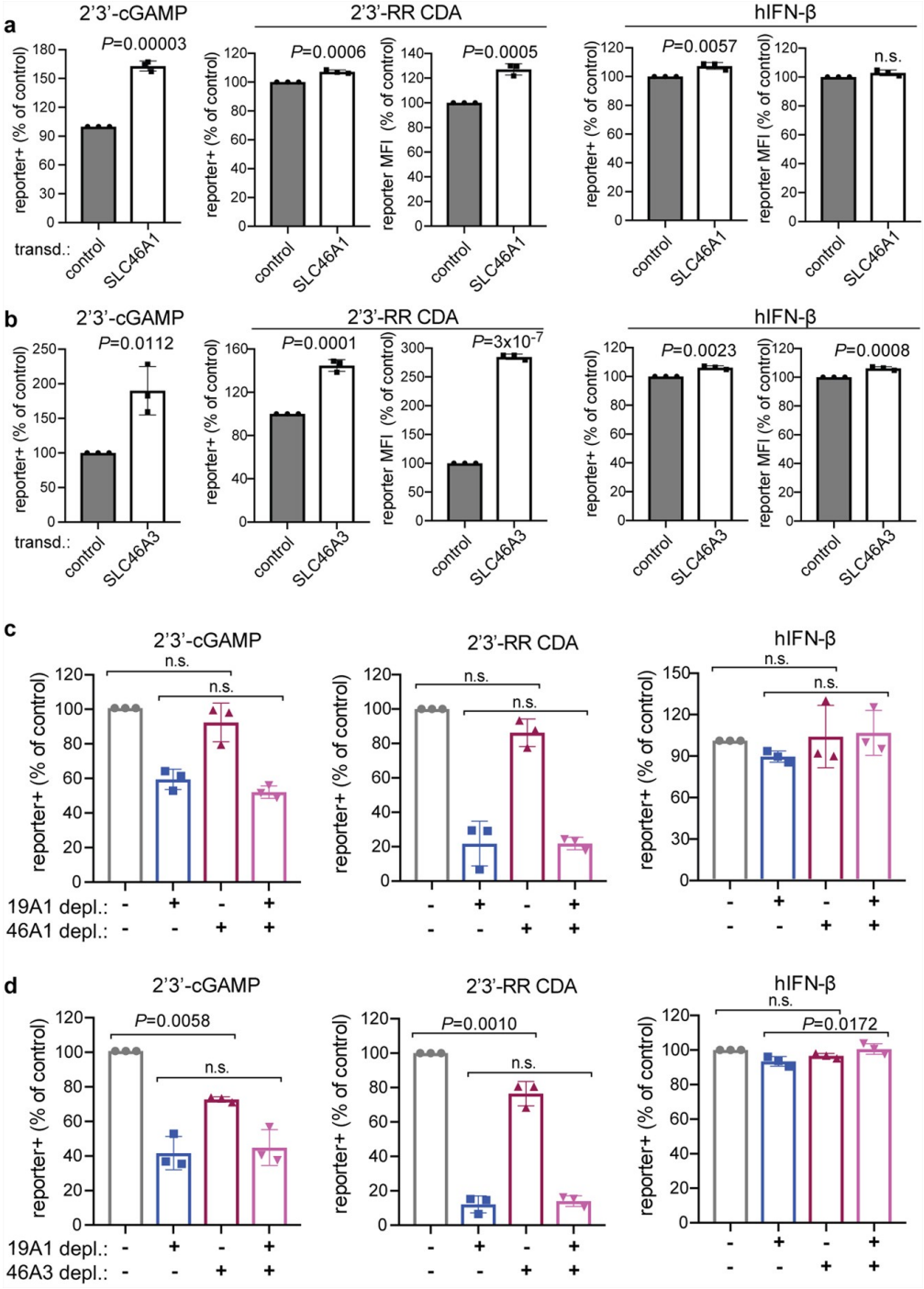

Figure 2.14: The effect of *SLC46A1* and *SLC46A3* expression on CDN-induced reporter activation.

(a-b) Enforced expression of *SLC46A1* and *SLC46A3* affects the responses of THP-1 cells to CDNs. Control THP-1 cells (transduced with empty expression vector) or *SLC46A1*-transduced THP-1 cells (a), or control THP-1 cells or *SLC46A3*-transduced cells (b) were stimulated with 2′3′-RR CDA (1.25 μg ml^{-1}), 2′3′-cGAMP (15 μg ml^{-1}) or IFN-β (100 ng ml^{-1}). tdTomato reporter expression was measured by flow cytometry 18–22 h after stimulation. **(c-d)** SLC46A1 or

SLC46A3 depletions had little or no effects on cellular responses to CDNs, and combining depletion of *SLC46A1* or *SLC46A3* with *SLC19A1* depletion had no additional effect compared to *SLC19A1* depletion alone. THP-1 cells were transduced with non-targeting control CRISPRi gRNAs or *SLC19A1*-targeting CRISPRi gRNA in combination with a second control CRISPRi gRNA or *SLC46A1*-targeting CRISPRi gRNA in (**c**) or *SLC46A3*-targeting gRNA in (d). Cells were stimulated with 2′3′-RR CDA (1.67 μg ml^{-1}), 2′3′-cGAMP (10 μg ml^{-1}) or IFN-β (100 ng ml^{-1}). tdTomato reporter expression was measured by flow cytometry 18–22 h after stimulation. Combined data of three independent experiments. Statistical analysis was performed using unpaired two-tailed Student's *t*-tests (a, b) or one-way ANOVA followed by post hoc Tukey's test when comparing only the effects of depleting SLC46A1 (c) or SLC46A3 (d). Data are mean ± s.e.m. of $n = 3$ independent replicates.

Table 2.1: Guide RNAs used in this study

guide RNAs (gRNA) used in this study			
Target gene	gRNA name	sequence (5'-3')	CRISPR system
hIRF3	IRF3-1	GGTCTGCACGGAGAGTGGAA	dCas9-BFP-KRAB
hIRF3	IRF3-2	GGGGTGGACTCCGTAGATGG	dCas9-BFP-KRAB
hSLC19A1	SCL19A1-1	GTACCTGCGACTCGGCGGGG	dCas9-BFP-KRAB
hSLC19A1	SLC19A2-2	GCGGTACCTGCGACTCGGCG	dCas9-BFP-KRAB
hSTING	STING-1	GGCTGCTCTGGATGATGACG	dCas9-BFP-KRAB
hSLC46A1	SLC46A1-1	GTACCGGGCCCCGGCACAGCA	dCas9-BFP-KRAB
hSLC46A3	SLC46A3-1	GGCCGCTGACCGACCGACGG	dCas9-BFP-KRAB
Control	Control	GGAGAGACGGTACCGTCTCA	dCas9-BFP-KRAB
GFP	GFP	GACCAGGATGGGCACCACCC	dCas9-BFP-KRAB
hSLC19A1	SLC19A1	TTCTTCAACCGCGACGACCG	Cas9
Control	Control	GGAGAGACGGTACCGTCTCA	Cas9

Table 2.2: RT-qPCR primers used in this study

RT-qPCR primers used in this study	
Primer	Sequence (5'-3')
hIRF3 fwd	AGAGGCTCGTGATGGTCAAG
hIRF3 rev	AGGTCCACAGTATTCTCCAGG
hSLC19A1 fwd	TGATCTCGTTCGTGACCTGCT
hSLC19A1 rev	GGCAGACACATTGTCATCAG
hSTING fwd	ACTGTGGGGTGCCTGATAAC
hSTING rev	TGGCAAACAAAGTCTGCAAG
hSLC46A1 fwd	ATGCAGCTTTCTGCTTTGGT
hSLC46A1 rev	GGAGCCACATAGAGCTGGAC
hSLC46A3 fwd	GCCATTCTCTGTTCTACGGTCC
hSLC46A3 rev	GTACCAAGCAACAGTGGCTGAG
hCCL5 fwd	CCTCGCTGTCATCCTCATTG

hCCL5 rev	TGCCACTGGTGTAGAAATACTC
hCXCL10 fwd	CCTTATCTTTCTGACTCTAAGTGGC
hCXCL10 rev	ACGTGGACAAAATTGGCTTG
hHPRT1 fwd	TGACACTGGCAAAACAATGCA
hHPRT1 rev	GGTCCTTTTCACCAGCAAGCT
hYWHAZ fwd	ACTTTTGGTACATTGTGGCTTCAA
hYWHAZ rev	CCGCCAGGACAAACCAGTAT
mUbc fwd	GCCCAGTGTTACCACCAAGA
mUbc rev	CCCATCACACCCAAGAACAA
mGAPDH fwd	TGTGTCCGTCGTGGATCTGA
mGAPDH rev	TTGCTGTTGAAGTCGCAGGAG
mSLC19A1 fwd	CCTGGTGTTCTATCTCTGCTTC
mSLC19A1 rev	TGATCTCGTTAGTCACCTGCT
mIFNB fwd	ATGAACTCCACCAGCAGACAG
mIFNB rev	ACCACCATCCAGGCGTAGC
mCCL5 fwd	AGATCTCTGCAGCTGCCCTCA
mCCL5 rev	GGAGCACTTGCTGCTGGTGTAG
mCXCL10 fwd	AGTGCTGCCGTCATTTTCTG
mCXCL10 rev	ATTCTCACTGGCCCGTCAT

Chapter 3

A STING-based biosensor affords broad cyclic dinucleotide detection within single living eukaryotic cells

The majority of this chapter was published in:

Pollock, A.J., Zaver, S.A. & Woodward, J.J. A STING-based biosensor affords broad cyclic dinucleotide detection within single living eukaryotic cells. *Nature Communications* **11**, 3533 (2020).

Summary

Cyclic dinucleotides (CDNs) are second messengers conserved across all three domains of life. Within eukaryotes they mediate protective roles in innate immunity against malignant, viral, and bacterial disease, and exert pathological effects in autoimmune disorders. Despite their ubiquitous role in diverse biological contexts, CDN detection methods are limited. In this chapter, using structure guided design of the murine STING CDN binding domain, we engineer a Förster resonance energy transfer (FRET) based biosensor deemed BioSTING. Recombinant BioSTING affords real-time detection of CDN synthase activity and inhibition. Expression of BioSTING in live human cells allows quantification of localized bacterial and eukaryotic CDN levels in single cells with low nanomolar sensitivity. These findings establish BioSTING as a powerful kinetic in vitro platform amenable to high throughput screens and as a broadly applicable cellular tool to interrogate the temporal and spatial dynamics of CDN signaling in a variety of infectious, malignant, and autoimmune contexts.

Introduction

The mammalian innate immune system provides a critical first line of defense against invading microorganisms through a suite of germline encoded, invariant sentinel proteins called Pattern Recognition Receptors (PRRs). PRRs survey the extracellular and intracellular milieu for molecular signatures of microbial origin, termed pathogen associated molecular patterns (PAMPs)[1,75]. Upon engaging PAMPs, PRRs participate in signal transduction cascades to activate antimicrobial gene regulatory programs that ultimately facilitate pathogen clearance[1,75]. Microbial nucleic acids, including DNA and RNA species, constitute a major class of PAMPs. Although a number of nucleic acid sensing PRRs have been identified to-date, the enzyme cyclic GMP-AMP Synthase (cGAS) has emerged as one of the most important sensors of foreign and self double-stranded (ds) DNA[4,5,63,75].

Upon allosteric activation by dsDNA, cGAS catalyzes the production of the cyclic dinucleotide (CDN) second messenger 2'3'-cyclic GMP-AMP (c[G(2',5')pA(3',5')p], 2'3'-cGAMP, or cGAMP), which then directly binds to and activates the ER-resident, scaffold protein STING[10–12,32,107]. In addition to 2'3'-cGAMP, STING also recognizes 3'3'-linked cyclic dipurines, including c-di-AMP, c-di-GMP, and 3'3'-cGAMP, produced in the context of infection with certain bacterial species, although with markedly reduced affinities[2,3,15,24]. CDN-mediated activation of STING facilitates the recruitment and activation of several kinases, culminating in transcription factor-mediated cytokine expression and induction of autophagy to sterilize the cytosol of the infected cell[22,23,33,34,39].

Despite significant advances in our understanding of cGAS and STING regulation, the development of methods for monitoring the kinetics and dynamics of CDN signaling, especially in living cells, is limited. Most studies have relied on type I interferon (IFN-I) induction downstream of STING activation as an indirect reporter of cGAS activity in cells[2,3,45]. While these assays are robust and sensitive, they are not specific as many PAMPs can elicit IFN-I responses. To that end, fluorescent tagged-STING constructs have been used as a more direct reporter for STING activation. These assays rely on the translocation of STING to a perinuclear punctate compartment upon CDN binding as a qualitative proxy for its activation and have recently been

employed to monitor 2'3'-cGAMP transfer via gap junctions[40]. These tools, however, are limited to a qualitative, binary localization readout. In lieu of these reporter assays, methods to directly measure cyclic dinucleotides, including mass spectrometry, enzyme immunoassays (EIA), ENPP1-based luciferase assays (cGAMP-luc), and RNA-based biosensors have been developed[3–5,10,108–111]. While these assays are specific, they range in their sensitivity and only provide bulk endpoint measurements following destruction of the biological sample.

FRET biosensors have been developed for the detection of small molecules, including the nucleotide second messengers cAMP[112,113] , cGMP[114], and cyclic-di-GMP[115–120]. Ligand binding to an intramolecular FRET biosensor results in a conformational shift that alters the relative distance and orientation of fused compatible donor and acceptor fluorophores. This, in turn, alters the excitation energy transfer between fluorophores, which can be quantitated by exciting the donor fluorophore and determining the ratio of acceptor fluorophore emission to donor fluorophore emission. This change in fluorescence is directly linked to ligand occupancy and thus reports on ligand concentration either in solution or within cells[121–123]. Because these biosensors are based on native ligand binding proteins, they are powerful, genetically encodable tools with biologically relevant binding affinities and responses. Use of these biosensors has provided fundamental insight into the spatial and temporal dynamics of nucleotide signaling, as well as the identification of activators and inhibitors following in vitro and cellular screens.

To address the limitations of current CDN detection techniques, we report the development of an intramolecular FRET biosensor deemed BioSTING, which is based on the eukaryotic CDN binding protein STING[124]. We demonstrate that recombinant BioSTING is a sensitive tool capable of detecting real-time CDN synthesis, drug inhibition, and extracted CDNs from cellular sources. Further, we show that BioSTING expressed in eukaryotic cells can be used to detect CDN synthesis, import, localization, and degradation by a viral protein. Thus, BioSTING affords a powerful in vitro and cellular platform for monitoring CDN levels and is likely to facilitate fundamental discoveries relating to CDN biology as well as translational drug discovery campaigns.

Results

Design and Development of BioSTING

CDN signal transduction is mediated by nucleotide binding to effector proteins. Ligand induced structural changes in the protein alter effector function to execute changes in response to altered cellular concentrations of the second messenger[7]. The mammalian protein STING is unique in its ability to bind a variety of CDNs of both mammalian and bacterial origin[2,3,10–12,15,24,32]. Structurally, STING is a multipass membrane protein with a C-terminal domain consisting of a dimerization region, a CDN binding domain, and a C-terminal tail (CTT) that is required for downstream signaling (Figure 3.1a)[22,23,33,34,39]. The CDN binding domain has been extensively characterized at atomic resolution. When the structures of human STING in the apo and c-di-GMP bound states are aligned, one monomer in each dimer was observed to overlap with nearly no change. However, the second monomer exhibited translocation of over 4 and 12 angstroms in the N and C-termini, respectively (Figures 3.1b and 3.2a, b). Because FRET is highly sensitive to the intermolecular distance between compatible fluorophores, we hypothesized that a fluorescent

fusion protein with the STING CTD would afford a platform for the development of a FRET-based CDN biosensor (Figure 3.1c)[7,14,125].

Unlike some human STING alleles, murine STING (mSTING) binds both bacterial and eukaryotic dipurine containing CDNs[2,3,10–12,15,24,32,107]. Therefore, to construct a reporter of broad utility, a prototype sensor was generated by fusing mSTING to the bright and photostable FRET pair mTFP and mKO2 at L152 and E335, respectively (Figure 3.1a)[121–123,126,127]. The residues contained within this region of mSTING include the dimerization domain and the CDN binding domain but exclude the amino-terminal transmembrane domains and CTT. Based on analysis of the crystal structure, we hypothesized that, upon cyclic dinucleotide binding, the C-terminus fused to mKO2 would shift in closer proximity to mTFP and increase the amount of FRET signal (Figure 3.1c). Indeed, we observed a modest ~7% FRET increase in the presence of cGAMP with purified recombinant protein (Figure 3.2c). While this observation demonstrated the utility of this approach, the FRET signal was deemed insufficient, and we sought to optimize this prototype to enhance the FRET signal. Notably, we did not observe a FRET change using the eCFP and eYFP FRET pair highlighting the importance of fluorophore orientation as a factor in generating a FRET response.

FRET is exquisitely sensitive to changes in distance and orientation. As such, a five amino acid GGSGG linker was added between mSTING-CTD and each fluorophore individually and in combination[128,129]. While addition of the linker between STING-CTD and mKO2 slightly diminished the FRET response, addition of GGSGG between mTFP and STING-CTD alone successfully increased the FRET change to over 20% (Figures 3.1d and 3.2c and Table 3.1). This modified FRET biosensor responded to 2'3'-cGAMP with a dynamic range of 12–125 nM and a limit of detection (signal-to-noise ratio 3:1) of approximately 12 nM (Table 3.1). Because a 20% FRET increase is more than sufficient for cellular applications, we named this protein BioSTING (Biosensor STING) and used this version in all further experiments.

Characterization of BioSTING-CDN Binding

Having generated BioSTING, we next sought to compare the biochemical parameters of nucleotide interactions between purified BioSTING and STING-CTD by DRaCALA analysis[130]. Radioactive cGAMP (Figure 3.2d) bound BioSTING and STING-CTD at a Kd of 56 and 61 nM, respectively (Figures 3.1e and 3.2e). Radioactive c-di-AMP (Figure 3.2d) bound BioSTING and STING-CTD at a Kd of 2.26 μM and 2.58 μM, respectively (Figures 3.1e and 3.2e). These results confirmed that the region of STING contained within BioSTING maintained CDN binding and that the addition of flanking FRET-fluorophores did not alter binding affinity or disrupt the dimer to which CDNs bind. To confirm that BioSTING retained binding specificity, we performed radioactive cGAMP binding analysis with both BioSTING and STING-CTD in the presence of a variety of unlabeled nucleotides. As expected, only 3'3'-cyclic and 2'3'-cyclic dinucleotides but not ATP, GTP, cAMP, or cGMP could compete off bound [^{32}P] 2'3'-cGAMP (Figures 3.1f and 3.2f). These findings reveal that fusion of the two FRET fluorophores to BioSTING has no discernable impact on nucleotide specificity or binding affinity relative to STING-CTD.

Finally, we monitored the dissociation kinetics by determining the rate that cold nucleotide could compete off bound radioactive nucleotide. Radioactive 2'3'-cGAMP was competed off BioSTING

and STING-CTD by cold 2'3'-cGAMP with a half-life of 121 and 83 min, respectively (Figure 3.1g). Radioactive 3'3'-c-di-AMP was competed off of both proteins with a half-life of <10 s by cold 3'3'-c-di-AMP (Figure 3.1h). Together, these results show similar dissociation rates of CDNs from BioSTING relative to STING-CTD, consistent with the similarity in the observed Kd's for these nucleotides. In addition, due to the rapid dissociation rate of 3'3'-c-di-AMP, BioSTING is anticipated to afford rapid monitoring of both increases and decreases in nucleotide levels of 3'3'-CDNs. However, as a consequence of the relatively slow dissociation rate of 2'3'-cGAMP, BioSTING may afford real time monitoring of increases in 2'3'-cGAMP but may be limited in the temporal resolution associated with its decline. Notably, these results suggest that STING activation by 2'3'-cGAMP may be possible through a single binding event while activation by 3'3'-CDNs may require constant exposure to an activating concentration of ligand.

BioSTING provides a real-time readout of cyclic dinucleotide production in vitro

Current in vitro methods for monitoring CDN production employ sensitive EIA, mass spectrometry, and cGAMP-luc endpoint measures, as well as less sensitive continuous tools, including a cGAMP RNA biosensor and an indirect pyrophosphate release assay[4,5,10,108–111]. Given the limitations of current CDN detection methods, the ease of recombinant BioSTING production, and its capacity to directly report on a variety of CDNs at biologically relevant concentrations, we employed BioSTING to monitor in vitro CDN synthase activity and inhibition to demonstrate its utility for kinetic characterization and feasibility for high throughput screening related to these enzymes.

To demonstrate the ability of recombinant BioSTING to detect real time production of cyclic dinucleotides, we monitored DNA integrity scanning protein A (DisA) mediated synthesis of 3'3'-c-di-AMP, which occurs constitutively in the presence of ATP. In reactions consisting of BioSTING, ATP, and increasing concentrations of purified DisA, we observed increasing rates of FRET signal concomitant with increasing DisA concentrations (Figure 3.3a). Next, cGAS synthesis of 2'3'-cGAMP from ATP and GTP was monitored. As expected, the rate of BioSTING FRET signal correlated with increased cGAS protein and there was no 2'3'-cGAMP production without the addition of DNA, which is required for allosteric activation of the enzyme (Figures 3.3b and 3.4a).

BioSTING FRET assays are carried out in a 96-well format using a fluorescent plate reader making it amenable to in vitro high throughput screening efforts (Figure 3.4b). Recently, Pfizer reported the development of the cGAS inhibitor PF-06928215[131]. To test the use of BioSTING as a platform to characterize small molecule inhibitors, we performed dose response measurements with fixed cGAS and variable concentrations of PF-06928215 (Figure 3.3c). In parallel, we also titrated cGAS levels while keeping the concentration of PF-06928215 fixed (Figure 3.4c). The slope of the linear region was determined for each reaction, plotted versus PF-06928215 concentration, and fit to identify an IC50 of ~12 μM (Figure 3.3d), in close agreement with the reported IC50 of 5 μM[131]. Together these studies demonstrate that BioSTING affords robust, continuous detection of CDN levels in vitro and offers flexibility in assay design, making it amenable to high throughput screens and kinetic characterization studies of a variety of CDN synthases. In addition to screening for modulators of CDN synthase activity, BioSTING could also potentially be used to screen directly for STING agonists and antagonists.

BioSTING can detect 2'3'-cGAMP extracted from mammalian cells

Given the ease of producing recombinant BioSTING and its nanomolar affinity for 2'3'-cGAMP, we anticipated that it may provide an attractive method for measuring 2'3'-cGAMP from cellular extracts. To demonstrate this utility, we monitored FRET responses of BioSTING exposed to methanol extracts from HEK293T cells transfected with increasing concentrations of pCDNA3.1-cGAS. As expected, FRET responses were negligible with low concentrations of transfected pCDNA3.1-cGAS plasmid but saturated at elevated plasmid concentrations (Figure 3.3e). Notably, at lower levels of transfected plasmid we observed marginal FRET responses. This is likely a consequence of the simultaneous increase in both cGAS expression and activating DNA, as well as the dilution factor chosen for the experiment. To overcome this limitation, samples containing low levels of cGAMP can be diluted less or subjected to a cGAMP enrichment step using recombinant STING.

In addition, we observed signal saturation with higher levels of transfected plasmid. To overcome signal saturation, samples transfected with the highest amount of pCDNA3.1-cGAS were diluted to obtain readings within the sensor's linear range (Figure 3.3f). Multiplying the dilution factor by the diluted sample's cGAMP concentration calculated by interpolation into a standard curve of known cGAMP concentrations (Figure 3.1d), thus allows for determination of cGAMP in the undiluted sample. If cell volume assumptions are applied, an average intracellular cGAMP concentration can be calculated, in our case ~30 μM, which was in line with the concentration determined by EIA and within the range of concentrations previously reported by other methods (Figure 3.4d)[44]. Together, these findings suggest that recombinant BioSTING can be used as a bulk cell extract 2'3'-cGAMP detection method; although, other sensitive methods for end-point 2'3'-cGAMP detection exist[44,108].

BioSTING can detect 2'3'-cGAMP within live mammalian cells

The ability to directly monitor cyclic dinucleotides in individual living eukaryotic cells is currently one of the biggest limitations in the field. Encouraged by the in vitro characterization of BioSTING, we next sought to extend its application within this context. BioSTING was introduced into a pSLIK doxycycline inducible lentiviral system to generate stable HEK293T cell lines (Figure 3.5a)[132]. Fixed levels of either pCDNA3.1-cGAS or empty vector were transfected into cells expressing BioSTING and FRET signal was monitored using flow cytometry. In cells expressing cGAS relative to an empty vector control, we observed a greater than 20% BioSTING FRET increase, consistent with our in vitro assays (Figure 3.5b, c, and 3.6a-c). We also confirmed production of 2'3'-cGAMP in this experimental system by EIA analysis (Figure 3.6b). To ensure that BioSTING FRET responses were directly due to cGAMP recognition, we delivered purified cGAMP using both lipofection and nucleofection. Lipofectamine transfection produced a strong response, which plateaued below the BioSTING saturation level, likely as a consequence of the limited carrying capacity of the transfection reagent (Figure 3.5d). Nucleofection, on the other hand, was not limited in this manner, and we observed complete BioSTING activation (Figure 3.6d).

As intracellular cGAMP concentrations can range from low nanomolar to high micromolar[44,108], to quantitatively contextualize the observed BioSTING FRET response in cells, we titrated the

levels of cGAS expression vector and determined the intracellular concentration of cGAMP by EIA in parallel with BioSTING FRET measurements by flow cytometry. Using assumptions about cell volume, we then plotted FRET changes versus average intracellular cGAMP concentration from which we were able to estimate that 50% of the maximum BioSTING FRET signal corresponds to a concentration of approximately 5–50 nM cGAMP in cells, consistent with the in vitro measured affinity of BioSTING for cGAMP and supporting our expectation that BioSTING is responding to biologically relevant concentrations of cGAMP (Figure 3.6e, f).

Reanalysis of our flow cytometry data to detect FRET levels of single cells rather than the entire population confirmed our expectation that, under the conditions tested, there was a unimodal rather than bimodal shift in signal (Figure 3.5e). Because the entire population is responding with a normal distribution, we interrogated the possibility of using BioSTING as a platform for screening via flow cytometry. To estimate sorting potential, a FRET high gate was drawn above cells transfected with an empty vector and a FRET low gate drawn below cells transfected with a high amount of pCDNA3.1-cGAS (Figure 3.5f). We obtained ~10-fold enrichment for cells in the FRET low gate (Figure 3.6g) and ~100 fold enrichment of cells in the FRET high gate (Figure 3.6h). We hypothesize that the decreased selection in the FRET low gate is a consequence of a small percentage of cells evading efficient transfection. Thus, efficiency of selection could likely be improved using an integrated inducible or constitutive cGAS system. Overall, these encouraging results provide support for utilizing BioSTING as a platform for forward genetic screens to identify genes involved in regulating cGAS and cGAMP in living cells.

In order to assess the impacts of BioSTING expression levels on intracellular FRET responses, we again reanalyzed our flow cytometry results to compare cells expressing high and low levels of BioSTING (Figure 3.7a). These two populations had similar FRET response dynamics but with slightly different response magnitudes (Figure 3.7b-d). Thus, although there is flexibility in the expression level of cells, BioSTING expression levels should be tightly controlled when comparing FRET responses between samples.

Development and use of a cGAMP-blind BioSTING

A powerful control for an intramolecular FRET biosensor is a ligand blind version which differentiates changes due to bonafide binding from other effects (i.e., protein–protein interactions, fluorophore quenching, etc). A literature search highlighted the mutations Y240S and T263A in human STING (Y239S and T262A in murine STING) as ideal candidates which would diminish CDN binding without disrupting protein stability (Figure 3.8a)[133]. As expected, Y239S T262A BioSTING stably expressed and neither appreciably bound radioactive cGAMP nor produced a FRET change in response to cGAMP (Figure 3.8b, c). To determine if Y239S T262A BioSTING could act as a cGAMP control in cells, we titrated pCDNA3.1-cGAS in cells expressing WT or mutant biosensor. While WT BioSTING produced a robust FRET response, Y239S T262A BioSTING only generated a minor FRET change at exceptionally high levels of cGAS, thus supporting the use of Y239S T262A BioSTING as a control biosensor for 2’3’-cGAMP (Figure 3.8d).

Bacterial 3’3’-CDNs have been shown to be released during infection and to activate STING in the cytosol. To determine if WT BioSTING and Y239S T262A BioSTING can detect bacterial

CDNs in cells, we titrated increasing concentrations of expression vectors for *B. subtilis* DisA which synthesizes c-di-AMP and a constitutively active isoform of *P. aeruginosa* WspR (D70E), denoted WspR*, which synthesizes c-di-GMP (Figure 3.8e)[14]. All nucleotides resulted in a BioSTING FRET increase. However, while Y239S T262A BioSTING produced a minor response to the highest concentrations of cGAS, moderate responses were observed for DisA, and unexpectedly large responses were observed for WspR*. Levels of c-di-AMP are not expected to reach high levels in physiologically relevant contexts, therefore Y239S T262A BioSTING is likely to serve as an adequate control for c-di-AMP. In contrast, the lowest levels of WspR* tested induced a large response in Y239S T262A BioSTING demonstrating that it will not be an adequate control for c-di-GMP. Thus, despite its applicability as a control for other CDNs, the Y239S T262A BioSTING variant may be selectively used as a c-di-GMP biosensor within cells.

We hypothesized that further design may be used to generate other versions of BioSTING which exhibit selectivity for CDNs based upon their unique chemical properties, including phosphodiester linkage and/or base content. Previous studies identified naturally occurring mutations in human STING that abolish responsiveness to 3'3'-CDNs while retaining 2'3'-cGAMP sensing[52]. In an effort to engineer a universally blind control biosensor we subsequently made the R231A/H mutations previously reported to diminish IFN-β activation in Y239S T262A BioSTING. We also introduced these mutations to WT BioSTING in an effort to make a sensor capable of uncoupling bacterial versus eukaryotic CDNs. When cyclic dinucleotide cyclases are expressed in this mutant array, we unexpectedly found that these mutants alone only diminished the response to cGAMP but the triple mutant Y239S, T262A, and R231A diminished but did not completely abrogate the FRET response to c-di-GMP (Figure 3.9). More work will be required to determine whether this is related to 3'3'-c-di-GMP binding before this sensor could be employed as a control for c-di-GMP secretion. Therefore, we were unsuccessful in our attempt to uncouple sensing of 3'3'-CDNs from 2'3'-cGAMP. In future iterations of BioSTING, we hope to use unbiased approaches to make BioSTING variants with altered nucleotide specificities.

BioSTING exhibits broad utility for monitoring 2'3'-cGAMP dynamics in live cells

Based on our encouraging results highlighting BioSTING's ability to detect cGAMP in cells, we next sought to demonstrate BioSTING's utility to monitor modulation of cGAS activity. Previous experiments titrated pCDNA3.1-cGAS alone, resulting in simultaneous increases in both the CDN cyclase and stimulatory ligand, leading to titration curves with positive Hill coefficients. To directly measure cGAS activation we co-transfected cells with a fixed, low concentration of pCDNA3.1-cGAS and increasing amounts of calf thymus DNA (CT-DNA) ligand. As expected, at low CT-DNA levels we observed no detectable FRET increase, but as CT-DNA content was increased, we observed an elevated FRET signal that began to saturate at the highest concentration of stimulatory ligand tested (Figure 3.10a). These results suggest that BioSTING is a useful tool to investigate the kinetics of cGAS activation in live cells.

The cGAS-STING pathway is immensely important for controlling viral infection and many viruses have developed methods to inhibit this pathway. Recently, vaccinia virus was reported to antagonize cGAS-STING signaling through expression of Poxin, a 2'3'-cGAMP-selective

phosphodiesterase[52]. To monitor cGAMP hydrolysis by Poxin in cells, we expressed a constant level of wild-type (WT) or catalytically dead (H17A) Poxin over a titration of cGAS plasmid. Expression of Poxin in 293T cells was confirmed by [^{32}P] CDN hydrolysis assays (Figure 3.11a, b). In cells transfected with low levels of cGAS plasmid we observed high FRET from the H17A mutant and a greatly decreased FRET response in cells expressing the WT Poxin. As expected, expression of high cGAS levels overcame the capacity of Poxin to antagonize cGAMP levels (Figure 3.10b). Co-expression of Poxin with DisA or WspR* had no effect on 3'3'-CDN-mediated FRET responses as compared to empty vector controls, consistent with the role of Poxin as a 2'3'-cGAMP specific hydrolase (Figure 3.11c). These results demonstrate the utility of BioSTING to characterize modulators of cGAMP concentrations within living cells.

While cGAS production of cGAMP and subsequent STING activation both occur in the cytosol, recent findings have established that CDNs can be transmitted between cells through export and import mechanisms, as well as through gap junctions[40,44–49,51]. Such nucleotide transfer is reported to facilitate antitumor properties and cGAMP is being explored therapeutically both alone and in combination with PD-1 blockade[43,44,46,51,54,60]. The therapeutic utility of cGAMP in this context requires nucleotide import to the cytosol to promote STING inflammatory responses[43–46]. To investigate the utility of BioSTING for monitoring cellular import of cGAMP, we added increasing concentrations of cGAMP to the extracellular medium. After 6 h, cellular FRET signals in response to altered concentrations of cGAMP exhibited saturation like responses below the maximum signal associated with the sensor (Figure 3.10c). The observed saturation of the response may be due to saturation of the importer operative in these cells or a consequence of the establishment of import-export equilibrium. While a thorough account of the transport mechanisms is yet to be documented, these results demonstrate that BioSTING can detect cGAMP uptake from the extracellular space and may provide a valuable tool to identify and characterize the mechanism by which cGAMP is transferred among cells.

Despite being a well-studied system, conflicting reports regarding cGAS and cGAMP localization remain[41,64,65,67,68]. As a genetically encodable protein, we hypothesized that BioSTING could be localized to distinct cellular compartments through the introduction of specific signal sequences. As such, we introduced a nuclear localization signal (NLS) to BioSTING, which resulted in successful localization to the nucleus (Figures 3.10d, e and 3.11d, e). Using a cGAS titration, we were able to detect cGAMP in both the nucleus and the cytoplasm (Figure 3.10f). Consistently, the Y239S T262A BioSTING control sensor had very little change in FRET response providing additional evidence that we are detecting bonafide cGAMP in the nuclear compartment. Although these experiments only indicate that cGAMP can penetrate the nucleus, we anticipate that utilization of BioSTING in time-course and microscopy experiments will further elucidate the localization of cGAMP production under various activating conditions and may be used to reveal mediators of nucleotide transit between cellular compartments.

Finally, BioSTING, containing the dimerization domain of full-length STING, has the potential to heterodimerize with endogenous STING. To determine the consequences of heterodimerization, full-length, human STING was expressed alone or in combination with cGAS in HEK293T cells stably expressing BioSTING. Expression of human STING in this context decreased the response of BioSTING in the presence and absence of cGAS (Figure 3.10g). Observation of a FRET decrease upon expression of STING suggests that heterodimerization leads to an altered

conformation and that cells must be deficient for STING in order to attain interpretable FRET responses. Taken together, these data demonstrate that our first-generation FRET biosensor, BioSTING, is highly versatile for both in vitro and cellular studies, but its application is currently limited to a STING-deficient setting.

Concluding Remarks

Here, we report the development of BioSTING, a FRET-based intramolecular biosensor engineered to monitor CDNs in vitro and in cells. BioSTING maintains the native CDN binding properties of the parent protein upon which it was designed and as such exhibits CDN reporting capacity in physiological concentration ranges. Through a variety of in vitro and cellular studies we establish BioSTING as a robust sensor of a variety of CDNs, providing real-time detection of nucleotide levels with temporal and spatial resolution.

BioSTING's ease of recombinant production, native binding properties, and simple kinetic readout make it a promising tool for investigating cyclic dinucleotides in vitro. We show that BioSTING can detect extracted nucleotides from cellular samples, as well as enzymatic production of cyclic dinucleotides with recombinant protein. Although not investigated in this work, BioSTING can also likely be used to monitor phosphodiesterase activity for bacterial 3'3'-cyclic dinucleotides in real time. However, given the unexpectedly low dissociation rate, such application for 2'3-cGAMP hydrolysis may be limited. In addition to general enzymatic characterization of CDN synthesis, we also utilized BioSTING to characterize PF-06928215 inhibition of cGAS, demonstrating its robust utility for characterization of small molecule modulators of CDN synthases. A key limitation to be considered relates to the spectral properties of compounds under investigation. For instance, while several antimalarial compounds have been reported to inhibit cGAS activity, the intrinsic fluorescence of these compounds spectrally overlap with BioSTING and interfere with its application in this context.

Despite impressive in vitro utility, the primary motivation for developing BioSTING was to create a tool capable of detecting 2'3'-cGAMP in live single cells. While the dynamic range of BioSTING is indeed narrower, our findings support that BioSTING binds and responds to cGAMP at physiologically relevant concentrations and with sensitivity comparable to commercially available EIA based approaches. In addition, we successfully measured FRET changes by flow cytometry, providing the first single cell measurements of CDN levels. In addition to single cell measurements, a key aspect of FRET based biosensors is the capacity to provide subcellular information about signaling dynamics. As a genetically encodable protein, localization tags can be added to target a sensor to specific cellular compartments. There is currently a debate about the localization of cGAS and therefore production of cGAMP in cells. By introducing an NLS to BioSTING we demonstrated the ability to restrict the sensor to the nucleus and monitor cGAMP within this compartment. Application of BioSTING in combination with rapid imaging microscopy is likely to provide important insight into when and where cGAMP is produced and if this differs depending upon the infectious insult, within distinct cell types, or in response to cellular damage versus pathogen encounter.

One particularly exciting application of BioSTING is for high throughput small molecule and forward genetic screening. In high throughput small molecule screening applications, BioSTING

provides the ability to measure cGAMP production in live cells, which can simultaneously account for compound toxicity and cell permeability together with target engagement. In fact, Pfizer identified PF-06928215 as an inhibitor of cGAS through in vitro enzyme screening methods but the compound failed in development as a pharmaceutical due to its inability to access the cytosol. In addition, we anticipate that BioSTING will have utility in genetic screens to study modulation of cGAMP levels in cells. Because FRET measurements can be conducted using flow cytometry, BioSTING affords the ability to conduct these studies in batch culture. Combining BioSTING flow-based sorting with disruption or overexpression libraries from mammalian and microbial pathogens will afford genome wide interrogation of CDN signaling pathways, including molecular insight into pathogen associated antagonists, as well as cell intrinsic regulators of the pathway, namely cGAS activators and inhibitors and mediators of cGAMP hydrolysis, transport, and localization.

Though developed to investigate 2'3'-cGAMP cellular biology, BioSTING is also capable of investigating similar aspects of bacterial 3'3'-cyclic dinucleotides. We demonstrated through expression of DisA and WspR* that BioSTING can detect bacterial 3'3'-CDNs in the mammalian cytosol. Thus, the potential for BioSTING to be used as a tool to investigate the timing and magnitude of bacterial CDN release in biologically relevant contexts such as during *Listeria monocytogenes, Mycobacterium tuberculosis,* and *Chlamydia trachomatis* infection, among others, is evident. In our attempts to identify CDN blind variants of BioSTING, we inadvertently identified Y239S T262A BioSTING as a c-di-GMP specific reporter. These findings suggest that with further engineering of BioSTING it may be possible to identify mutants sensitive to specific CDNs. Such sensors would be useful to dissect mixed CDN interactions such as during *M. tuberculosis* infection, in which both cGAS produced 2'3'-cGAMP and bacterial derived c-di-AMP have been implicated in STING activation[103,134,135]. In addition, a wide array of bacterial cyclic dinucleotides of dipurine, dipyrimidine, and mixed purine pyrimidine content were recently reported; however, only cyclic dipurine containing nucleotides were shown to robustly bind to and activate STING[9,15]. It is feasible that BioSTING can be engineered through a mix of semi-randomized and rationally designed mutations to detect these more recently discovered signaling nucleotides. Finally, mutation of Tyrosine 167, which stabilizes CDN binding though a pi-stacking interaction, to an Alanine or Valine will likely generate an additional BioSTING control variant that is universally blind to all CDNs. Although outside the scope of this work, the intracellular concentration of bacterial CDNs have been reported to be similar to the Kd of BioSTING[3,103,118], thus it is feasible that expression of BioSTING in bacterial cells will afford interrogation of CDN dynamics within these organisms as well.

BioSTING is a blue, orange-based rather than far-red or luminescence-based biosensor, which limits its use to cell culture due to the limited ability for blue-orange light to penetrate tissues. Although there are many important findings to be made in cell culture, as a clinically relevant molecule, there is also an immense interest in studying 2'3'-cGAMP in vivo. We believe that it will be possible to develop a far-red FRET or luminescent version of BioSTING by replacing mKO2-mTFP fluorophores with a small circularly rotated library of a red-shifted FRET pair, BRET pair, or split luciferase and screening for increased signal upon cGAMP binding[136–140]. Production of either a far-red or luminescent derivative integrated into the murine genome under either constitutive or cell specific promoters will allow for the detection of cGAMP in vivo and

create a powerful model to study cGAMP activity in viral infection and autoimmune disease models.

As a STING-based biosensor, BioSTING is sensitive to heterodimerization with native STING. Thus, the sensitivity afforded by STING also leads to the limitation that BioSTING must be used in cells which either do not express or are genetically modified to lack STING. Although many important studies are tractable in this system, some investigations such as those coupling cGAMP measurements with STING-Interferon pathway activation or regulation in the same sample currently are not. To allow investigation of these exciting research areas we anticipate creating a version of BioSTING incapable of heterodimerization with WT STING through engineering of the dimerization interface. This updated version will increase BioSTING's versatility while retaining the impressive sensitivity and specificity of STING.

Overall BioSTING is a powerful tool that makes many fundamental and clinically important investigations of cyclic dinucleotide biology more tractable and in some instances even feasible. In addition to the immediate application of current BioSTING versions, we believe there is immense promise in using BioSTING as a foundation to develop a wide array of biosensors with unique CDN binding or in vivo imaging capacities. In total, BioSTING represents a versatile tool to significantly advance the current limits of knowledge related to the ever expanding and clinically relevant field of cyclic dinucleotide signaling.

Materials and Methods

BioSTING cloning

Primers for BioSTING cloning are listed in Supplementary Table 2 and plasmids and strains are listed in Supplementary Table 3. Prototype and GGSGG linker versions of BioSTING were generated by amplifying STING CTD with Kapa HiFi polymerase (Kapa Biosystems) using a combination of primers 1, 2, 3, and 4 from pET28b-mSTING CTD. The resulting products were ligated into pET15b-mKO2-12AA-mTFP using Spe1/Kpn1 fast digest restriction endonuclease cloning (Thermo Fisher) and transformed into XL1-Blue chemically competent *E. coli*. Site directed mutagenesis was carried out by amplifying the generated pET15b-BioSTING sensor using primers 5, 6 or 7, 8 or 9, 10, or 11,12 using Kapa HiFi polymerase. PCR purified product was DpnI digested (NEB) and transformed into XL1-Blue chemically competent *E. coli*. To generate pSLIK-BioSTING, pET15b-BioSTING was amplified using primers 13 and 14 for cytoplasmic expression and primers 13 and 15 to add a nuclear localization signal (NLS) from c-MYC at the C-terminus. These products were then ligated into the BsiW1 (Thermo Fisher) site of pSLIK using InFusion (Takara) then transformed into Stbl3-OneShot competent cells (Thermo Fisher).

Protein expression and purification

Recombinant 6×-His tagged SUMO-mcGAS, *B. subtilis* (*B.s.*) DisA, mSTING-CTD, and mRECON were expressed and purified as summarized below[45]. Briefly, plasmids for mcGAS, DisA, mSTING-CTD, and mRECON expression were transformed into Rosetta (DE3)pLysS chemically competent cells. Overnight cultures of the resulting transformed bacteria were inoculated into 1.5 L of LB broth at a 1:100 dilution. Bacterial cultures were grown to OD_{600} 0.4–0.6 at 37 °C after which protein expression was induced by the addition of 0.5 mM isopropyl β-D-1-thiogalactopyranoside (IPTG) for 20 h at 16 °C. Bacteria were harvested by centrifugation, and the cell pellets were resuspended in Buffer A [50 mM Tris-Cl pH = 8.0, 300 mM NaCl, 20 mM Imidazole, 5 mM β-Mercaptoethanol (BME), and 1 mM phenylmethylsulfonyl fluoride (PMSF)]. Cells were lysed by sonication and clarified lysate was bound to HisPur NiNTA Resin (Thermo Scientific). The resin was washed with 100–200 column volumes of buffer A and bound proteins were eluted in Buffer B [50 mM Tris-Cl pH = 7.4, 300 mM NaCl, 300 mM Imidazole, 5 mM β-Mercaptoethanol (BME), and 1 mM phenylmethylsulfonyl fluoride (PMSF)]. Following NiNTA chromatography, His6-SUMO-mcGAS was exchanged into Buffer C [20 mM Tris-Cl pH 7.4, 250 mM NaCl, 1 mM dithiothreitol (DTT)] and further purified by Heparin Sepharose chromatography. Bound cGAS was eluted over 250 mM to 1000 mM NaCl gradient. The resulting purified proteins were analyzed by SDS-PAGE, exchanged into storage buffer [40 mM Tris pH 7.5, 100 mM NaCl, 20 mM $MgCl_2$] using PD-10 desalting columns (GE Healthcare), snap frozen, and stored at −80 °C until use.

For BioSTING expression, plasmids encoding BioSTING variants were transformed into Rosetta (DE3)pLysS chemically competent cells.Overnight cultures of the resulting transformed bacteria were inoculated into 1 L of LB broth and grown as above. At an OD_{600} of 0.5–0.7, protein expression was induced by the addition of 0.2 mM isopropyl β-D-1-thiogalactopyranoside (IPTG) for 6 h at 18 °C. Bacteria were harvested by centrifugation, and the cell pellets were resuspended in Buffer D [50 mM Tris-Cl pH = 7.5, 100 mM NaCl, 20 mM Imidazole, 5 mM β-Mercaptoethanol

(BME), and 1 mM phenylmethylsulfonyl fluoride (PMSF)]. Cells were lysed by sonication and clarified lysate was bound to HisPur NiNTA Resin (Thermo Scientific, Waltham, MA). The resin was washed with 100–200 column volumes of Buffer D and bound proteins were eluted in Buffer E [50 mM Tris-Cl pH = 7.5, 100 mM NaCl, 300 mM Imidazole, 5 mM β-Mercaptoethanol (BME), and 1 mM phenylmethylsulfonyl fluoride (PMSF)]. The resulting proteins were concentrated and further purified by gel filtration on a Superdex 200 column (GE Healthcare) using storage buffer [40 mM Tris pH 7.5, 100 mM NaCl, 30 mM $MgCl_2$, supplemented with 0.5 mM TCEP]. Protein samples were tested for purity by SDS-PAGE followed by Coomassie Brilliant Blue staining. Fractions with high purity were pooled, concentrated, flash frozen, and stored at −80 °C until use in biochemical assays.

Synthesis of [^{32}P] 2'3'-cyclic GMP-AMP and [^{32}P] 3'3'-cyclic di-AMP

[^{32}P] Radiolabeled cyclic dinucleotides (CDNs) were synthesized enzymatically using α-[^{32}P] ATP (Perkin-Elmer) and recombinant SUMO-mcGAS (2'3'-cGAMP) or *B.s*. DisA (3'3'-c-di-AMP) and affinity purified using mSTING-CTD and mRECON, as follows: [^{32}P] cGAMP was synthesized enzymatically by incubating 0.33 μM α-[^{32}P] ATP (Perkin-Elmer) with 250 μM unlabeled GTP, 1 μg of Interferon Stimulatory DNA 100mer, and 1 μM of recombinant His-tagged cGAS in binding buffer [40 mM Tris pH 7.5, 100 mM NaCl, 20 mM $MgCl_2$] at 37 °C overnight. Subsequently, recombinant cGAS was removed from the reaction mixture by incubation with HisPur Ni-NTA resin (Thermo Scientific) for 30 min. The sample was transferred to a minispin column (Thermo Scientific) to elute the crude [^{32}P] cGAMP sample. The resulting [^{32}P] cGAMP was purified further using recombinant mSTING-CTD. 100 μM mSTING-CTD was bound to HisPur Ni-NTA resin for 30 min on ice. The resin was washed two times to remove unbound mSTING-CTD. The resulting resin was incubated with the remaining crude cGAMP synthesis reaction mixture for 30 min on ice. Following removal of the supernatant, the Ni-NTA resin was washed five times with ice cold binding buffer. The resin was then incubated with 100 μL of binding buffer for 10 min at 95 °C and transferred to a minispin column to elute [^{32}P] cGAMP.

[^{32}P] c-di-AMP was synthesized as follows: briefly, 1 μM α-[^{32}P] ATP (Perkin-Elmer) was incubated with 1 μM of recombinant DisA in binding buffer at 37 °C overnight. The reaction mixture was boiled for 5 min at 95 °C and DisA was removed by incubation with HisPur Ni-NTA resin. The sample was transferred to a minispin column (Thermo Scientific) to elute the crude [^{32}P] c-di-AMP sample. The resulting [^{32}P] c-di-AMP was further purified using recombinant His-tagged mRECON. 100 μM His-tagged mRECON was bound to HisPur Ni-NTA resin for 30 min on ice. The resin was washed two times to remove unbound RECON. The resulting resin was incubated with the remaining crude [^{32}P] c-di-AMP sample for 30 min on ice. Following removal of the supernatant, the Ni-NTA resin was washed five times with ice cold binding buffer and then incubated with 100 μL of binding buffer for 5 min at 95 °C. The slurry was then transferred to a minispin column to elute [^{32}P] c-di-AMP.

Affinity purified CDNs were analyzed by Thin Layer Chromatography (TLC) on Polygram CEL300 PEI TLC plates (Machery-Nagel) in buffer containing 1:1.5 (vol/vol) saturated $(NH_4)_2SO_4$ and 1.5 M NaH_2PO_4 pH 3.6. [^{32}P] radiolabeled CDNs were visualized by exposure onto PhosphorImager screens, which were developed using a Typhoon FLA 9000 biomolecular imager (GE Healthcare) and determined to be ~99% pure.

Nucleotide binding assays

[^{32}P] Radiolabeled cyclic dinucleotide binding assays were performed using DRaCALA[105]. Binding assays were performed in binding buffer [40 mM Tris pH 7.5, 100 mM NaCl, 20 mM $MgCl_2$] at room temperature. To determine binding affinities, two-fold serial dilutions of proteins were incubated with ~1 nM of [^{32}P] radiolabeled CDNs for at least 10 min. To determine binding specificities, proteins were pre-incubated with 500 μM excess, unlabeled nucleotides for 10 min, followed by incubation with ~1 nM of [^{32}P] radiolabeled CDNs for at least 10 min. Samples were then blotted onto nitrocellulose membranes and allowed to air dry. [^{32}P] radioactivity was visualized by exposure onto PhosphorImager screens, which were developed using a Typhoon FLA 9000 biomolecular imager (GE Healthcare). Non-radioactive 2'3'-cGAMP (Invivogen), 3'3'-cGAMP (Invivogen), 3'3'-c-di-AMP (Invivogen, San Diego, CA), and 3'3'-c-di-GMP (BIOLOG Life Science Institute, Bremen, Germany) were purchased and diluted in endotoxin free water.

In vitro FRET assays

5–10 μM purified BioSTING proteins were incubated with increasing concentrations of cyclic dinucleotides within a black flat bottom opaque 96-well plate (Greiner Bio-One) in activity buffer [40 mM Tris pH 7.5, 100 mM NaCl, 20 mM $MgCl_2$]. mTFP and FRET fluorescence was monitored using a fluorimeter (BioTek Synergy H1 Hybrid Reader, BioTek Instruments) with the following parameters (unless otherwise stated): 458 nm excitation, 490 nm emission for mTFP, and 600 nm emission for mKO2. Assay parameters were calculated using Prism Software. Kd and EC50 were determined using nonlinear fit and all other parameters were calculated using linear fit, according to literature precedent [26].
Enzyme activity assays

For DisA enzyme activity assays, 5–10 μM purified BioSTING was incubated with increasing concentrations of recombinant *B.s*. DisA within a black 96-well plate in activity buffer [40 mM Tris pH 7.5, 100 mM NaCl, 20 mM $MgCl_2$]. Enzyme assays were initiated by the addition of 1 mM ATP, and the enzyme reactions were allowed to proceed for 2 h at 37 °C.

For cGAS enzyme activity assays, 5–10 μM purified BioSTING was incubated with increasing concentrations of recombinant SUMO-mcGAS within a black 96-well plate in activity buffer [40 mM Tris pH 7.5, 100 mM NaCl, 20 mM $MgCl_2$]. Enzyme assays were initiated by the addition of 1 mM ATP, 1 mM GTP and 1 μg ISD (Figures 3.3b and 3.4a, b) or by the addition of 250 μM ATP, 250 μM GTP, and 50 ng ISD (Figures 3.3c, d and 3.4c). Enzyme assays were allowed to proceed for 2 h at 37 °C. cGAS inhibitor (PF-06928215) was purchased from Sigma-Aldrich and diluted in sterile DMSO.

For all assays, FRET activity was monitored as above.

2'3'-cGAMP extraction

HEK293T cells were plated at a density of 750,000 cells per well of a 6-well cell culture plate. The next day cells were transfected with the indicated amounts of pcDNA3.1-hcGAS vector using PEI transfection reagent (Polysciences). Twenty-four hours later the cells were harvested by centrifugation and washed once with ice-cold PBS. Cell pellets were resuspended in ice-cold 80% Optima, HPLC grade methanol (Fisher Scientific) and incubated on ice for 20 min. Cells were further lysed by sonication. Following centrifugation, cellular extracts were completely dried under vacuum and stored at −20 °C until use. For FRET assays, extracts were resuspended in activity buffer [40 mM Tris pH 7.5, 100 mM NaCl, 20 mM $MgCl_2$] containing 5–10 μM purified BioSTING and transferred to a black 96-well plate. FRET activity was monitored using a fluorimeter as described above. Quantification requires a standard curve of known cGAMP concentrations in the sample buffer done at the time of analysis.

Cell lines

Human Embryonic Kidney (HEK) 293 T cells were grown in Dulbecco's Modified Eagle Medium (DMEM) (Gibco) supplemented with 10% (v/v) heat-inactivated FBS (HyClone), 1 mM sodium pyruvate, 2 mM L-Glutamine (Thermo Fisher), 100 U mL^{-1} penicillin, 100 μg mL^{-1} streptomycin and maintained at 37 °C in 5% CO2 in a humidified incubator.

Lentivirus production and transduction

VSV-G pseudotyped, self-inactivating lentivirus was prepared by transfecting a semi-confluent 10 cm dish of HEK293T cells with 4 μg of psPAX2, 2 μg of pCMV-VSV-G, together with 4 μg of pSLIK lentiviral vector using Poly(ethyleneimine) (PEI). Growth medium was replaced 24 h after transfection and cell culture supernatants were collected at 48 and 72 h after transfection and filtered through a 0.45 μm filter.

For lentiviral transduction, HEK293T cells were seeded at a density of 2 to 4 million cells per 10 cm dish. The following day, cells were transduced with 5 mL of filtered lentiviral supernatant. 24 h later the cell culture medium was removed and replaced with standard cell culture medium supplemented with 2 μg per mL puromycin (Gibco). For all subsequent experiments, lentivirus-transduced cells were passaged and maintained in selection medium containing puromycin.

Intracellular FRET assays

For experiments using CDN cyclases, HEK293T cells stably expressing the indicated BioSTING constructs under a doxycycline-inducible promoter were plated at a density of 750,000 cells per well of a 6-well cell culture plate. The next day, the cells were transfected with the indicated amounts of cyclase-encoding plasmids using PEI transfection reagent. One hour later, biosensor expression was induced by the addition of Doxycycline Hydrochloride (1 μg mL^{-1}) (Sigma-Aldrich). Twenty four hours later the cells were harvested by centrifugation and resuspended in ice-cold PBS. Biosensor activity was determined by FACS analysis. To contextualize results, a negative control in which no cGAMP is present and a positive control where cGAMP is abundant should be run in each assay to quantify the lower and upper bounds of FRET activation.

For electroporation experiments, HEK293T cells stably expressing wild-type BioSTING were plated at a density of five million cells per 10 cm dish in cell culture medium supplemented with Doxycycline (1 μg mL^{-1}) to induce biosensor expression. The next day cells were harvested by trypsinization and electroporated with the indicated concentrations of 2'3'-cGAMP using SF Cell Line 4D-Nucleofector X Kit according to the manufacturer's protocols (Lonza). Following electroporation, the cells were resuspended in ice-cold PBS and analyzed by FACS analysis.
For extracellular 2'3'-cGAMP stimulations, HEK293T cells stably expressing wild-type BioSTING were plated at a density 750,000 cells per well of a 6-well cell culture plate in cell culture medium supplemented with Doxycycline (1 μg mL^{-1}) to induce biosensor expression. The next day, the indicated concentrations of 2'3'-cGAMP were added to the culture medium. 6 h later the cells were harvested by centrifugation and resuspended in ice-cold PBS. Biosensor activation was determined by FACS analysis.

Flow cytometry

To prepare cells for flow cytometry, cell culture media was aspirated, and the cells were harvested in ice-cold PBS. The resuspended cells were then analyzed using a LSR II flow cytometer (BD) with the following voltages: FSC-A/H/W-350, SSC-A/H/W-240, BV510(mTFP)-360, PE(mKO2)-380, and BV570(FRET)-375 volts. Data was then analyzed using FlowJo software (Tree Star).

2'3'-cGAMP enzyme immunoassay (EIA)

HEK293T cells were plated at a density of 750,000 cells per well of a 6-well cell culture plate. The next day cells were transfected with the indicated amounts of pcDNA3.1-hcGAS vector using PEI transfection reagent. Twenty-four hours later the cells were harvested by centrifugation and washed once with ice-cold PBS. Cell lysates were prepared using the 2'3'-cGAMP EIA protocol and 2'3'-cGAMP was quantified according to the manufacturer's instructions (Arbor Assays).

Western blotting

HEK293T cells were plated at a density of 750,000 cells per well of a 6-well cell culture plate. The next day cells were transfected with 1 μg pcDNA3.1-hcGAS or empty vector using PEI transfection reagent. Twenty-four hours later cells were harvested by centrifugation, and the cell pellets were lysed in Pierce RIPA buffer (Thermo Scientific) supplemented with Halt Protease and Phosphatase Inhibitor Cocktail (Thermo Scientific). Lysates were clarified by centrifugation, and protein content was normalized using Pierce BCA Protein Assay Kit (Thermo Scientific). In total, 30 μg of protein per condition were loaded onto Any kD Mini-PROTEAN TGX Precast Protein Gels (Bio-Rad) and separated by SDS-PAGE. Proteins were then transferred onto nitrocellulose membranes (Bio-Rad) at 100 V for 90 min at 4 °C. The membranes were then air dried for one hour and blocked in 5% Blotto, non-fat milk (Santa Cruz Biotechnology) dissolved in 1× TBS for one hour. Membranes were probed overnight in 5% Bovine Serum Albumin (Fisher Scientific) dissolved in 1 X TBS-T with anti-cGAS Rabbit mAb (1:1000) and anti-β-Actin Mouse mAb (1:1000) (Cell Signaling Technology). Proteins were visualized using IRDye 800CW Goat anti-Rabbit IgG Secondary Antibody (1:10000) and IRDye 680RD Goat anti-Mouse IgG Secondary Antibody (1:10000) (LI-COR Biosciences). All wash steps were carried out using 1× TBS-T. Blots

were imaged using an Odyssey Fc System (LI-COR Biosciences). Rabbit anti-cGAS (D1D3G; cat. no. 15102) and mouse anti-β-Actin (8H10D10; cat. no. 3700) monoclonal antibodies were obtained from Cell Signaling Technology.

Figures

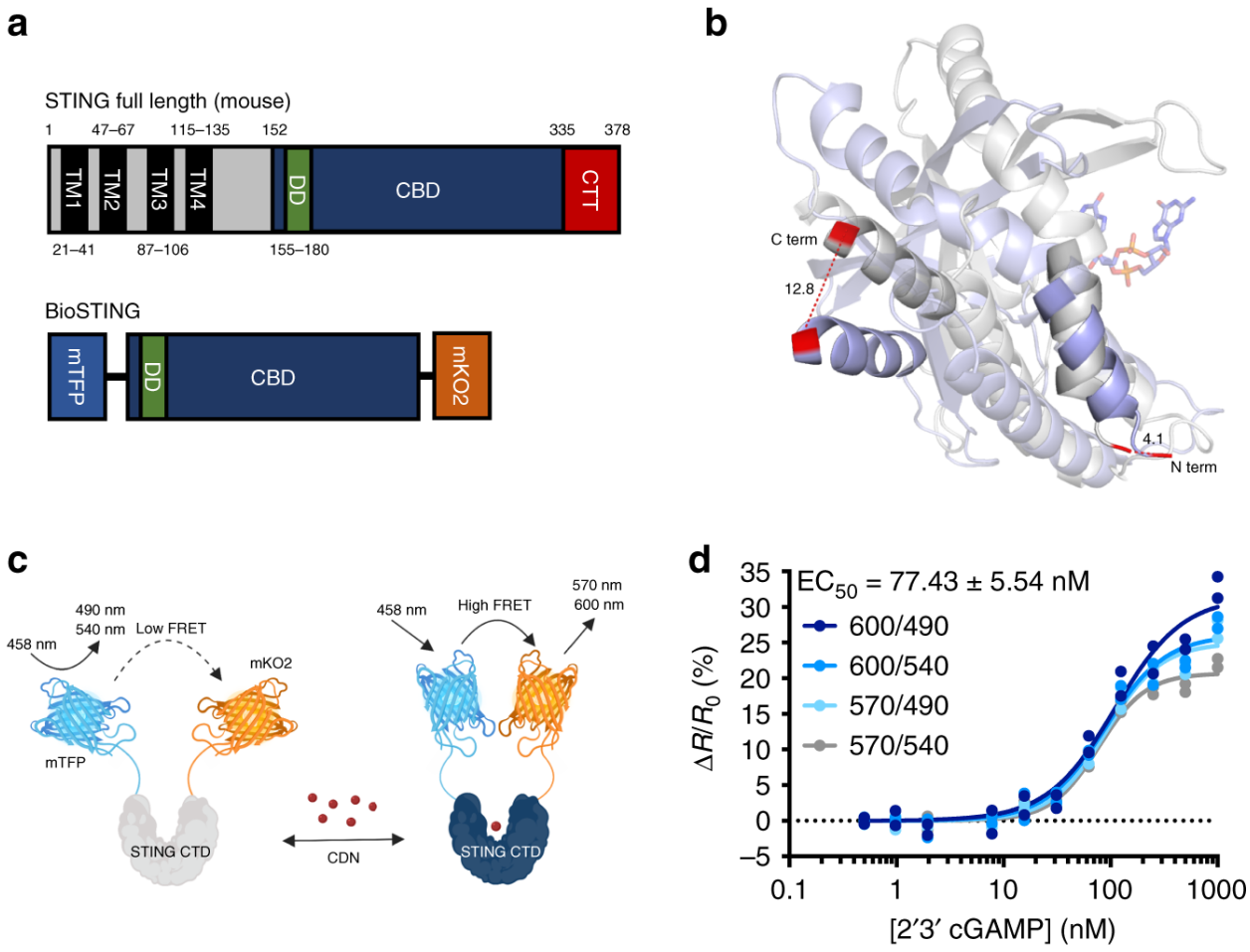

Fig. 3.1: BioSTING Design and Optimization
(a) Schematic representation of full-length STING (top) and BioSTING with additional GGSGG linker between mTFP and STING-CTD (bottom). Abbreviations are defined as follows: TM (transmembrane region), DD (dimerization domain), CBD (CDN binding domain), and CTT (C-terminal tail). **(b)** Overlay and structural alignment of human STING CTD in apo (blue) and c-di-GMP bound (gray) states (PDB 4F5E and 4F5D, respectively). Only a single monomer, which exhibits the largest structural rearrangement upon ligand binding, is shown. The N and C-terminal helices of the CTD are highlighted with the terminal residues in red and their associated displacement following ligand binding labeled in angstroms. **(c)** Model of the FRET increase which occurs upon CDN binding. Generated with Biorender.com. **(d)** Recombinant BioSTING FRET response to increasing concentrations of 2'3'-cGAMP using 458 nm excitation and listed emission wavelengths.

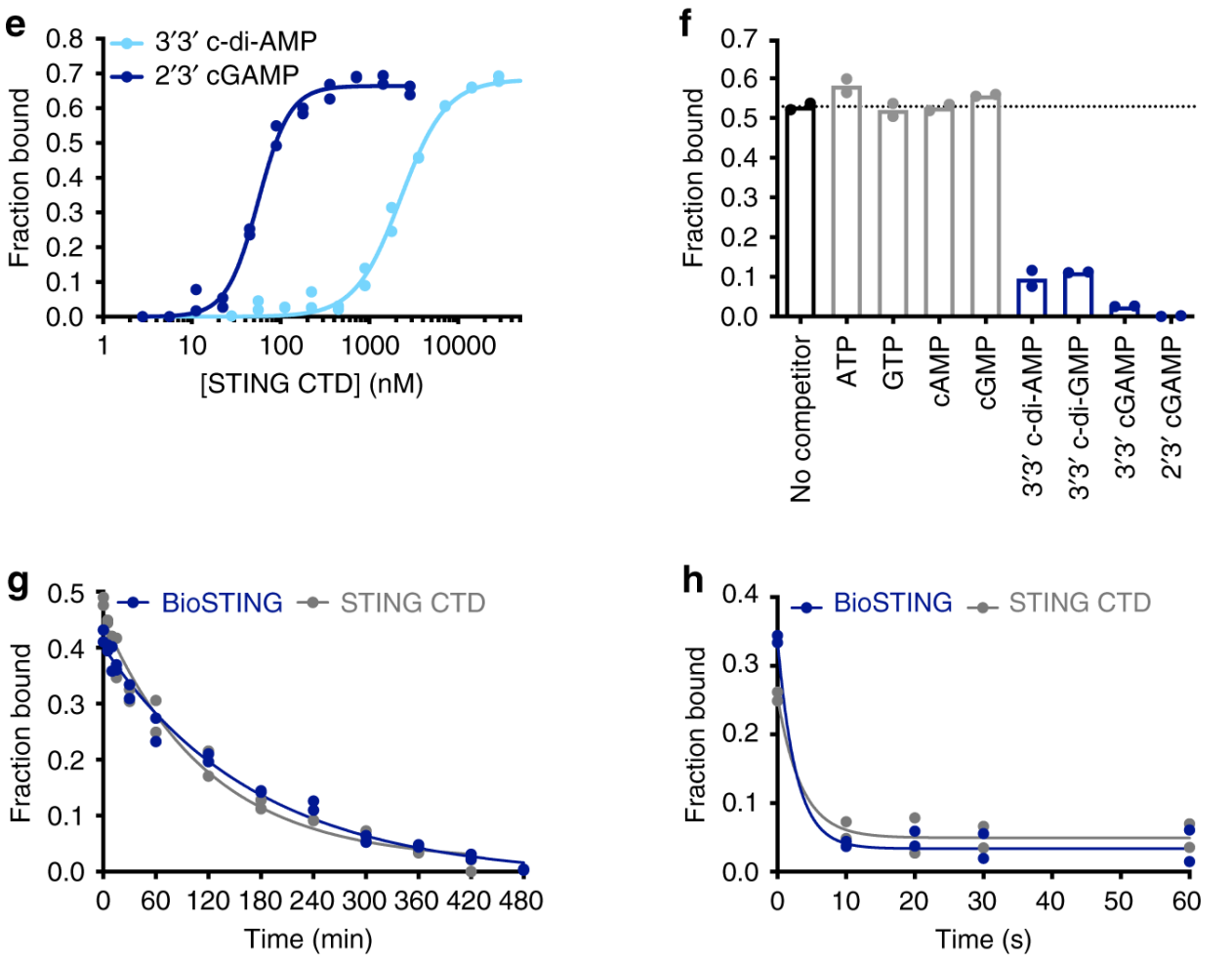

Fig. 3.1 (continued): BioSTING Design and Optimization
(e) DRaCALA radioactive nucleotide binding assay of BioSTING using ~1 nM [^{32}P] labeled 2'3'-cGAMP and 3'3'-c-di-AMP. Corresponding STING-CTD binding curve is Fig. 3.2e. **(f)** DRaCALA binding analysis of BioSTING using ~1 nM [^{32}P] labeled 2'3'-cGAMP in the presence of excess (500 µM) unlabeled nucleotides. Corresponding STING-CTD competition is Fig. 3.2f. **(g)** Time course of excess unlabeled 2'3'-cGAMP competing off bound [^{32}P] labeled 2'3'-cGAMP from BioSTING (blue) and STING-CTD (gray). **(h)** Time course of excess unlabeled 3'3'-c-di-AMP competing off bound [^{32}P] labeled c-di-AMP from BioSTING (blue) and STING-CTD (gray). In panels g and h, BioSTING was pre-incubated with ~1 nM of [^{32}P] labeled CDNs for 10 min followed by the addition of 1 mM unlabeled 2'3'-cGAMP (g) or 3'3'-c-di-AMP (h). In all panels, individual data points of $n = 2$ biological replicates are shown.

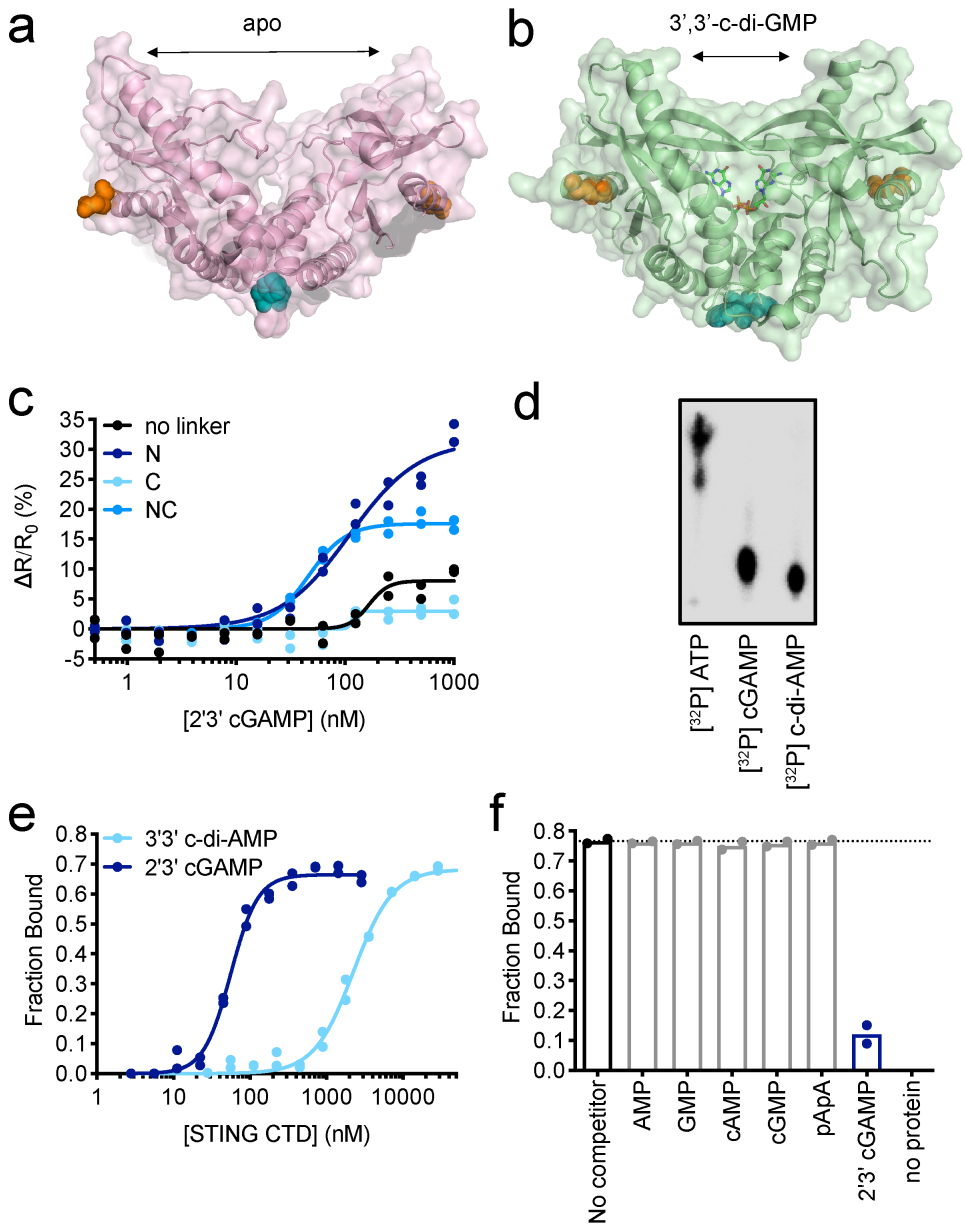

Fig. 3.2: BioSTING development and characterization

(a-b) STING crystal structures [40] with N terminus highlighted in Teal and C terminus highlighted in Orange where mTFP and mKO2 fluorophores were respectively attached (a) STING Apo structure (pink) (PDB 4F5E) and (b) STING bound to 3'3'-c-di-GMP (green) (PDB 4F5D) **(c)** FRET response in the presence of increasing 2'3'-cGAMP of prototype biosensor (black) and biosensors with GGSGG linkers on the N (dark blue), C (light blue), or both (medium blue) termini of STING-CTD **(d)** TLC analysis of enzymatically synthesized [^{32}P] labeled 2'3'-cGAMP and 3'3'-c-di-AMP and [^{32}P] ATP standard. Data are representative of two independent experiments **(e)** DRaCALA binding analysis of STING-CTD using ~1 nM [^{32}P] labeled 2'3'-cGAMP and 3'3'-c-di-AMP. **(f)** DRaCALA binding analysis of recombinant STING-CTD using ~1 nM [^{32}P] labeled 2'3'-cGAMP in the presence of excess (500 µM) unlabeled nucleotides. In all panels, individual data points of n=2 biological replicates are shown.

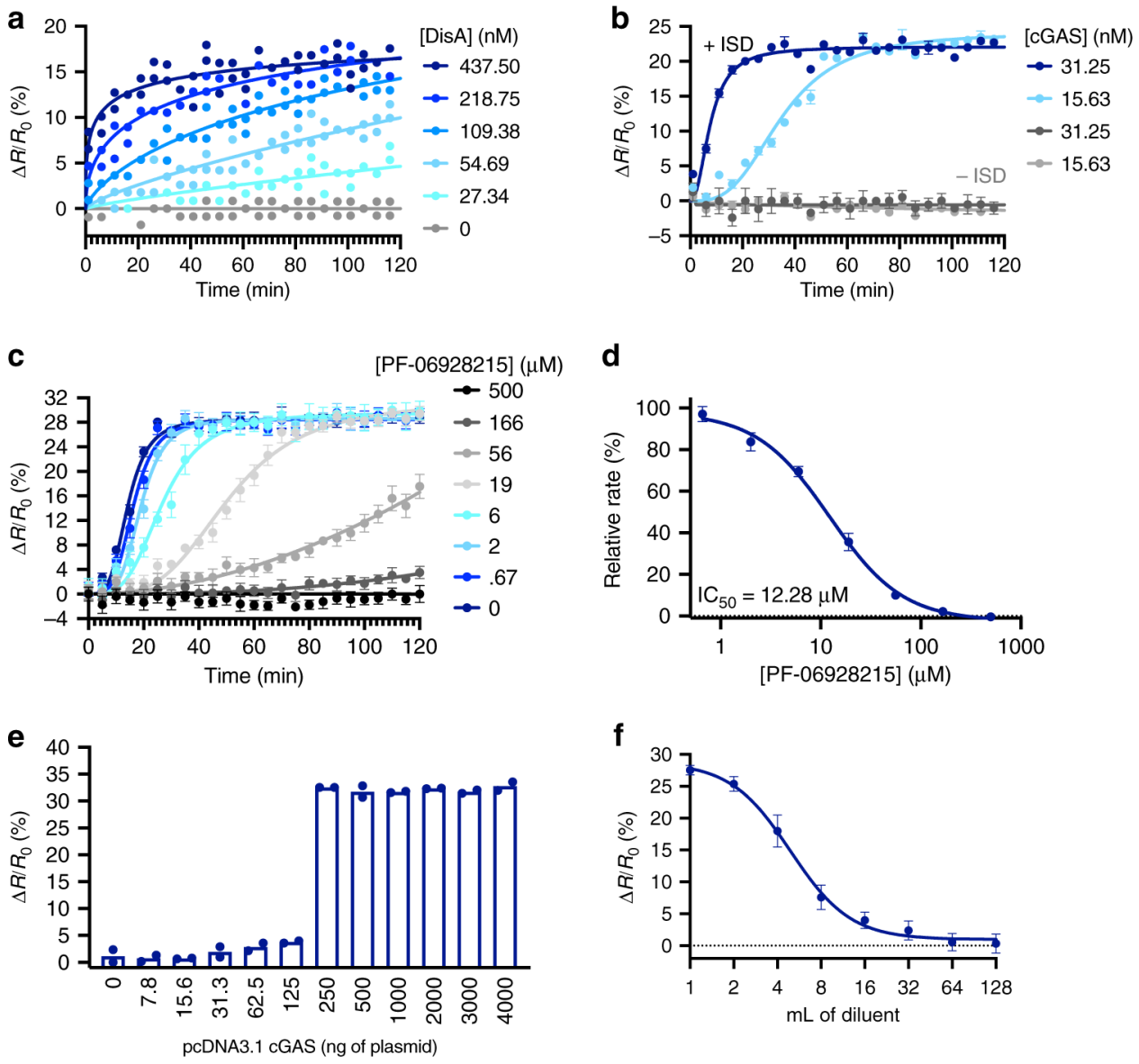

Fig. 3.3: Real-time measurement of CDN synthesis and determination of CDN levels from cellular extracts.

(a) DisA enzyme activity assay time course in the presence of increasing concentrations of the 3'3'-c-di-AMP cyclase DisA using BioSTING. (**b)** cGAS activity assay in the presence of indicated concentrations of recombinant cGAS with or without Interferon Stimulatory DNA (ISD) using BioSTING. (**c)** cGAS activity assay measuring 2'3'-cGAMP production in the presence of fixed cGAS and ISD concentrations with increasing concentrations of the cGAS inhibitor PF-06928215 using BioSTING. (**d)** Reaction linear rates calculated from panel **c** plotted versus PF-06928215 concentration and fit to IC50 curve (Prism 8). € BioSTING FRET response in the presence of methanol extracted cGAMP from HEK293T cells transfected with increasing concentrations of pCDNA3.1-cGAS. (**f)** BioSTING FRET response over two-fold serial dilutions of cGAMP methanol extracts from HEK293T cells transfected with 5 µg of pCDNA3.1-cGAS. In panels a and e, individual data points of $n = 2$ biological replicates are shown. In panels b–d and f, data are presented as mean ± s.d. of $n = 3$ (b, f) or $n = 8$ (c–d) biological replicates.

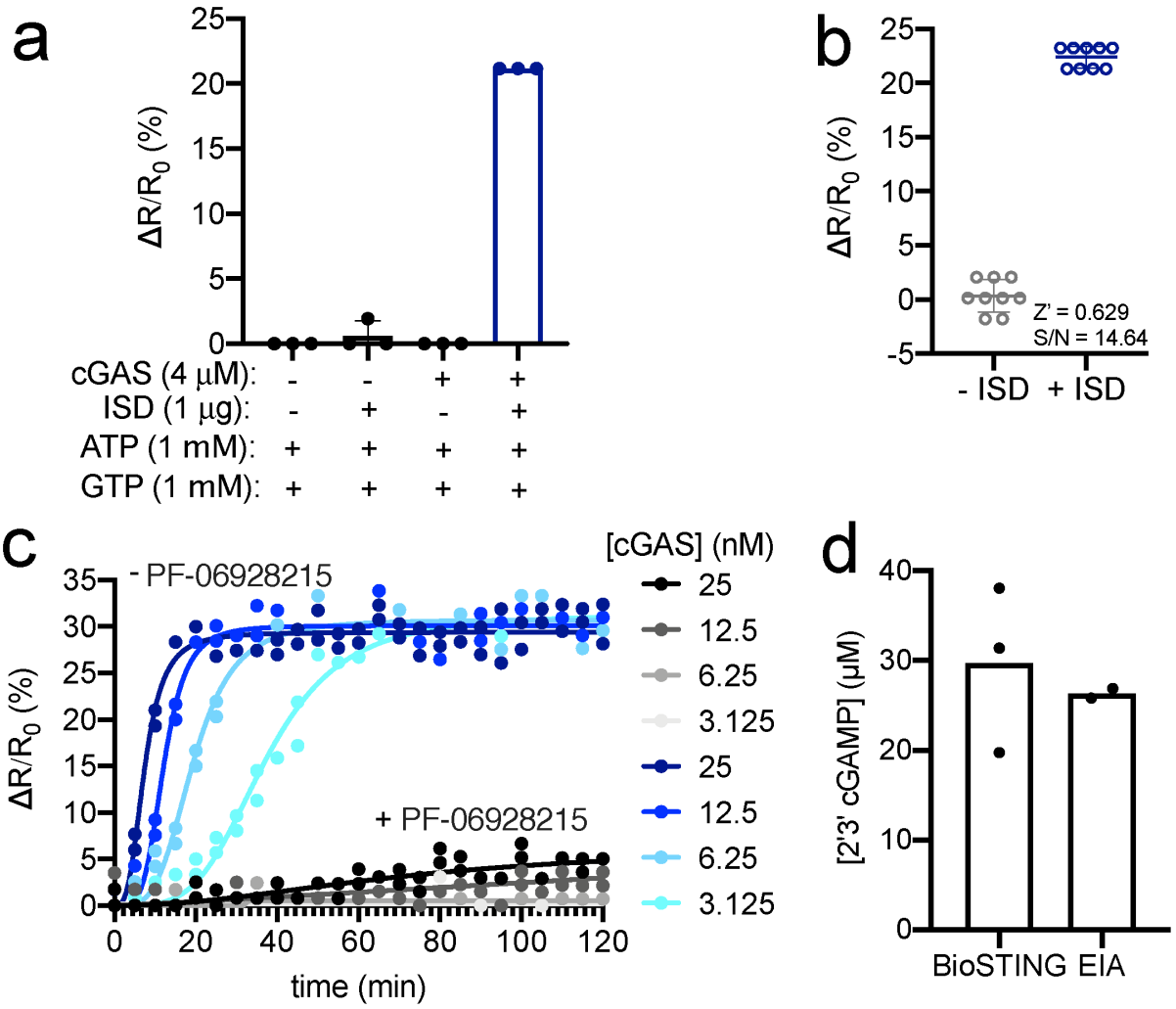

Fig. 3.4: BioSTING detection of CDNs in vitro.

(a) cGAS activity assay in the presence and absence of indicated concentrations of recombinant cGAS, ISD, ATP, and GTP using BioSTING. **(b)** Determination of Z' factor and signal to noise (S/N) ratio for BioSTING using recombinant cGAS in the presence and absence of ISD in a 96-well format. $0.5 < Z' < 1$ is considered excellent statistical reliability for high throughput screening applications. **(c)** cGAS activity assay measuring 2'3'-cGAMP production in the presence of a fixed concentration of PF-06928215 (500 μM) with increasing concentrations of cGAS using BioSTING. **(d)** Quantification of 2'3'-cGAMP levels from HEK293T cells transfected with 5 μg of pcDNA3.1-cGAS using BioSTING or EIA. Data are presented as mean ± s.d. of n=3 (a) or n=9 (b) biological replicates. In panels c and d, individual data points of n=2 (c, d) or n=3 (d) biological replicates are shown.

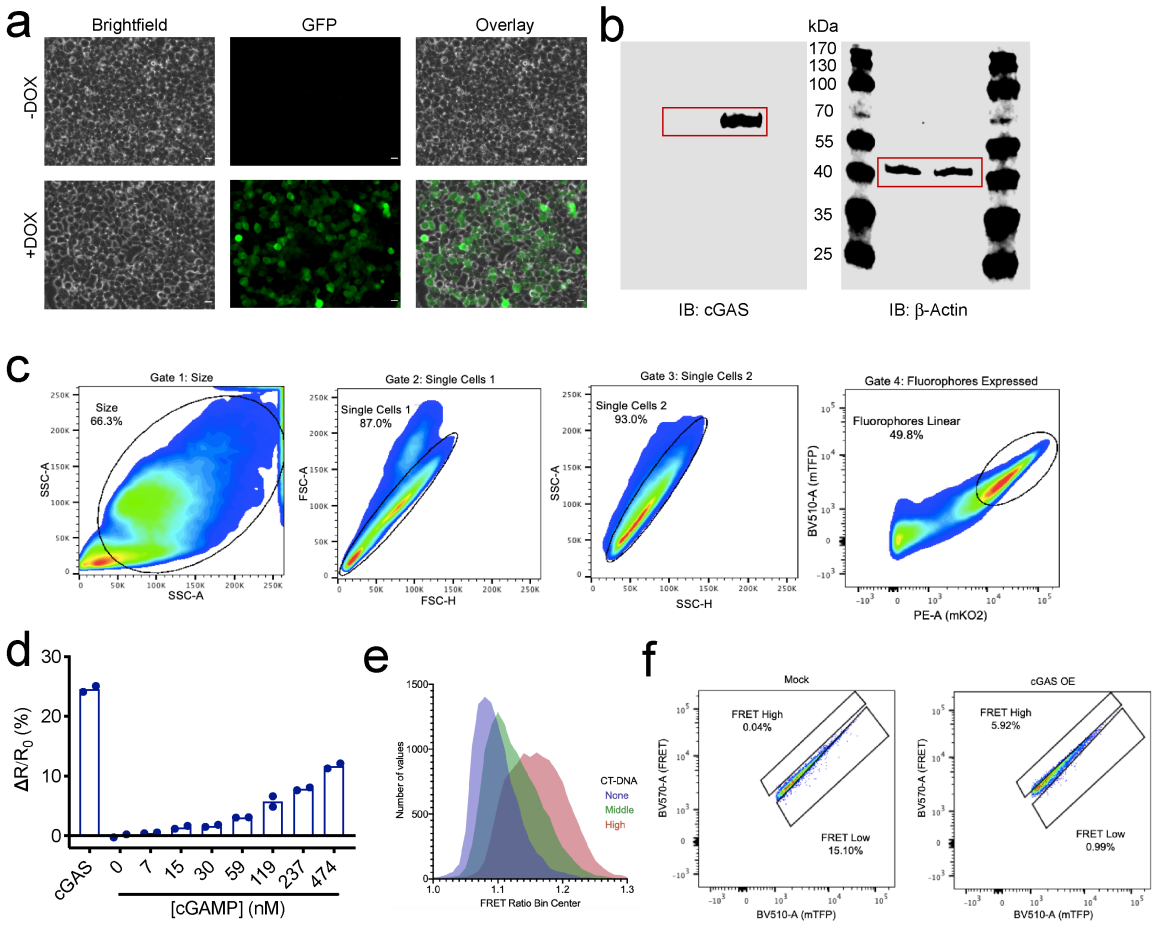

Fig. 3.5: BioSTING can detect cGAMP in cells.
(a) BioSTING expression was induced in HEK293T cells transduced with pSLIK-BioSTING for 24 hours after the addition of doxycycline or vehicle control. Biosensor expression was analyzed using a BZ-X710 microscope (Keyence), GFP filter cube (EX 470/40, DM 495, and BA 525/50), and 40X objective. Scale bars, 15 µm. Data are representative of two independent experiments. (**b**) Uncropped blots for Fig. 3.6a of HEK293T cells stably expressing BioSTING transfected with either 1 µg of empty-pCDNA3.1 vector or pCDNA3.1-cGAS vector. Data are representative of two independent experiments. (**c**) Flow analysis method: Step 1 is to set a permissive size gate, Step 2 and 3 are sorting for single cells using FSC and SSC A by H plots, and step 4 is to plot BV510 (mTFP) by PE (mKO2) and gate on cells with appropriate expression. These cells are then analyzed for BV570 (FRET)/BV510 (CFP) ratio. (**d**) HEK293T cells stably expressing BioSTING were transfected with either pCDNA3.1-cGAS or increasing concentrations of purified 2'3'-cGAMP using Lipofectamine 2000 transfection reagent according to the manufacturer's protocol and analyzed for FRET response by flow cytometry. Individual data points of n=2 biological replicates are shown. (**e**) Single cell analysis of HEK293T cells stably expressing BioSTING transfected with 10 ng of pCDNA3.1-cGAS and then transfected with a mock (0 ng), medium (156 ng), or high (1250 ng) amounts of cGAS-activating CT-DNA for 4 hours and analyzed by flow cytometry. (**f**) FRET high and low gates made on cells gated by above method (c) used to demonstrate flow selection potential. (Left) cells transfected with empty vector (Right) cells transfected with pCDNA3.1-cGAS.

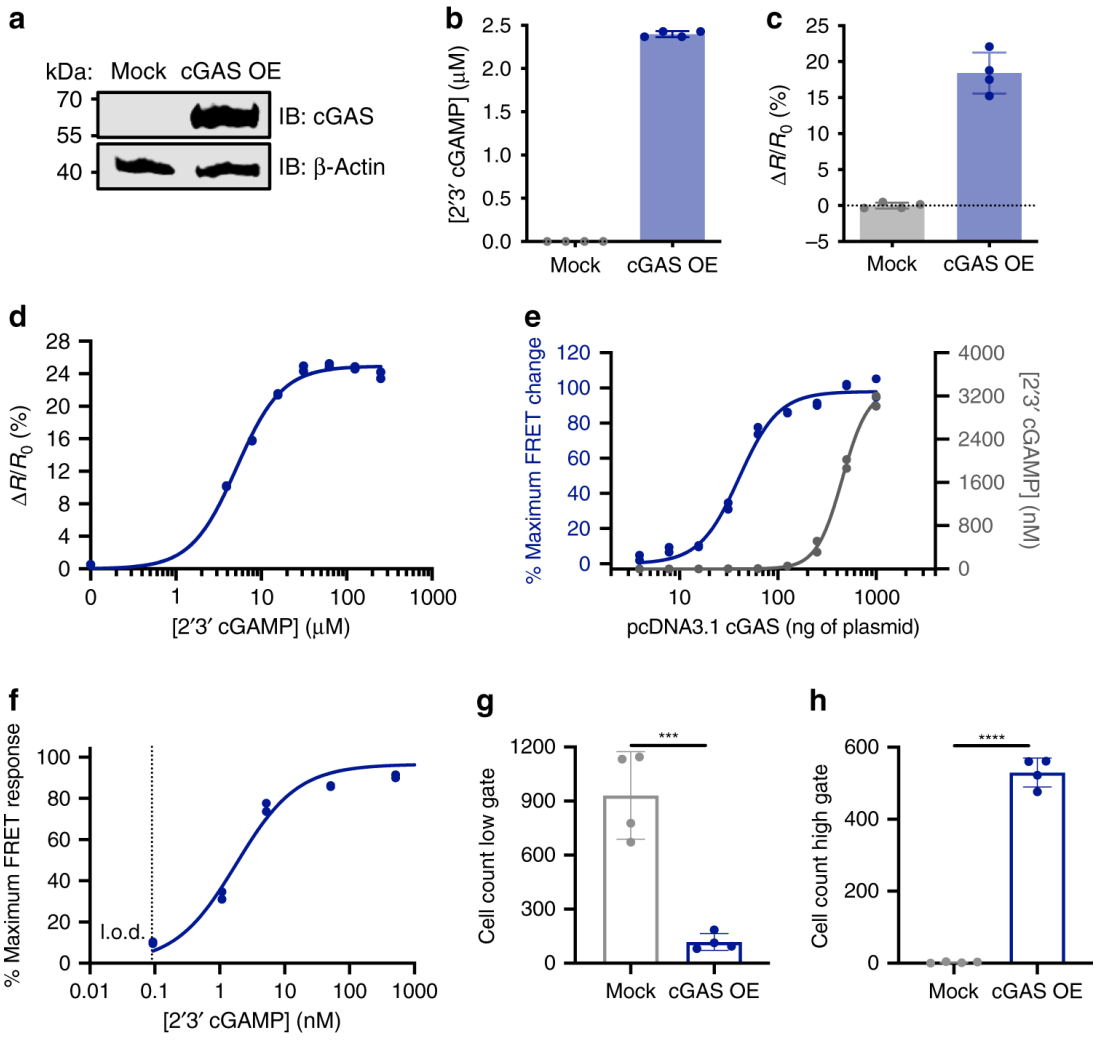

Fig. 3.6: BioSTING quantitates cGAMP in single cells in a manner compatible with flow screening.

HEK293T cells stably expressing BioSTING transfected with 1 µg of either empty pCDNA3.1 vector or pCDNA3.1-cGAS vector and analyzed for **(a)** cGAS expression by western blot (data are representative of two independent experiments), **(b)** cGAMP production by EIA analysis, and **(c)** BioSTING FRET response by flow cytometry. **(d)** HEK293T cells stably expressing BioSTING were electroporated using AMAXA (Lonza) with increasing concentrations of purified 2'3'-cGAMP and analyzed for FRET response by flow cytometry. **(e)** HEK293T cells stably expressing BioSTING were transfected with increasing concentrations of pCDNA3.1-cGAS and analyzed for FRET response by flow cytometry or for 2'3'-cGAMP production by EIA. **(f)** BioSTING FRET response from (e) graphed as a function of intracellular 2'3'-cGAMP concentration measured by EIA. **(g–h)** HEK293T cells stably expressing BioSTING transfected with either empty-pCDNA3.1 vector or pCDNA3.1-cGAS vector and analyzed by the alternative gating method in S2d for (g) cells in the low gate and (h) cells in the high gate. Statistical analyses were performed using two-tailed *t*-tests: *** denotes $P = 0.0006$ (g) and **** denotes $P = 0.0000002$ (h) (Prism 8). In panels b–c and g–h, data are presented as mean ± s.d. of $n = 4$ biological replicates. In panels d–f, individual data points of $n = 2$ biological replicates are shown.

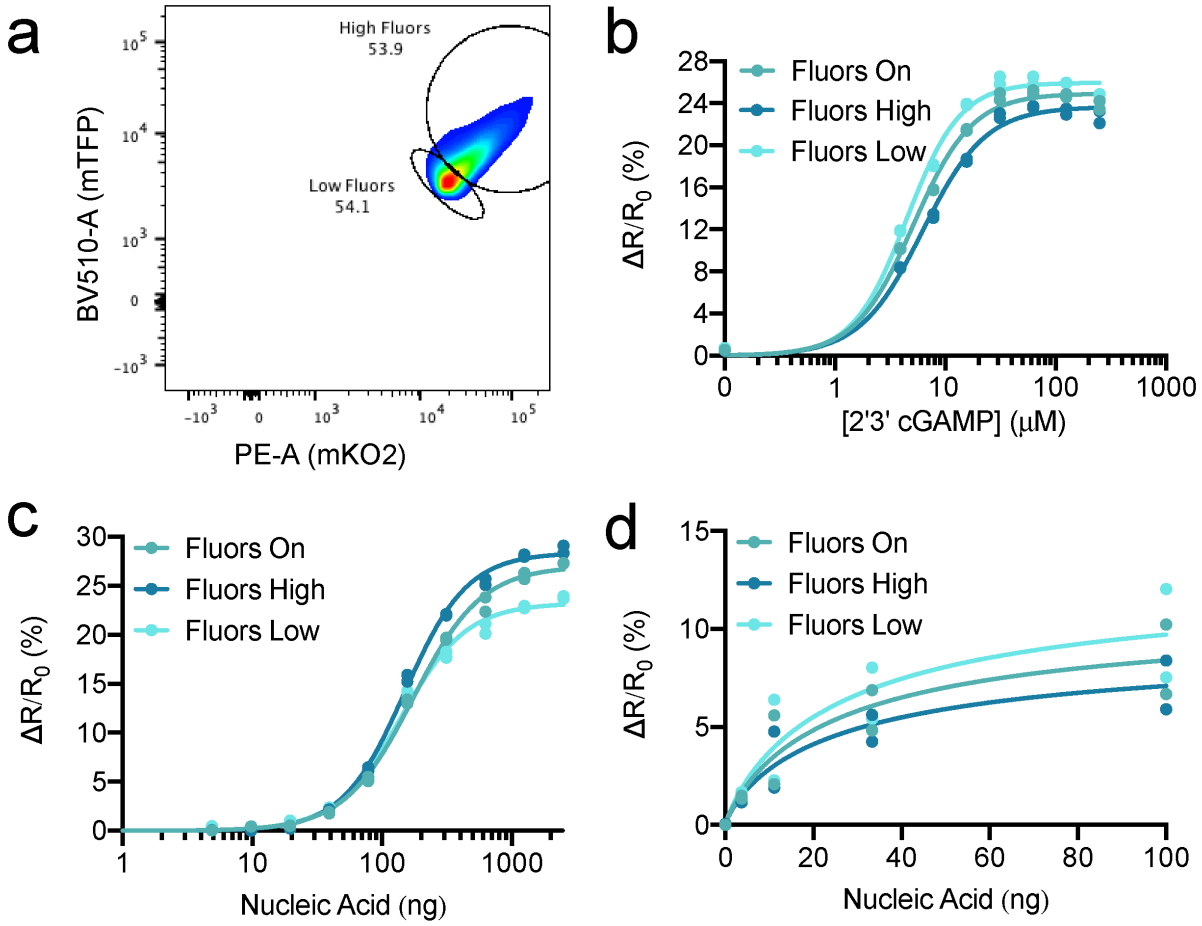

Fig. 3.7: Effects of BioSTING expression levels on FRET responses.
(a) Representative flow plot demonstrating the gating method for separation of high and low BioSTING expressing populations. Cells were first analyzed as in Figure 3.5c and then separated as shown. This method was used to collect data for all figures in this panel. (**b)** Data from Figure 3.6d was reanalyzed to compare FRET responses from populations of cells expressing high and low levels of BioSTING (**c)** Data from Figure 3.10a was reanalyzed to compare FRET responses from populations of cells expressing high and low levels of BioSTING. (**d)** Data from Figure 3.10c was reanalyzed to compare FRET responses from populations of cells expressing high and low levels of BioSTING. In all panels, individual data points of n=2 biological replicates are shown.

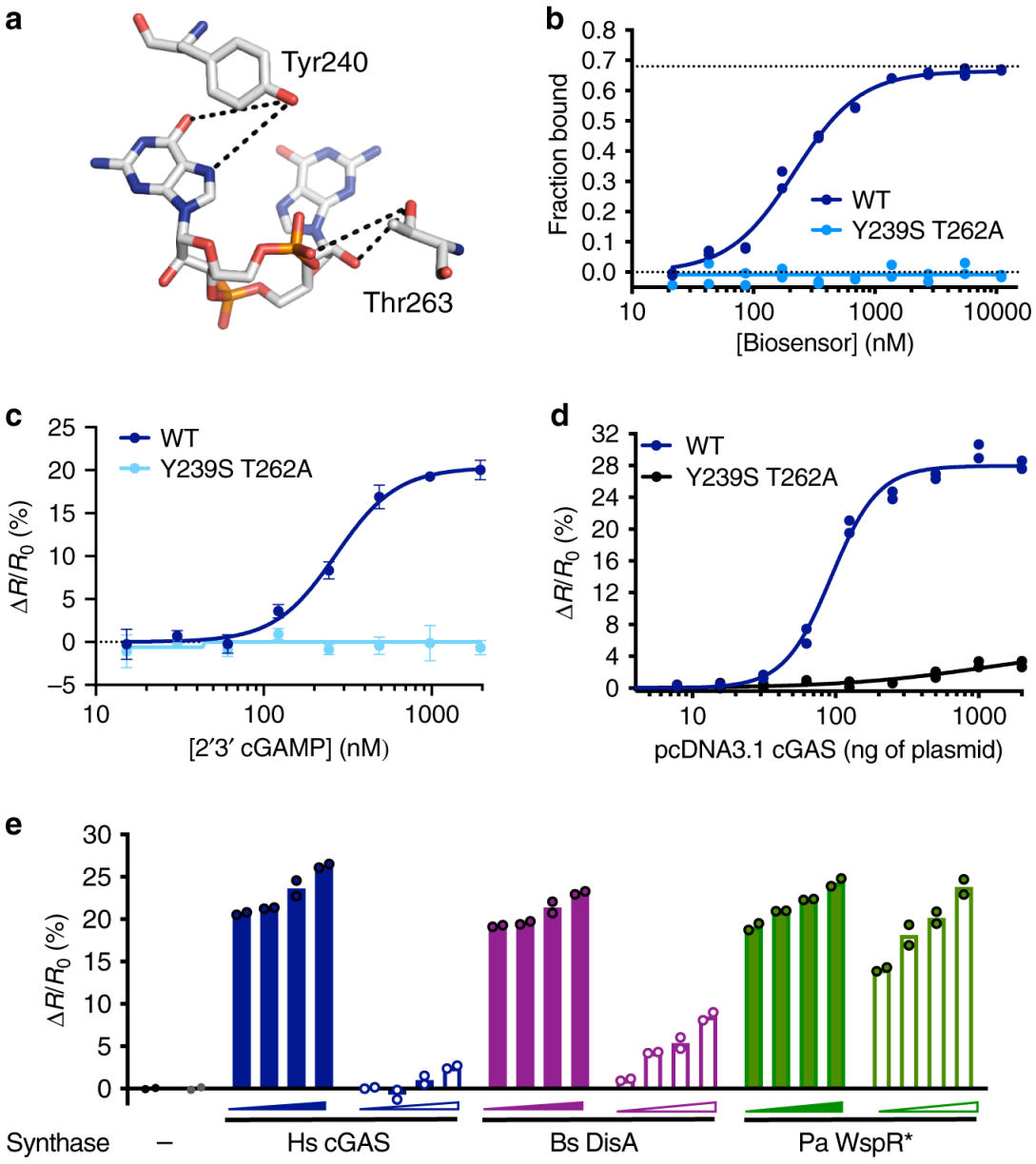

Fig. 3.8: BioSTING variants exhibit distinct specificity for metazoan and bacterial CDNs. **(a)** Interactions made by human STING residues Y240 (mouse Y239) and T263 (mouse T262) hypothesized to stabilize CDN binding in PDB 4F5D visualized in PyMol. **(b)** DRaCALA binding analysis of WT and Y239S T262A BioSTING using [^{32}P] labeled 2'3'-cGAMP. **(c)** Recombinant WT and Y239S T262A BioSTING FRET response in the presence of increasing concentrations of 2'3'-cGAMP. Data are presented as mean ± s.d. of $n = 4$ biological replicates. **(d)** HEK293T cells stably expressing WT or Y239S T262A BioSTING were transfected with increasing concentrations of pCDNA3.1-cGAS and analyzed for FRET response by flow cytometry. **(e)** HEK293T cells stably expressing WT (solid bars) or Y239S T262A (open bars) BioSTING were transfected with increasing concentrations (125, 250, 500, or 1000 ng) of expression vectors for cGAS, DisA, WspR*, or empty vector and analyzed for FRET response by flow cytometry. Data in panels b, d and e are presented as individual data points of $n = 2$ biological replicates are shown.

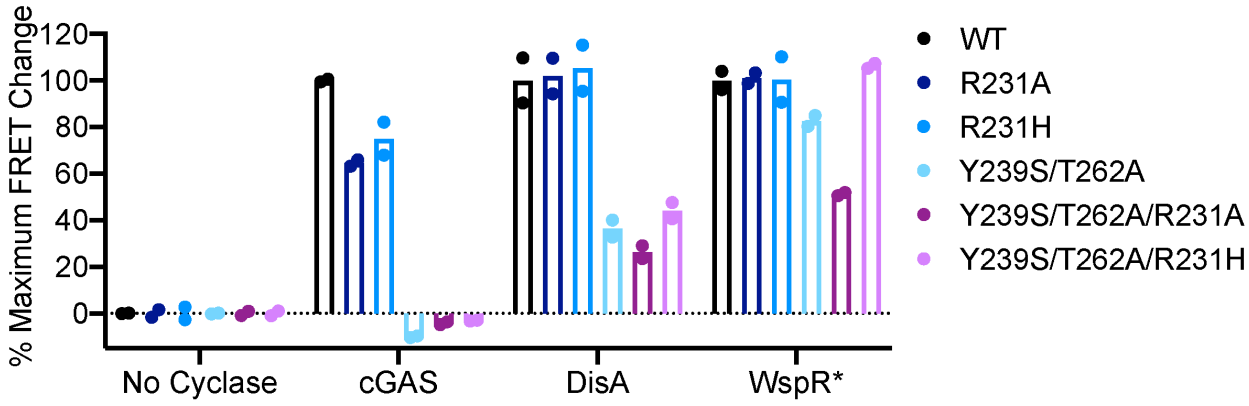

Fig. 3.9: BioSTING R231 Mutations.

HEK293T cells stably expressing WT, R231A, R231H, Y239S/T262A, R231A/Y239S/T262A, or R231H/Y239S/T262A BioSTING were transfected with expression vectors for cGAS, DisA, WspR*, or empty vector and analyzed for FRET response by flow cytometry. Individual data points of n=2 biological replicates are shown.

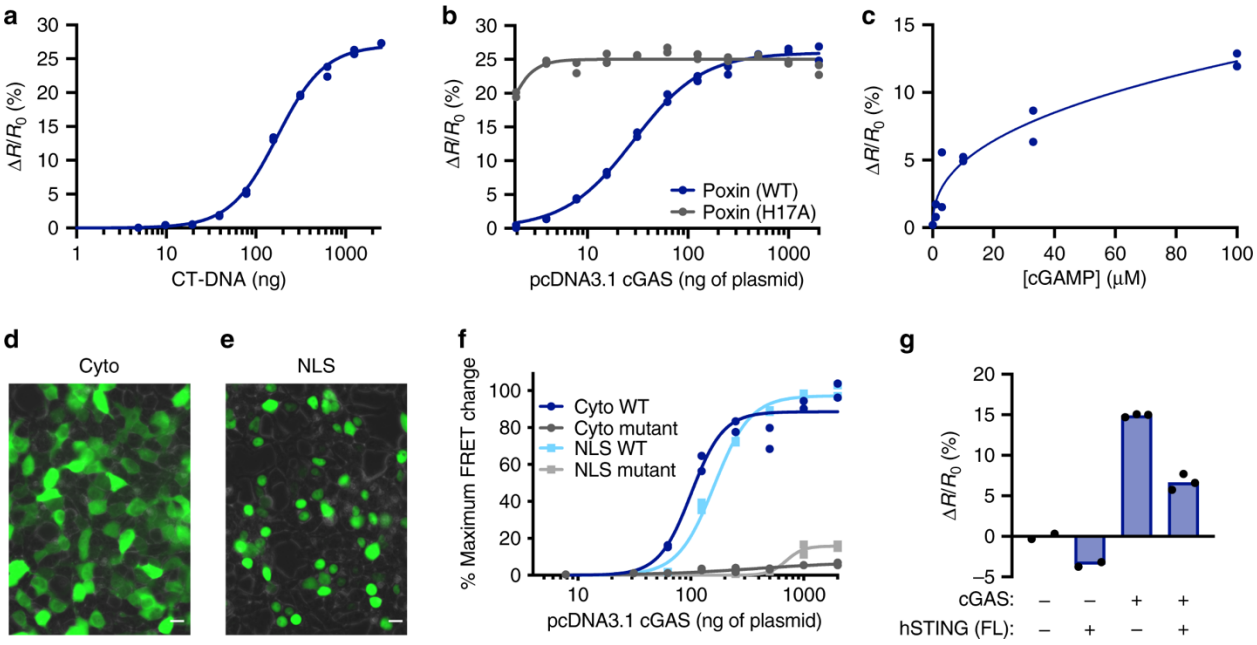

Fig. 3.10: BioSTING exhibits broad utility for monitoring diverse aspects of cGAMP signaling.

(a) HEK293T cells stably expressing BioSTING were transfected with 10 ng of pCDNA3.1-cGAS for 16-20 h then transfected again with an increasing concentration of activating CT-DNA for 4 h and analyzed by flow cytometry. (**b)** HEK293T cells stably expressing BioSTING were transfected with 3 µg of WT or H17A Poxin and increasing concentrations of pCDNA3.1-cGAS and analyzed for FRET response by flow cytometry. (**c**) Increasing concentrations of 2'3'-cGAMP were added to the media of HEK293T cells stably expressing BioSTING for 6 h and analyzed for FRET response by flow cytometry. **(d–e)** BioSTING expression was induced in HEK293T cells transduced with pSLIK-BioSTING or pSLIK-NLS-BioSTING for 24 h by the addition of doxycycline and biosensor expression was analyzed using a BZ-X710 microscope (Keyence) using brightfield and a GFP filter cube (EX 470/40, DM 495, and BA 525/50) with a 40X objective. Scale bars, 15 µm. Data are representative of two independent experiments. (**f**) HEK293T cells stably expressing untagged or NLS-tagged WT or Y239S T262A BioSTING were transfected with increasing concentrations of pCDNA3.1-cGAS and analyzed for FRET response by flow cytometry. (**g**) HEK293T cells stably expressing untagged WT BioSTING were transfected with 100 ng of cGAS expression plasmid or empty vector alone with either 100 ng of empty vector or vector expressing full-length (FL) human STING and analyzed by flow cytometry. In all panels, individual data points of $n = 2$ (a–c, f–g) or $n = 3$ (g) biological replicates are shown.

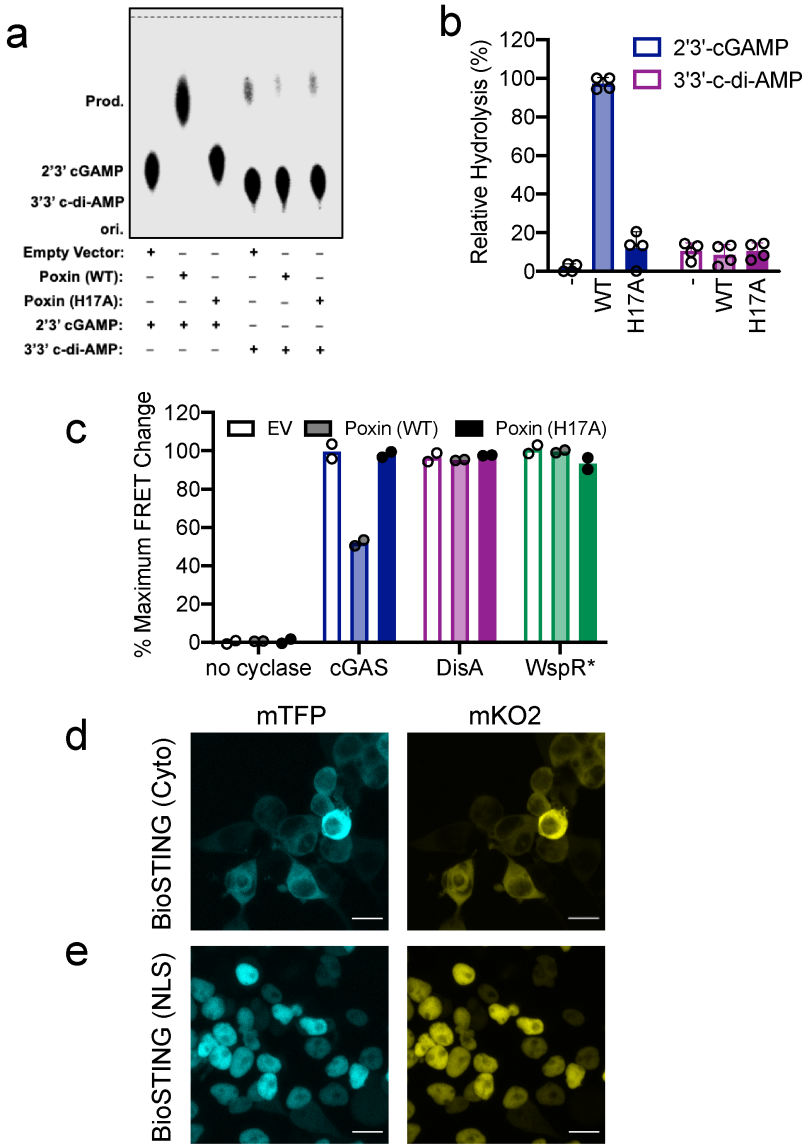

Fig. 3.11: Poxin Activity Assays and BioSTING localization.

(a) TLC analysis of [^{32}P] labeled 2'3'-cGAMP and 3'3'-c-di-AMP degradation following 1h incubation in lysates from HEK293T cells transfected with 3 µg of empty vector or plasmid expressing wildtype (WT) or catalytically-dead (H17A) Poxin. Data are representative of four independent experiments. Relative hydrolysis from four biologically, independent samples is quantified on the right in panel (**b**). Data are presented as mean ± s.d. of n=4 biological replicates. (**c**) HEK293T cells stably expressing BioSTING were transfected with 3 µg of empty vector or plasmid expressing WT or H17A Poxin along with 40 ng of plasmid expressing cGAS, DisA, or WspR* and analyzed for FRET response by flow cytometry. Individual data points of n=2 biological replicates are shown. (**d-e**) BioSTING expression was induced in HEK293T cells transduced with pSLIK-BioSTING (d) or pSLIK-NLS-BioSTING (e) for 24 hours by the addition of doxycycline and biosensor expression was analyzed by confocal microscopy using a Leica SP8X confocal microscope (Leica). Scale bars, 15 µm. Data are representative of two independent experiments.

Table 3.1: BioSTING Parameters

BioSTING Parameters	
Kd (nM)	56
EC50 (nM)	77.4
L.O.D (nM)	12.6
L.O.Q. (nM)	38.2
Dynamic Range (nM)	12-125
ΔFRET Ratio (%)	~25

Table 3.2: Primers used in this study

Primer	Use	Sequence
1	Forward Amplify STING CTD no linker	GAGGAGACTAGTTTAAATGTTGCCCACGGGCTG
2	Reverse Amplify STING CTD no linker	GAGGAGGGTACCTTCCTGACGAATGTGCCGGAG
3	Forward Amplify STING CTD GGSGG linker	GAGGAGACTAGTGGCGGATCCGGGGGCTTAAATGTTGCCCACGGGCTG
4	Reverse Amplify STING CTD GGSGG linker	GAGGAGGGTACCGCCCCCGGATCCGCCTTCCTGACGAATGTGCCGGAG
5	Forward Y239S QuickChange	GGCATCAAGAATCGGGTTTCTTCCAACAGCGTCTACGAG
6	Reverse Y239S QuickChange	CTCGTAGACGCTGTTGGAAGAAACCCGATTCTTGATGCC
7	Forward T262A QuickChange	CTGTATCCTGGAGTACGCCGCCCCCTTGCAGACCC
8	Reverse T262A QuickChange	GGGTCTGCAAGGGGGCGGCGTACTCCAGGATACAG
9	Forward R231H QuickChange	CCCAGCAAAACATCGACCATGCTGGCATCAAGAATCGG
10	Reverse R231H QuickChange	CCGATTCTTGATGCCAGCATGGTCGATGTTTTGCTGGG
11	Forward R231A QuickChange	CCCCAGCAAAACATCGACGCTGCTGGCATCAAGAATCGG
12	Reverse R231A QuickChange	CCGATTCTTGATGCCAGCAGCGTCGATGTTTTGCTGGGG
13	Forward Amplify BioSTING for pSLIK	TGATCACTAGCGTACGACCATGGGCAGCAGCCATCATCATC
14	Reverse Amplify BioSTING for pSLIK	TCTTCCAATTCGTACGTCATCCGCCAAAACAGCCAAG
15	Reverse Amplify BioSTING for pSLIK with NLS tag	TCTTCCAATTCGTACGTCAGTCCAACTTGACCCTCTTGGCAGCAGGTCCGCCAAAACAGCCAAGC

Table 3.3: Plasmids used in this study

Number	Name	Use	Source
1	pET15b-mKO2-12AA-mTFP	Contained FRET fluorophores	Gift from Samuel Miller
2	pET15b-BioSTING	Bacterial expression vector	This study
3	pET15b-BioSTING (Y239S T262A)	Bacterial expression vector	This study
4	pSLIK-Empty Vector	Eukaryotic expression vector	Gift from Andrew Oberst
5	pSLIK-BioSTING	Eukaryotic expression vector	This study
6	pSLIK-BioSTING (R231A)	Eukaryotic expression vector	This study
7	pSLIK-BioSTING (R231H)	Eukaryotic expression vector	This study
8	pSLIK-BioSTING (Y239S T262A)	Eukaryotic expression vector	This study
9	pSLIK-BioSTING (R231A Y239S T262A)	Eukaryotic expression vector	This study
10	pSLIK-BioSTING (R231H Y239S T262A)	Eukaryotic expression vector	This study
11	pSLIK-NLS BioSTING	Expresses nuclear localized BioSTING	This study
12	pSLIK-NLS BioSTING (Y239S T262A)	Expresses nuclear localized BioSTING (Y239S T262A)	This study
13	pcDNA3-empty vector	Vector Control in Eukaryotic cells	Gift from Genhong Cheng
14	pcDNA3-cGAS	Expresses full-length human cGAS in Eukaryotic cells	Gift from Genhong Cheng
15	pcDNA4-DisA	Expresses DisA in Eukaryotic cells	Gift from Philip Kranzusch
16	pcDNA4-WspR*	Expresses WspR* in Eukaryotic cells	Gift from Philip Kranzusch
17	pcDNA4-Poxin (WT)	Expresses Poxin (WT) in Eukaryotic cells	Gift from Philip Kranzusch
18	pcDNA4-Poxin (H17A)	Expresses Poxin (H17A) in Eukaryotic cells	Gift from Philip Kranzusch
19	pcDNA3-hSTING (FL)	Expresses hSTING in Eukaryotic cells	Gift from Genhong Cheng
20	pSPEEDET-mRECON	Bacterial expression vector	[106]

21	pet28-mSTING-CTD	Bacterial expression vector	Gift from Russell Vance
22	pet20b-DisA	Bacterial expression vector	[103,104]
23	pET28a-His6-SUMO-mcGAS	Bacterial expression vector	Gift from Russell Vance

Chapter 4

A luminescence based coupled enzyme assay enables high throughput quantification of the bacterial second messenger 3'3'-cyclic-di-AMP

The majority of this chapter is in revision:

Zaver, S.A., Pollock, A. J., Boradia, V.M. & Woodward, J.J. A luminescence based coupled enzyme assay enables high throughput quantification of the bacterial second messenger 3'3'-cyclic-di-AMP. *ChemBioChem.* In revision.

Summary

Cyclic dinucleotide signaling systems are found ubiquitously throughout nature allowing organisms to rapidly and dynamically sense and respond to alterations in their environments. In recent years, the secondary messenger, cyclic di-(3',5')-adenosine monophosphate (c-di-AMP), has been identified as an essential signaling molecule in a diverse array of bacterial genera. We and others have shown that defects in c-di-AMP homeostasis result in severe physiological defects and virulence attenuation in many bacterial species. Despite significant advancements in the field, there is still a major gap in the understanding of the environmental and cellular factors that influence c-di-AMP dynamics due to a lack of tools to sensitively and rapidly monitor changes in c-di-AMP levels. To address this limitation, we describe in this chapter the development of a luciferase-based coupled enzyme assay that leverages the cyclic nucleotide phosphodiesterase, CnpB, for the sensitive and high throughput quantification of 3'3'-c-di-AMP. We also demonstrate the utility of this approach for the quantification of the cyclic oligonucleotide-based anti-phage signaling system (CBASS) effector, 3'3'-cGAMP. These findings establish CDA-Luc as a more affordable and sensitive alternative to conventional c-di-AMP detection tools with broad utility for the study of bacterial cyclic dinucleotide physiology.

Introduction

Cyclic dinucleotide (CDN) second messengers have emerged as conserved signaling molecules across all domains of life. In response to altered environmental cues, CDN levels dynamically fluctuate through regulated synthesis by cyclic dinucleotide synthases and degradation by phosphodiesterases (PDEs)[7,75]. In bacteria, cyclic dinucleotides regulate a myriad of biological processes including central metabolism, cell wall homeostasis, osmoregulation, biofilm formation, motility, virulence and anti-phage immunity by modulating the activity of a diverse suite of protein and riboswitch effectors, which collectively coordinate a cellular response[6,7,9,75,104,141–147]. Additionally, bacterial cyclic dinucleotides have also been shown to interface with receptors of the metazoan innate immune system where they activate pro-inflammatory cytokine and autophagy pathways to sterilize the host of offending microorganisms[2,3,24,36,106,148,149].

Among these nucleotide small molecules, cyclic di-(3',5')-adenosine monophosphate (3'3'-c-di-AMP, c-di-AMP or CDA) has been shown to play an essential role in regulating the lifestyles of a diverse range of clinically significant bacterial genera[146,150]. Within these bacterial species, cyclic di-AMP production is mediated by a conserved family of diadenylate cyclase (DAC) domain containing proteins, of which, five classes have been characterized to date[146]. Degradation of CDA is catalyzed by dedicated phosphodiesterase enzymes, which fall into two major classes: DHH-DHHA1 (aspartate-histidine-histidine) domain or HD (histidine-aspartate) domain containing proteins[103,146]. Although the mechanisms of CDA synthesis and degradation are quite conserved, the arsenal of c-di-AMP receptors appears to vary among bacterial species[146]. This may allow the output of c-di-AMP signaling systems to be tailored to the individual needs of specific bacteria.

Despite significant advancements in the understanding of the components of bacterial c-di-AMP signaling networks, a detailed understanding of the environmental and cellular cues that regulate CDA homeostasis are lacking. A few studies have attempted to answer this question, mostly through the use of genetic approaches[142,145,147,151,152]. These studies revealed a role for potassium

and glutamate availability in the regulation of c-di-AMP synthesis, underscoring the importance of this molecule in maintaining osmotic balance[145,147,152]. Additionally, both DHH-DHHA1-type and HD-type phosphodiesterases have been shown to be inhibited by the alarmone (p)ppGpp, suggesting a link between amino acid starvation and cyclic di-AMP signaling[103,153]. Nevertheless, understanding of c-di-AMP regulation is still rudimentary and high-throughput, unbiased genetic and phenotypic screens to identify the factors that regulate CDA dynamics have not been performed.

Such studies are currently intractable due to the lack of tools to sensitively, affordably and rapidly quantify c-di-AMP levels. A sensitive liquid chromatography mass-spectrometry (LC-MS) based assay for CDA detection and quantification was previously described; however, mass-spectrometry based approaches are low throughput and require technical knowledge as well as access to expensive machinery[3,150]. RNA-aptamer based biosensors for c-di-AMP as well as other CDNs have been developed; unfortunately, these sensors typically have low affinities for their cognate CDNs (~3-30 μM for c-di-AMP)[154]. More recently, commercial enzyme immunoassays (EIAs) have become available for the quantification of several cyclic dinucleotide species. While these assays have reasonable throughput, they can be quite costly and have narrow dynamic ranges, which limits their utility in high-throughput screening campaigns. To address these limitations, we describe the development of a luciferase-based coupled-enzyme assay termed CDA-Luc to quantify 3'3'-c-di-AMP. This assay can be paired with conventional ATP detection assays to sensitively and affordably quantify c-di-AMP over a broad dynamic range and is likely to enable fundamental discoveries relating to c-di-AMP physiology.

Results

Selection of a suitable 3'3'-c-di-AMP phosphodiesterase

Recently, a luciferase based coupled enzyme assay for quantification of the metazoan CDN 2'3'-cGAMP (cGAMP-Luc) was described[108]. This assay takes advantage of the mammalian phosphodiesterase ectonucleotide pyrophosphatase (ENPP1), which hydrolyzes 2'3'-cGAMP to GMP and AMP. Following cleavage, AMP is subsequently phosphorylated to ADP by the enzyme polyphosphate:AMP phosphotransferase (PAP). Next, the enzyme myokinase is utilized to phosphorylate ADP to ATP. Finally, the ATP produced by the coupled-enzyme assay can be quantified using a conventional ATP detection kit. We hypothesized that a similar approach could be utilized to develop a sensitive assay to quantitate 3'3'-c-di-AMP. Several classes of CDA phosphodiesterase have been identified to date; however, many of these enzymes are incompatible with this approach as they linearize c-di-AMP to 5'-pApA rather than separating the two fused nucleotides. In addition, many of these enzymes are integral membrane proteins, making them challenging to work with and difficult to produce in large quantities (Figure 4.1)[146]. Fortunately, a small group of soluble, AMP-producing CDA phosphodiesterases have been identified, of which the *Mycobacterium tuberculosis* PDE, cyclic nucleotide phosphodiesterase B (CnpB), has been best characterized[155–159]. Thus, we hypothesized that Mtb CnpB would be an optimal candidate for a coupled enzyme-based c-di-AMP quantification assay.

Optimization of CnpB hydrolytic activity

We began by optimizing the *in vitro* reaction conditions in order to maximize CnpB hydrolytic activity. Recombinant hexahistidine-tagged CnpB was produced in *E. coli* and purified to apparent homogeneity in a single-step using Ni^{2+} affinity chromatography (Figure 4.2a). We next monitored the activity of CnpB towards bis-*p*-nitrophenyl phosphate (BNPP) a non-specific, colorimetric reporter substrate for phosphatase and phosphodiesterase enzymes. Consistent with previous reports, we observed no enzymatic activity in the absence of added metal cations (Figure 4.2b, c)[155–158]. We next tested CnpB activity against a panel of divalent metal ions. Among this array, CnpB activity was highest in the presence of Mn^{2+} and completely absent in the presence of Mg^{2+} (Figure 4.2b, c). Minor activity was observed with other metal cations including Co^{2+}; however, as Mn^{2+} resulted in the highest activity, it was selected for all future assays. As some metal ions have been shown to interfere with downstream steps in the AMP detection assay, we next titrated $MnCl_2$ in order to determine the minimal concentration required for full CnpB activity[108]. Based on these assays, we concluded that a minimum concentration of approximately 30 μM $MnCl_2$ is required for optimal activity (Figure 4.2d). Finally, as phosphodiesterase activity is highly sensitive to pH, CnpB activity was monitored across a pH gradient (Figure 4.2e). Consistent with previous reports, CnpB activity was highest at alkaline pH with a pH optimum of approximately 8.5 (Figure 4.2e)[155–158]. Taken together, a buffer formulation of [Tris-Cl pH 8.5, 0.1 mM MnCl2, 100 mM NaCl] was selected for all future assays.

Analysis of CnpB 3'3'-c-di-AMP binding and hydrolysis

Having optimized the activity of CnpB using the mock-substrate BNPP, we next sought to directly monitor CnpB hydrolytic activity against 3'3'-c-di-AMP under these assay conditions. To that end, [^{32}P]-labeled 3'3'-c-di-AMP was enzymatically synthesized and affinity purified to near homogeneity (Figure 4.3a). CnpB binding to 3'3'-c-di-AMP was confirmed by differential radial capillary action of ligand assay (DRaCALA). As a positive control, the mammalian c-di-AMP binding protein reductase controlling NF-κb (RECON) was employed, yielding a Kd of 68 nM[106]. In the absence of $MnCl_2$, binding of 3'3'-c-di-AMP to CnpB was weak and non-saturating with a Kd > 17 μM (Figure 4.3b). Interestingly, addition of $MnCl_2$ to the binding buffer appeared to enhance the affinity of CnpB towards CDA by five-fold with a Kd of approximately 3 μM (Figure 4.3b). These results were in agreement with the previously reported low micromolar Km of CnpB for 3'3'-c-di-AMP[155–158]. Additionally, these results support a role for Mn^{2+} in enhancing substrate binding in addition to increasing catalytic activity.

We next monitored the hydrolytic activity of CnpB by thin layer chromatography (TLC) analysis. We began by testing whether CnpB could cleave nanomolar concentrations of 3'3'-c-di-AMP to AMP, its previously reported product. Trace concentrations (~1 nM) of [^{32}P] labeled c-di-AMP were incubated with CnpB in the presence and absence of $MnCl_2$. After 2 hours, we observed complete hydrolysis of c-di-AMP to a product that migrated slightly slower than the [α-^{32}P] ATP standard (Figure 4.3c). Interestingly, we also observed complete hydrolysis of CDA in the absence of $MnCl_2$ under these assay conditions, perhaps because only trace quantities of substrate were used (Figure 4.3c). Addition of alkaline phosphatase completely converted the CnpB product to inorganic phosphate confirming that AMP and not 5'-pApA is indeed the reaction product (Figure 4.3c). Finally, in order for this approach to be suitable for quantification of 3'3'-c-di-AMP, CnpB must also be capable of completely hydrolyzing low micromolar concentrations of CDA. To test this, we incubated CnpB with 1 μM 3'3'-c-di-AMP spiked with 1 nM [^{32}P] labeled c-di-AMP.

After 24 hours, we observed complete hydrolysis of c-di-AMP to AMP with minimal degradation of AMP to adenosine and free inorganic phosphate (Figure 4.3d). Taken together, these data show that CnpB is capable of completely converting low nanomolar to low micromolar concentrations of CDA to AMP and suggest that this could be a viable approach for a c-di-AMP quantification assay.

Coupling of CnpB with commercially available AMP detection assays

Over the years, several commercial AMP detection assays have been formulated. Of these, the AMP-GloTM assay is one of the most commonly used. In the first reaction, AMP is converted to ADP by the enzyme PAP using polyphosphate as a substrate. In the next and final step, myokinase is coupled to luciferase. Thus, as ATP is produced by myokinase, it is subsequently utilized by luciferase to oxidize the luciferin substrate producing a luminescence signal (Figure 4.4a)[108]. Luciferase activity is proportional to the amount of ATP in the sample, enabling quantification. Thus, we began by coupling CnpB to the commercially available AMP-Glo™ assay. Promisingly, we were able to detect AMP produced by CnpB using this assay; however, consistent with previous findings, luciferase activity was not linear when plotted on a standard linear-linear plot greatly limiting the quantitative capabilities of this approach (Figure 4.4b)[108]. We observed similar non-linearity using purified AMP as the substrate suggesting that this problem is inherent to the assay itself and not the CnpB digestion step (Figure 4.4c). Interestingly, re-analysis of the data using a log-log plot resulted in a much more linear standard curve for both 3'3'-c-di-AMP and AMP with quantification limits of approximately 7.8 nM (Figure 4.5a, b). In contrast, commercially available luciferase-based ATP detection kits displayed linear standard curves under both analysis methods (Figures 4.4d, e and 4.5c, d). These results suggest that it is indeed possible to sensitively quantify 3'3'-c-di-AMP using commercially available AMP detection kits with this alternative analysis method; however, the high costs associated with these kits greatly diminishes their utility for high throughput screening campaigns.

Development of CDA-Luciferase (CDA-Luc) Assay

Recently, a revised method for AMP-detection, termed AMP-Luc, was described and successfully employed for quantification of 2'3'-cGAMP[108]. Here, the reaction components remained the same as in the AMP-GloTM assay, but the coupled steps in the assay were rearranged to allow complete conversion of AMP to ATP prior to ATP detection using a conventional luciferase-based ATP detection kit (Figure 4.6a). This is accomplished by coupling myokinase to PAP instead of luciferase as in the conventional assay. Second, the PAP and myokinase coupled step is allowed to proceed longer (up to three hours) to ensure complete conversion of the AMP to ATP. Simply, rearranging the steps in the assay in this way was shown to dramatically improve the quantitative capabilities of the assay. Encouraged by these findings, we hypothesized that we could couple CnpB with AMP-Luc to generate a robust and affordable method for 3'3'-c-di-AMP quantification. To that end, the enzyme PAP was expressed in *E. coli* and purified to near homogeneity using a single Ni^{2+} affinity purification step (Figure 4.6b and 4.7a). The activity of the purified PAP was confirmed by coupling the enzyme to commercially available myokinase and monitoring ATP production using the Kinase Glo® assay (Figure 4.6c). We next tested the ability of AMP-Luc to detect CnpB-digested 3'3'-c-di-AMP. Incubation of 3'3'-c-di-AMP with CnpB followed by detection with AMP-Luc resulted in a robust luciferase response that was

abolished in the absence of either CDA or CnpB (Figure 4.6d). Notably, the resulting luminescence signal was stable for at least one hour after addition of the Kinase Glo® reagent, allowing for flexibility in assay design (Figure 4.7b). Thus, these data suggest that the reconfigured AMP-Luc assay could be used to detect 3'3'-c-di-AMP using CnpB.

We next examined the ability of this assay to quantify AMP. As expected, the AMP-Luc assay yielded a robust standard curve for both AMP and 3'3-c-di-AMP with quantification limits of 31.2 or 7.8 nM, depending on the analysis method (linear-linear vs log-log) (Figure 4.6e, f and 4.7c, d). Next, we compared the standard curve of 3'3'-c-di-AMP generated using CDA-Luc to the standard curve of pure ATP using Kinase-Glo®. This yielded largely overlapping standard curves with low nanomolar limits of quantification, suggesting that there is no further room for optimization of the CDA-Luc assay (Figure 4.8a). Taken together, these data suggest that this approach is robustly quantitative for 3'3'-c-di-AMP. To be consistent with the nomenclature of preceding literature, we named this assay CDA-Luc [108].

Having optimized the CDA-Luc assay, we next sought to further characterize the limitations of the assay. As this assay relies on ATP-mediated oxidation of luciferin, we hypothesized that there would be an upper limit for c-di-AMP quantification based on the availability of luciferin substrate. To that end, we performed an extended c-di-AMP titration which yielded a standard curve that was linear up to 5 µM (Figure 4.8b). CDA concentrations greater than 5 µM resulted in a departure from linearity. Because each cleaved c-di-AMP molecule yields two AMP molecules, these results were consistent with the 10 µM specification for ATP quantification by the Kinase Glo® reagent.

In addition to cleaving 3'3'-c-di-AMP, CnpB has also been shown to possess some hydrolytic activity towards 3'3'-c-di-GMP, albeit with markedly reduced affinity[155–157]. Many c-di-AMP producing bacteria also encode catalytic machinery for the production and degradation of c-di-GMP. Thus, we wanted to make sure that any GMP produced by hydrolysis of CDG would not interfere with CDA quantification by the CDA-Luc assay. To that end, we generated CDA standard curves in the presence and absence of a fixed (1 µM) concentration of GMP. This yielded overlapping standard curves with similar limits of quantification (Figure 4.8c). Thus, although CnpB is capable of degrading c-di-GMP, its product GMP will not interfere with c-di-AMP quantification by the CDA-Luc assay.

Finally, we wanted to determine whether the CDA-Luc assay could successfully be employed under different buffer conditions. To do this, we previously described chemically defined minimal media for growth of *Listeria monocytogenes*[3,103]. Growth of *L. monocytogenes* in this medium enabled the identification of 3'3'-c-di-AMP by mass spectrometry analysis and has since been used by our lab and others to monitor the regulation of c-di-AMP homeostasis[3,103,151]. Thus, known concentrations of 3'3'-c-di-AMP were titrated into *L. monocytogenes* minimal media supplemented with streptomycin and subjected to digestion with CnpB followed by quantification by AMP-Luc. We observed robust linearity of the CDA-Luc assay in chemically defined media with a quantification limit of 7.8 nM, similar to the standard assay (Figure 4.9a, b). In contrast, conditioned, defined minimal media from Δ*dacA*Δ*oppA L. monocytogenes* deficient for endogenous c-di-AMP synthesis demonstrated only minor luminescence differences upon titration of pure 3'3'-c-di-AMP suggesting the presence of interferents in the sample (Figure 4.9c). We also tested the performance of CDA-Luc in a commonly used lysis buffer, RIPA buffer. This yielded a

mostly linear standard curve with a reduced quantification limit of approximately 62.5 nM, likely due to the presence of detergents in the lysis buffer (Figure 4.9d). These results suggest that CDA-Luc can be employed under a variety of buffer conditions but that interferents can be present in complex biological samples.

RECON enables affinity purification of c-di-AMP from biological samples in a manner compatible with CDA-Luc quantification

Although CDA-Luc is capable of monitoring c-di-AMP levels in chemically defined buffers, quantification of c-di-AMP from complex biological samples is hindered by biological interferents and large quantities of AMP, ADP, and ATP (ANPs), which would interfere with the CDA-Luc assay. We and others have previously utilized CDN binding proteins for the purification of cyclic dinucleotides from complex mixtures[45,104,106,108,160]. Most bacterial and host c-di-AMP binding proteins have low micromolar affinities for CDA, limiting their utility for affinity purification as large quantities of recombinant protein would be required[24,104,146,149]. We recently identified a host 3'3'-c-di-AMP binding protein, RECON, with high affinity for c-di-AMP (Kd of 68 nM) (Figure 4.3b)[106]. We have also previously utilized RECON affinity purification (RECAP) to specifically capture [32P] labeled c-di-AMP from crude reaction mixtures containing ANPs and free inorganic phosphates (Figures 4.3a and 4.10a, b)[45,160]. Thus, we hypothesized that RECON could be employed as an upstream step to purify 3'3'-c-di-AMP prior to quantification using the CDA-Luc assay.

Recombinant hexahistidine-tagged RECON was immobilized onto NiNTA agarose beads and incubated with samples containing known concentrations of 3'3'-c-di-AMP. Following washing, the RECON-CDA complexes were eluted from the beads using imidazole. The resulting supernatant was then boiled to remove the bound c-di-AMP, which was then quantified using CDA-Luc. Quantification of RECON-purified CDA by CDA-Luc resulted in a linear standard curve with a quantification limit of approximately 31.2 nM and a detection limit of 1.2 nM (Figure 4.10c). We hypothesize that the quantification limit could be improved further by reducing the volume of elution buffer. We performed a similar analysis using c-di-AMP dissolved in *L. monocytogenes* chemically defined media. This approach yielded a standard curve with a quantification limit of 39 nM and a dynamic range of 5 nM – 5 μM (Figure 4.10d). We next sought to determine whether RECAP is able to extract c-di-AMP away from interferents generated from biological samples. Implementing RECAP on conditioned media doped with known concentrations of 3'3'-c-di-AMP as in figure 4.9c allowed for high fidelity recovery and detection of c-di-AMP (Figure 4.10e). Thus, RECAP allows for c-di-AMP quantification in a wide array of samples, even when interferents which disrupt the CDA-Luc assay are present.

Having established the utility of RECON affinity purification for CDA quantification, we next sought to monitor the intracellular and secreted levels of c-di-AMP from various *L. monocytogenes* strains with altered levels of c-di-AMP production, degradation, and/or secretion. As expected, we observed no c-di-AMP in a *L.m.* strain deficient for CDA production (Δ*dacA*Δ*oppA*) (Figure 4.10f, g). Consistent with our previous findings, deficiency of both CDA phosphodiesterases (Δ*pgpH*Δ*pdeA*) resulted in an approximately four-fold enhancement in both the intracellular and extracellular levels of c-di-AMP as compared to the wildtype (WT) strain (Figure 4.10f, g). Finally, depletion of TetR (*tetR::Tn917*), a negative regulator of multidrug resistant transporters

that export c-di-AMP, augmented the levels of c-di-AMP secreted into the bacterial growth medium (Figure 4.10f, g). Interestingly, depletion of TetR did not affect intracellular levels of 3'3'-c-di-AMP. We believe that this is due to compensation for enhanced export by increased production and/or decreased degradation of CDA. Taken together, these data demonstrate that pairing of RECON affinity purification (RECAP) with the CDA-Luc assay can enable detection of c-di-AMP from complex biological samples.

Comparison of CDA-Luc to LC-MS

Having optimized and established the utility of CDA-Luc for quantification of 3'3'-c-di-AMP, we next wanted to compare it to the established gold standard for c-di-AMP quantification, LC-MS. To that end, we generated standard curves of known concentrations of c-di-AMP doped with an isotopically labeled internal standard and subjected them to LC-MS analysis. This yielded a robustly linear standard curve with a quantification limit of 50 nM and a dynamic range from 5 nM – 5 μM (Figure 4.11a, c). Consistent with our previous results, CDA-Luc performed similarly with a limit of quantification of 39 nM (Figure 4.11b, c). Collectively, these data establish CDA-Luc as a high throughput and affordable alternative to LC-MS based quantification of 3'3'-c-di-AMP without loss of sensitivity.

Quantification of 3'3'-cGAMP using CDA-Luc

Recently, cyclic oligonucleotides have been shown to play an important signaling role in bacterial, innate anti-phage immunity. In this context, cyclic oligonucleotide second messengers are synthesized by cGAS/DncV-like nucleotidyltransferases (CD-NTases) upon infection with bacteriophage[6,9,75]. The resulting second messenger then activates a cognate effector protein culminating in abortive phage infection through the death of the infected cell, thereby protecting the greater bacterial community[6,9,75]. Among the cyclic oligonucleotide-based anti-phage signaling systems (CBASS), 3'3'-cGAMP synthesized by DncV has been the most well studied; nevertheless, the mechanisms that trigger 3'3'-cGAMP production remain poorly elucidated. Such studies would benefit from sensitive and affordable quantification tools. Interestingly, CnpB has been shown to possess hydrolytic activity against 3'3'-cGAMP[157]. Thus, we hypothesized that the CnpB-based CDA-Luc assay could also be utilized to quantify 3'3'-cGAMP. To that end, we first confirmed that CnpB could utilize 3'3'-cGAMP using a competitive BNPP hydrolysis assay. CnpB was incubated with BNPP in the presence of increasing concentrations of 3'3'-cGAMP and production of *p*-nitrophenol was monitored (Figure 4.12a). Consistently, we observed a dose-dependent decrease in the rate of BNPP hydrolysis in the presence of 3'3'-cGAMP (Figure 4.12a). Having confirmed utilization of 3'3'-cGAMP by CnpB, we next tested the ability of the CDA-Luc assay to quantify purified 3'3'-cGAMP. This analysis yielded a linear standard curve with a quantification limit of 62.5 nM and a detection limit of approximately 3 nM, in line with the limits of the ENPP1-based cGAMP-Luc assay (Figure 4.12b)[108]. Taken together, these data demonstrate the utility of CDA-Luc for the quantification of the CBASS second messenger 3'3'-cGAMP.

Concluding Remarks

In this study, we have developed a robustly quantitative, high throughput luminescence-based c-di-AMP detection method. We show that the unique ability of the *M. tuberculosis*

phosphodiesterase CnpB to cleave CDA to AMP can be leveraged for the design of a highly sensitive and precise c-di-AMP quantification assay. CnpB can easily be paired with commercially available AMP detection kits to yield a moderately quantitative c-di-AMP detection method; however, rearrangement of the coupled steps greatly improved the quantitative capabilities of the assay yielding a dynamic range spanning four orders of magnitude while maintaining the general accessibility of this approach. We also show that the high affinity mammalian c-di-AMP binding protein, RECON, can be leveraged to purify c-di-AMP from complex biological mixtures, allowing this method to be used in diverse investigations. Thus, we anticipate that CDA-Luc can be readily employed to replace mass-spectrometry based measurements of c-di-AMP.

Over the last decade, cyclic di-AMP has emerged as a widespread secondary messenger among both environmental and pathogenic microbes[104,142–144,146]. In bacteria, c-di-AMP has been shown to regulate a number of diverse processes including central metabolism, cell wall homeostasis, osmoregulation, genome integrity, antibiotic resistance, biofilm formation, sporulation, and virulence among others[104,141–147,152]. These pleiotropic functions of cyclic di-AMP are mediated by a diverse suite of protein and ribonucleotide effectors. Because of these critical functions, c-di-AMP is unique amongst all other cyclic dinucleotides as it is both essential for many bacterial species as well as toxic at elevated concentrations; however, the molecular mechanisms involved in regulation of c-di-AMP synthesis and degradation are still poorly understood[146,150].

Several classes of cyclic di-AMP synthases have been identified to date with the DacA or CdaA family of diadenylate cyclases being the largest[146]. Structurally DacA consists of an N-terminal transmembrane domain and a catalytic C-terminal DAC domain. In many bacterial species, DacA is encoded in a three gene operon consisting of an extracytoplasmic regulatory protein, CdaR or YbbR, and the phosphoglucosamine mutase, GlmM, an enzyme involved in peptidoglycan biosynthesis, both of which have been shown to modulate the activity of DacA—providing evidence for crosstalk between cell wall biosynthesis and c-di-AMP signaling networks[146,161,162]. In addition to synthesis, degradation of c-di-AMP must be dynamically regulated in order to allow bacteria to sense and respond to alterations in their environment. In *L. monocytogenes*, two phosphodiesterases that cleave c-di-AMP to the linear dinucleotide pApA have been identified, PdeA and PgpH[103,141]. Structurally, PdeA is comprised of a membrane spanning N-terminus followed by a PAS domain, GGDEF domain, and catalytically active DHH-DHHA1 domain[141]. PgpH consists of an N-terminal extracellular domain followed by a seven-pass transmembrane domain reminiscent of G-protein coupled receptors and a C-terminal catalytic HD domain[103]. While these enzymes have somewhat redundant functions, biochemical studies revealed that PdeA is the dominant c-di-AMP hydrolase during intracellular bacterial growth; whereas, PgpH is the dominant hydrolase during broth culture[103]. It is likely that these enzymes, through their regulatory domains, respond to specific environmental or cellular cues as *L. monocytogenes* transitions from its environmental, saprophytic lifestyle to its pathogenic lifecycle. Thus, a detailed understanding of the factors that regulate c-di-AMP dynamics is of fundamental importance to the field.

Development of the first sensitive, high throughput c-di-AMP quantification tool will make these fundamental lines of inquiry tractable. We expect that pairing unbiased genomic and chemical screens with CDA-Luc measurements will uncover the key cellular and environmental factors that regulate c-di-AMP dynamics during infection and environmental growth. As cyclic di-AMP is both essential and toxic, high throughput drug screens using CDA-Luc to identify compounds that

either target c-di-AMP cyclases or phosphodiesterases would have promising potential for the development of novel antimicrobial agents. Because CDA is also a potent inducer of host innate immune responses, PDE inhibitors could be especially promising as they would induce bacterial cell death while simultaneously boosting host, antibacterial inflammatory responses. Additionally, we also provide evidence that CDA-Luc can be used for the quantification of other bacterial CDN species, namely 3'3'-cGAMP. Although not tested here, we also expect that CDA-Luc could be used to quantify other AMP-containing 3'3'-CDNs including 3'3'-cUAMP. We anticipate that this will make CDA-Luc not only useful to the study of c-di-AMP signaling but also the newly discovered CBASS field. One caveat to CDA-Luc based measurements is that this approach, like mass-spectrometry and EIA, only allows population level measurements of c-di-AMP at a single time point following destruction of the biological sample. Thus, there is still a need for the development of reversible, continuous, single cell methods for in vivo quantification of c-di-AMP. Nevertheless, we anticipate that CDA-Luc will facilitate fundamental discoveries relating to c-di-AMP dynamics and physiology for years to come.

Materials and Methods

Materials

ATP, [α-^{32}P], 3000Ci/mmol 10mCi/ml, 250 µCi was obtained from PerkinElmer (cat. no. BLU003H250UC). 3'3'-c-di-AMP and 3'3'-cGAMP were obtained from Invivogen (cat. no. tlrl-nacda and cat. no. tlrl-nacga, respectively). AMP-Glo™ (cat. no. V5011), Cell Titer Glo® (cat. no. G7570), and Kinase Glo® (cat. no. V6712) reagents were obtained from Promega Corporation. Sodium Hexametaphosphate (polyphosphate) was obtained from Sigma-Aldrich (cat. no. 71600). Myokinase from rabbit muscle was obtained from Sigma-Aldrich (cat. no. M3003). RIPA buffer was purchased from ThermoFisher Scientific (cat. no. 89900).

Cloning

M. tuberculosis CnpB gene (Rv2837c) was amplified by PCR from Mtb H37Rv genomic DNA using the forward primer 5'-GAAATACCATATGACGACGATCGACCCAAGG and reverse primer 5'-GAATATCAAGCTTCTAACCAAGCGCCGCGC. The resulting PCR product was cloned into the NdeI /HindIII site of pET28b vector to generate an N-terminal His-tagged polypeptide. The resulting CnpB expression vector was confirmed by sequencing using the T7 and T7 Term universal primers (GENEWIZ).

Codon optimized PAP gene from *A. johnsonii* 210A (GenBank accession no. AB092983) was chemically synthesized (Integrated DNA Technologies). The gBlock™ was then PCR amplified using the forward primer 5'-GAGGAGCATATGGATACAGAGACTATCGCAAGTGC and reverse primer 5'-GAGGAGAAGCTTATCAGTGTCGCGGTCGGC. The resulting PCR product was cloned into the NdeI/HindIII site of pET20b vector to generate a C-terminal His-tagged polypeptide. The resulting PAP expression vector was confirmed by sequencing using the T7 and T7 Term universal primers (GENEWIZ).

Protein Expression and Purification

For expression of Mtb CnpB, plasmid encoding CnpB was transformed into LOBSTR (low background strain) BL21 (DE3) chemically competent *E. coli*. Overnight cultures of the resulting bacterial strains were used to inoculate 1.5 L of LB broth at a 1:100 dilution. Bacterial cultures were grown to OD_{600} 0.6 at 37°C. The cultures were then cooled down to room temperature and protein expression was induced by the addition of 0.5 mM isopropyl β-D-1-thiogalactopyranoside (IPTG) for 18 hours at 16°C. Bacteria were harvested by centrifugation at 9000 x g for 5 minutes, and the cell pellets were resuspending into 30 mL of Buffer A [50 mM Tris pH = 8.0, 500 mM NaCl, 20 mM Imidazole, 5 mM β-Mercaptoethanol (BME), and 1 mM phenylmethylsulfonyl fluoride (PMSF)] and cooled on ice for 30 minutes. Bacteria were lysed by sonication on ice and clarified by centrifugation at 40,000 x g for 30 minutes at 4°C. The resulting clarified lysate was bound to HisPur NiNTA Resin (Thermo Scientific). The resin was washed with 100 column volumes of buffer A and bound proteins were eluted in Buffer B [50 mM Tris-Cl pH = 8.0, 500 mM NaCl, 300 mM Imidazole, 5 mM β-Mercaptoethanol (BME), and 1 mM phenylmethylsulfonyl fluoride (PMSF)]. Eluates were assessed for purity by SDS-PAGE analysis. Proteins were concentrated using Vivaspin 6 (5000 MWCO) centrifugal concentrators and then buffer exchanged

into storage buffer [50 mM Tris-Cl pH = 8.5, 100 mM NaCl] using PD-10 desalting columns (GE Healthcare). The desalted proteins were concentrated again using Vivaspin 6 (5000 MWCO) centrifugal concentrators, supplemented with glycerol (25%), snap frozen using liquid nitrogen, and stored at -80°C until use.

For expression of PAP, plasmid encoding PAP was transformed into LOBSTR (low background strain) BL21 (DE3) chemically competent *E. coli*. Overnight cultures of the resulting bacterial strains were used to inoculate 1.5 L of LB broth at a 1:100 dilution. Bacterial cultures were grown to OD_{600} 0.4 at 37°C. The cultures were then cooled down to room temperature and protein expression was induced by the addition of 0.5 mM isopropyl β-D-1-thiogalactopyranoside (IPTG) for 18 hours at 16°C. Bacteria were harvested by centrifugation at 9000 x g for 5 minutes, and the cell pellets were resuspending into 30 mL of Buffer A [50 mM Tris pH = 8.0, 500 mM NaCl, 20 mM Imidazole, 5 mM β-Mercaptoethanol (BME), and 1 mM phenylmethylsulfonyl fluoride (PMSF)] supplemented with 0.2 mg mL-1 Lysozyme and cooled on ice for 30 minutes. Bacteria were lysed by sonication on ice and clarified by centrifugation at 40,000 x g for 30 minutes at 4°C. The resulting clarified lysate was bound to HisPur NiNTA Resin (Thermo Scientific). The resin was washed with 100 column volumes of buffer A and bound proteins were eluted in Buffer B [50 mM Tris-Cl pH = 8.0, 500 mM NaCl, 300 mM Imidazole, 5 mM β-Mercaptoethanol (BME), and 1 mM phenylmethylsulfonyl fluoride (PMSF)]. Eluates were assessed for purity by SDS-PAGE analysis. Proteins were concentrated using Vivaspin 6 (5000 MWCO) centrifugal concentrators and then buffer exchanged into storage buffer [50 mM Tris-Cl pH = 8.5, 100 mM NaCl] using PD-10 desalting columns (GE Healthcare). The desalted proteins were concentrated again using Vivaspin 6 (5000 MWCO) centrifugal concentrators, aliquoted into PCR strip tubes, snap frozen using liquid nitrogen, and stored at -80°C until use.

For expression of RECON, plasmid encoding mRECON was transformed into Rosetta (DE3)pLysS chemically competent *E. coli*. Overnight cultures of the resulting bacterial strains were used to inoculate 1.5 L of LB broth at a 1:100 dilution. Bacterial cultures were grown to OD_{600} 0.5 at 37°C. The cultures were then cooled down to room temperature and protein expression was induced by the addition of 0.5 mM isopropyl β-D-1-thiogalactopyranoside (IPTG) for 18 hours at 16°C. Bacteria were harvested by centrifugation at 9000 x g for 5 minutes, and the cell pellets were resuspending into 30 mL of Buffer A [50 mM Tris pH = 8.0, 500 mM NaCl, 20 mM Imidazole, 5 mM β-Mercaptoethanol (BME), and 1 mM phenylmethylsulfonyl fluoride (PMSF)] and cooled on ice for 30 minutes. Bacteria were lysed by sonication on ice and clarified by centrifugation at 40,000 x g for 30 minutes at 4°C. The resulting clarified lysate was bound to HisPur NiNTA Resin (Thermo Scientific). The resin was washed with 100 column volumes of buffer A and bound proteins were eluted in Buffer B [50 mM Tris-Cl pH = 8.0, 500 mM NaCl, 300 mM Imidazole, 5 mM β-Mercaptoethanol (BME), and 1 mM phenylmethylsulfonyl fluoride (PMSF)]. Eluates were assessed for purity by SDS-PAGE analysis. Proteins were concentrated using Vivaspin 6 (5000 MWCO) centrifugal concentrators and then buffer exchanged into storage buffer [40 mM Tris pH 7.5, 100 mM NaCl, 20 mM MgCl2] using PD-10 desalting columns (GE Healthcare). The desalted proteins were concentrated again using Vivaspin 6 (5000 MWCO) centrifugal concentrators, supplemented with glycerol (25%), snap frozen using liquid nitrogen, and stored at -80°C until use.

BNPP Cleavage Assays

Unless otherwise noted, CnpB activity assays were carried out in clear polystyrene 96-well plates using assay buffer [50 mM Tris-Cl pH = 8.5, 100 mM NaCl] in 100 µL of assay buffer at 37°C. Indicated concentrations of CnpB and specified metal ions were diluted into assay buffer and reactions were initiated by the addition 0.2 mM BNPP. CnpB reaction rates were monitored by measuring the absorbance at 405 nm (OD_{405}) using a plate reader (Synergy HTX multimode reader, BioTek Instruments).

Synthesis of [^{32}P] 3'3'-c-di-AMP

Briefly, 1 µM of *B. subtilis* DisA and 1 µM α-[^{32}P] ATP (Perkin-Elmer) (100 µL total reaction volume) was incubated in buffer [40 mM Tris pH 7.5, 100 mM NaCl, 20 mM MgCl2] at 37°C overnight. The following day, the reaction was spiked with an additional 1 µM DisA enzyme and incubated at 37°C for four hours. The reaction was terminated by boiling for 10 min at 95°C. The resulting crude [^{32}P] 3'3'-c-di-AMP mixture was further purified using RECON affinity purification: 100 µM His-tagged mRECON was immobilized on HisPur Ni-NTA resin for 30 min on ice. The resin was washed twice with buffer and held on ice until use. The RECON resin was incubated with the crude [^{32}P] 3'3'-c-di-AMP mixture for 30 minutes at room temperature. Following removal of the supernatant, the Ni-NTA resin was washed five times with ice cold buffer. 500 uL of buffer was added to the resin and the sample was incubated at 95°C for 10 minutes. The slurry was transferred to a minispin column and [^{32}P] 3'3'-c-di-AMP was eluted by centrifugation. [^{32}P] 3'3'-c-di-AMP was analyzed for purity by Thin Layer Chromatography (TLC) analysis using Polygram CEL300 PEI TLC plates (Machery-Nagel) in running buffer containing 1:1.5 (vol/vol) saturated (NH4)2SO4 and 1.5 M NaH2PO4 pH 3.6.

DRaCALA Binding Assays

Two-fold serial dilutions of CnpB in buffer [50 mM Tris-Cl pH = 8.5, 100 mM NaCl] with and without 0.1 mM $MnCl_2$ were incubated with ~1 nM [^{32}P] 3'3'-c-di-AMP for 10 minutes at 4°C. Samples were blotted onto nitrocellulose membranes and air dried for 15 minutes. Membranes were then exposed onto PhosphorImager screens (GE Healthcare) and developed using a Sapphire Biomolecular Imager (Azure Biosystems). Data were analyzed using Fiji/ImageJ software as previously described and graphed using GraphPad Prism 8 software.

[^{32}P] 3'3'-c-di-AMP Hydrolysis Assays

Briefly, recombinant CnpB was incubated with radiolabeled 3'3'-c-di-AMP in buffer [50 mM Tris-Cl pH = 8.5, 100 mM NaCl] at 37°C. After indicated times, samples were dotted onto TLC plates and allowed to air dry for 5-10 minutes and then separated in TLC running buffer. TLC plates were then air dried for 30-60 minutes, exposed onto PhosphorImager screens (GE Healthcare) and developed using a Sapphire Biomolecular Imager (Azure Biosystems).

Quantification of 3'3'-c-di-AMP Using AMP-Glo™ Assay

3'3'-c-di-AMP standards were prepared by performing two-fold serial dilutions in buffer [50 mM Tris-Cl pH = 8.5, 100 mM NaCl]. 3'3'-c-di-AMP samples were supplemented with 0.1 mg mL^{-1}

Bovine Serum Albumin, 1 mM DTT, 0.1 mM $MnCl_2$, and 1 μM CnpB (final concentration) (100 μL total reaction volume). Samples were incubated overnight at 37°C. 24 hours later, 100 μL of AMP-Glo™ reagent I was added to each sample and incubated at room temperature for 2 hours. 50 μL of the resulting sample was transferred to a solid white 96-well plate (BioRad) and then incubated with 50 μL of AMP Detection Solution (equilibrated at room temperature for at least one hour) for one hour at room temperature. Luminescence was quantified using a plate reader (Synergy HTX multimode reader, BioTek Instruments) with an integration time of one second. Relative luminescence units (RLU) for each sample were background corrected by subtracting the RLU of the no 3'3'-c-di-AMP control. Standard curves were generated using default settings in GraphPad Prism software. Quantification and detection limits were calculated as previously described[26].

Quantification of 3'3'-c-di-AMP Using AMP-Luciferase Assay (CDA-Luc)

3'3'-c-di-AMP standards were prepared by performing two-fold serial dilutions in buffer [50 mM Tris-Cl pH = 8.5, 100 mM NaCl]. 3'3'-c-di-AMP samples dissolved in buffer [50 mM Tris-Cl pH = 8.5, 100 mM NaCl] were supplemented with 0.1 mg mL^{-1} Bovine Serum Albumin, 1 mM DTT, 0.1 mM $MnCl_2$, and 1 μM CnpB (final concentration) (100 μL total reaction volume). Samples were incubated overnight at 37°C. 24 hours later, 100 μL of ATP generation solution [50 mM Tris-Cl pH = 8.5, 100 mM NaCl, 2 μM PAP, 50 μg mL^{-1} sodium hexametaphosphate, 2U myokinase, 0.1 mg mL^{-1} Bovine Serum Albumin, 1 mM DTT, 0.1 mM $MgCl_2$] was added to each sample and incubated at room temperature for 3 hours. 50 μL of the resulting sample was transferred to a solid white 96-well plate (BioRad) and then incubated with 50 μL of Kinase Glo® reagent (equilibrated at room temperature for at least one hour). The plates were briefly centrifuged and incubated for at least ten minutes at room temperature. Luminescence was quantified using a plate reader (Synergy HTX multimode reader, BioTek Instruments) with an integration time of one second. Relative luminescence units (RLU) for each sample were background corrected by subtracting the RLU of the no 3'3'-c-di-AMP control. Standard curves were generated using default settings in GraphPad Prism 8 software. Concentrations of 3'3'-c-di-AMP in unknown samples was determined by interpolating into standard curves using GraphPad Prism 8 software. Quantification and detection limits were calculated as previously described[26].

RECON Affinity Purification

Listeria monocytogenes was back diluted into *Listeria* defined media[3,103] at an OD 0.1 and grown for 24 hours shaking at 37°C. The following day, 1 mL of overnight culture was spun at max speed in a microcentrifuge for 1 minute and supernatant and cell pellet were separated and saved for processing. The cell pellet was resuspended in 200 μL ice cold pulldown buffer [100uM Tris pH = 7.5 20mM MgCl2 50mM NaCl] and lysed by sonication for 5 seconds at 25% power. Next, 800 μL of pulldown buffer and 1.3 μM (final concentration) of RECON bound to 20 μL of Ni-NTA beads were added to the sample and agitated for 15 minutes at room temperature to allow binding. The beads were then spun down and washed 3X with pulldown buffer. Subsequently, 150 μL of pulldown buffer with 500mM Imidazole was added to the beads and agitated for 15 minutes at room temperature to release RECON. (Note: We have found that directly boiling the RECON-bead complexes can release interferents that affect downstream quantification. We recommend eluting the RECON-CDA complexes first, followed by boiling to release CDA.) Beads were spun

down at max speed and supernatant added to a clean microcentrifuge tube. The supernatant was heated to 95°C for 10 minutes to denature RECON and release c-di-AMP then spun down at maximum speed to pellet the denatured protein. The supernatant was then processed to determine c-di-AMP concentration using the CDA-Luc protocol, as detailed above. Supernatant samples were processed identically except that 500 µL of supernatant was added to 500 µL of 2X pulldown buffer and 1.3 µM (final concentration) of RECON bound to 20 µL of Ni-NTA beads was used to bind c-di-AMP.

Figures

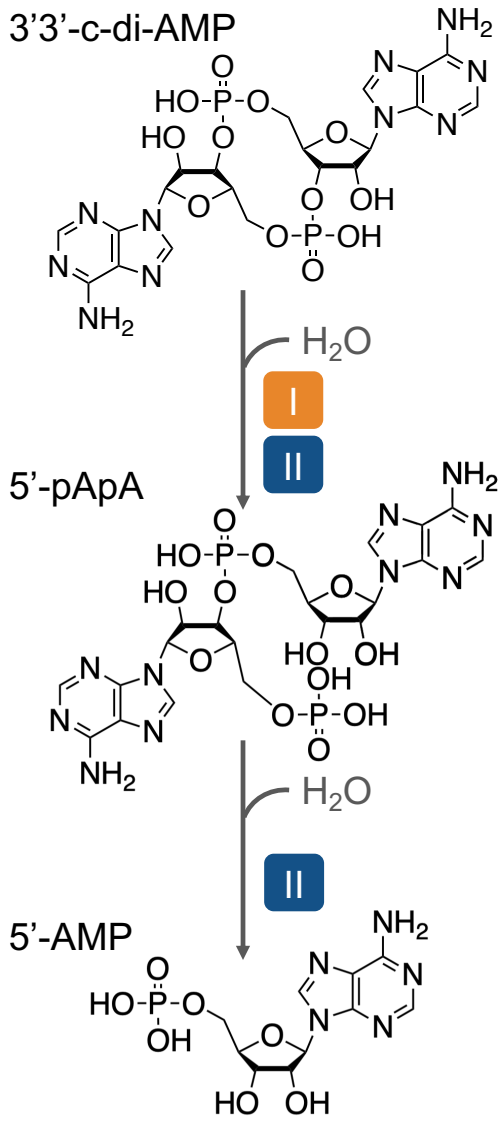

Group I Phosphodiesterases

PdeA – *Listeria monocytogenes*
PgpH – *Listeria monocytogenes*
GdpP – *Bacillus subtilis*
GdpP – *Lactococcus lactis*
GdpP – *Staphylococcus aureus*
GdpP – *Streptococcus pyogenes*
GdpP – *Streptococcus suis*
GdpP – *Lactococcus lactis*
Pde1 – *Streptococcus pneumoniae*
DhhP – *Borrelia burgdorferi*

Group II Phosphodiesterases

Pde2 – *Streptococcus pneumoniae*
CnpB – *Mycobacterium tuberculosis*
PDE – *Mycobacterium smegmatis*
AtaC – *Streptomyces venezuelae*
CdnP – *Streptococcus agalactiae*

Fig. 4.1: Mechanisms of 3’3’-c-di-AMP hydrolysis
Overview of 3’3’-c-di-AMP hydrolysis by phosphodiesterases (PDEs). Group I PDEs hydrolyze 3’3’-c-di-AMP to the linear dinucleotide 5’-pApA. Group II PDEs hydrolyze 3’3’-c-di-AMP to 5’-AMP. Group II PDEs can also hydrolyze 5’-pApA to 5’-AMP.

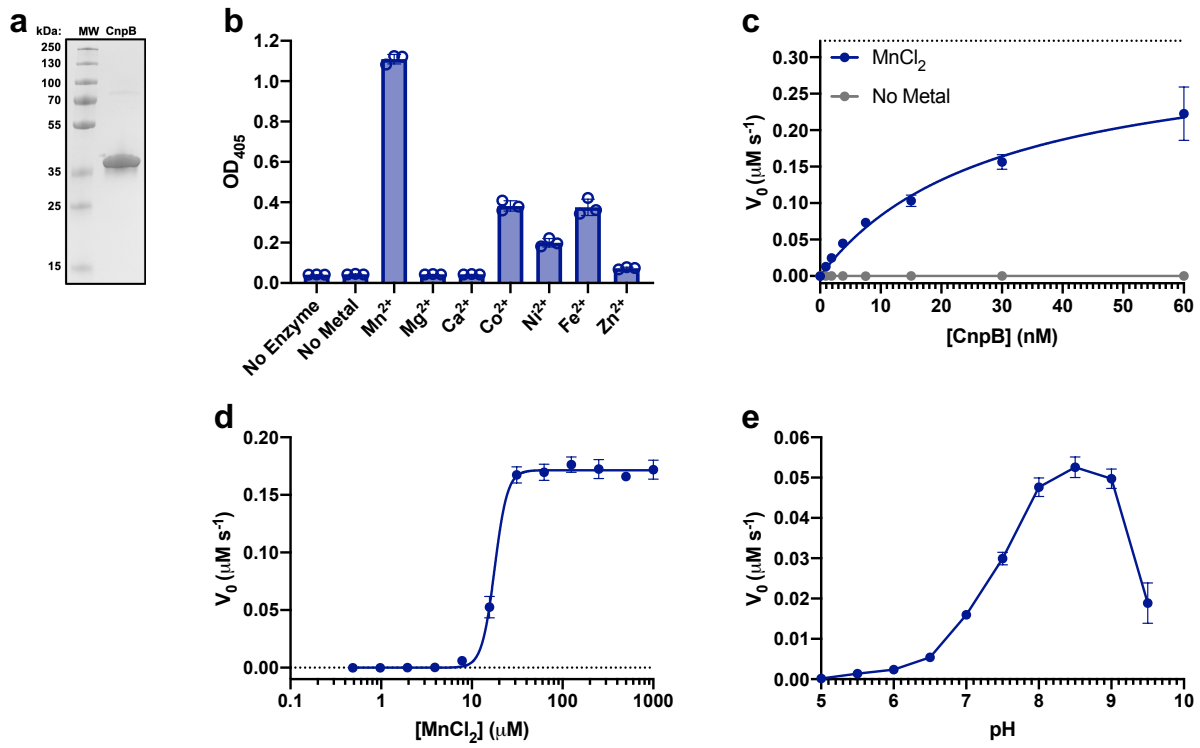

Fig. 4.2: Optimization of CnpB hydrolytic activity

(a) SDS-PAGE analysis of NiNTA purified *M. tuberculosis* CnpB. **(b-e)** BNPP hydrolysis activity of CnpB. (b) 500 nM CnpB was incubated with 0.2 mM BNPP in the presence and absence of 0.1 mM indicated metal ions for 5 minutes at 37°C and absorbance at 405 nm was recorded. **(c)** Increasing concentrations of CnpB were incubated with 0.2 mM BNPP in the presence and absence of 0.1 mM $MnCl_2$ at 37°C and absorbance at 405 nm was monitored. **(d)** 15 nM CnpB was incubated with 0.2 mM BNPP and increasing concentrations of $MnCl_2$ at at 37°C and absorbance at 405 nM was monitored. **(e)** 15 nM CnpB was incubated with 0.2 mM BNPP and 0.1 mM $MnCl_2$ in pH 5-9.5 reaction buffer at 37°C and absorbance at 405 nm was monitored. In all panels, data are presented as mean ± standard deviation of n=3 replicates.

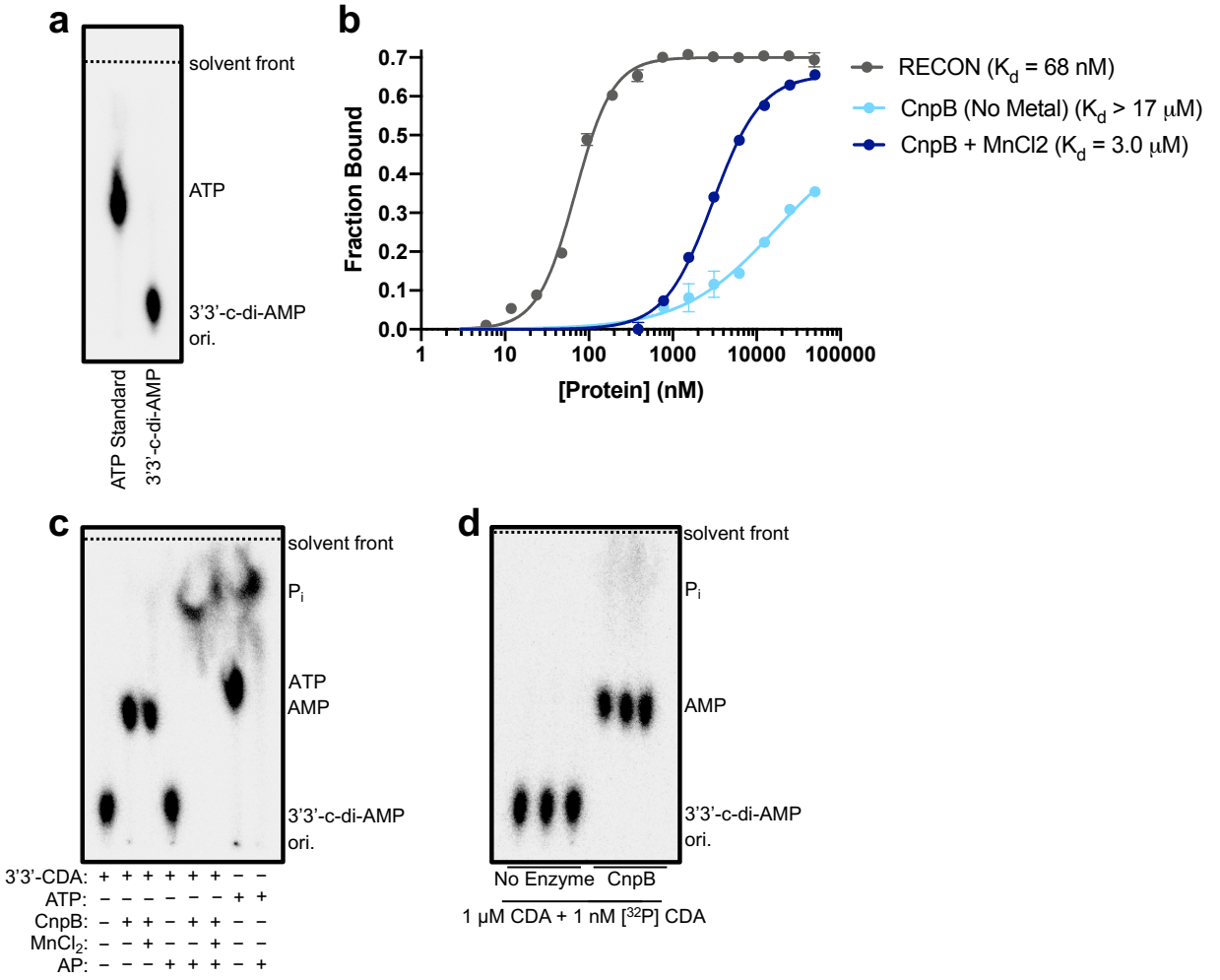

Fig. 4.3: Analysis of CnpB 3'3'-c-di-AMP binding and hydrolysis

(a) Thin layer chromatography (TLC) analysis of enzymatically synthesized [^{32}P] 3'3'-c-di-AMP and [^{32}P] ATP standard. Data are representative of several independent experiments. **(b)** DRaCALA analysis of 3'3'-c-di-AMP binding to RECON and CnpB in presence and absence of 0.1 mM $MnCl_2$. data are presented as mean ± standard deviation of n=3 replicates. (c-d) TLC analysis of 3'3'-c-di-AMP hydrolysis by CnpB. **(c)** ~1 nM [^{32}P] 3'3'-c-di-AMP was incubated with or without 25 μM CnpB in the presence and absence of 0.1 mM $MnCl_2$ for 2 hours at 37°C. Samples were then treated with or without 0.1 U of Alkaline Phosphatase for 1 hour. Samples were then spotted onto TLC plates and separated. Data are representative of n=3 experiments. **(d)** 1 μM unlabeled 3'3'-c-di-AMP spiked with ~1 nM [^{32}P] 3'3'-c-di-AMP was treated with or without 1 μM CnpB overnight at 37°C. Samples were then spotted onto TLC plates and separated. N=3 replicates are shown.

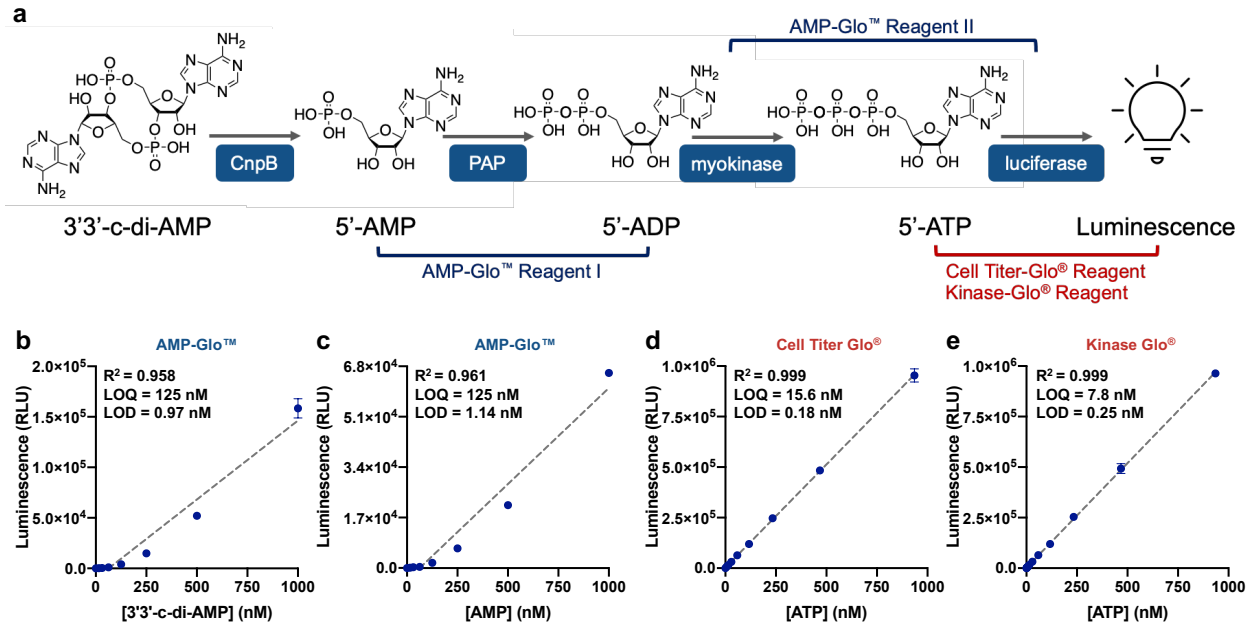

Fig. 4.4: Detection of 3'3'-c-di-AMP using conventional AMP-Glo assay

(a) Schematic overview of AMP and ATP detection methods. **(b)** Standard curve of CnpB hydrolyzed 3'3'-c-di-AMP using AMP-Glo™ assay. **(c)** Standard curve of AMP using AMP-Glo™ assay. **(d)** Standard curve of ATP using Cell Titer Glo® reagent. **(e)** Standard curve of ATP using Kinase Glo® reagent. In all panels, data are presented as mean ± standard deviation of n=3 replicates.

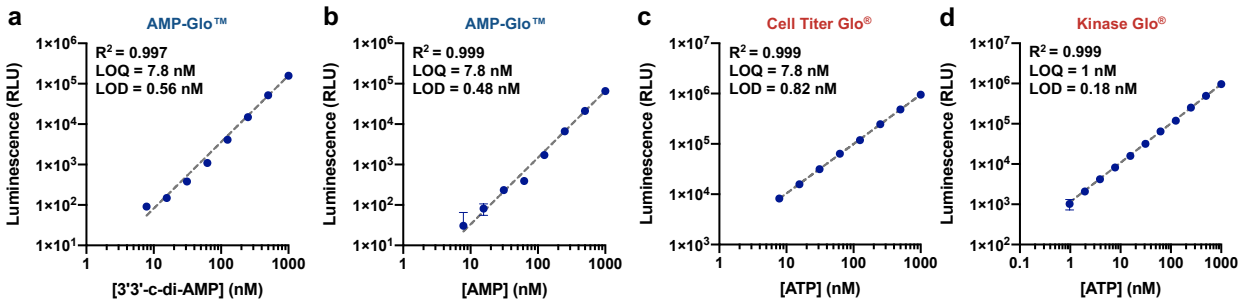

Fig. 4.5: Reanalysis of AMP and ATP detection methods

Data from Figure 4.4 b-e were reanalyzed using log-log plots. **(a)** Standard curve of CnpB hydrolyzed 3'3'-c-di-AMP using AMP-Glo™ assay. **(b)** Standard curve of AMP using AMP-Glo™ assay. **(c)** Standard curve of ATP using Cell Titer Glo® reagent. **(d)** Standard curve of ATP using Kinase Glo® reagent. In all panels, data are presented as mean ± standard deviation of n=3 replicates.

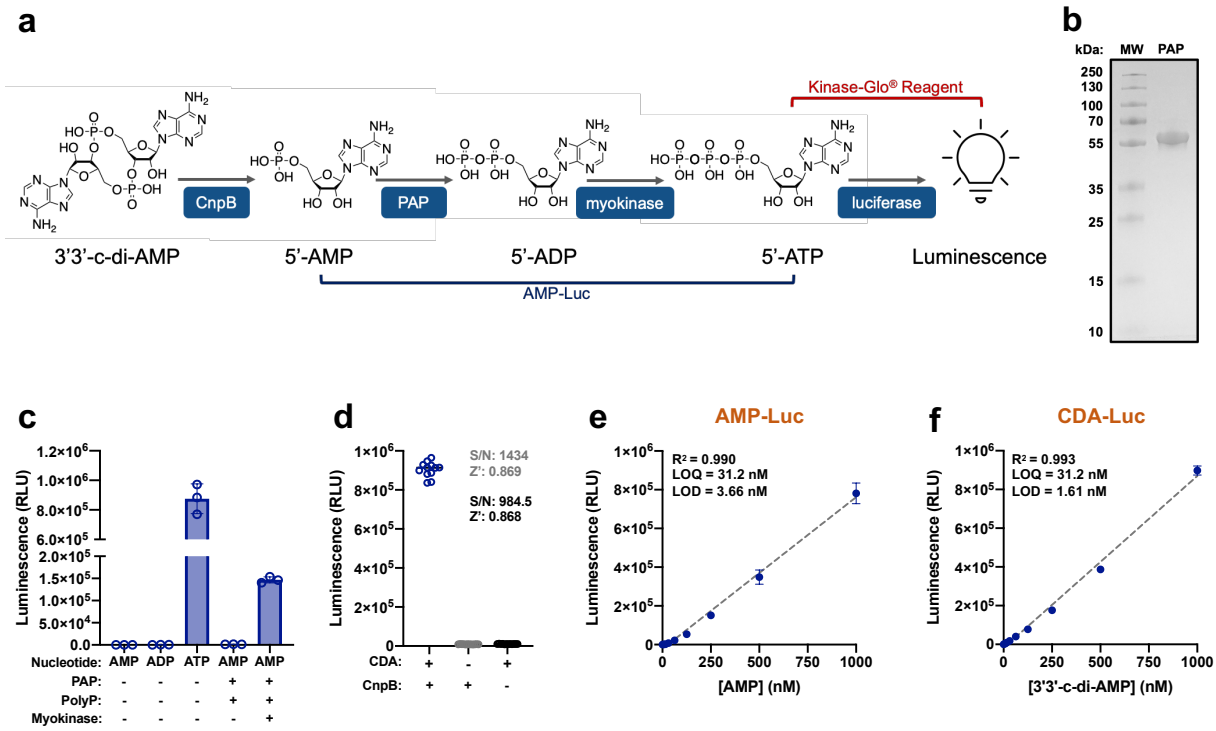

Fig. 4.6: Quantification of 3'3'-c-di-AMP using CDA-Luc Assay

(a) Schematic overview of CDA-Luc assay. **(b)** SDS-PAGE analysis of NiNTA purified *A. johnsonii* PAP. **(c)** Optimization of AMP-Luc assay. AMP was incubated with 2 µM PAP and 50 µg mL^{-1} of sodium hexametaphosphate (PolyP) with or without 1U myokinase for 3 hours followed by incubated with Kinase Glo® reagent for 10 minutes. **(d)** Z' factor analysis of CDA-Luc Assay. 1 µM 3'3'-c-di-AMP was treated with or without CnpB overnight and AMP was detected using AMP-Luc assay. **(e)** Standard curve of AMP using AMP-Luc assay. **(f)** Standard curve of CnpB hydrolyzed 3'3'-c-di-AMP using AMP-Luc assay. In all panels, data are presented as mean ± standard deviation of n=3 (c, e-f) or n=12 (d) replicates.

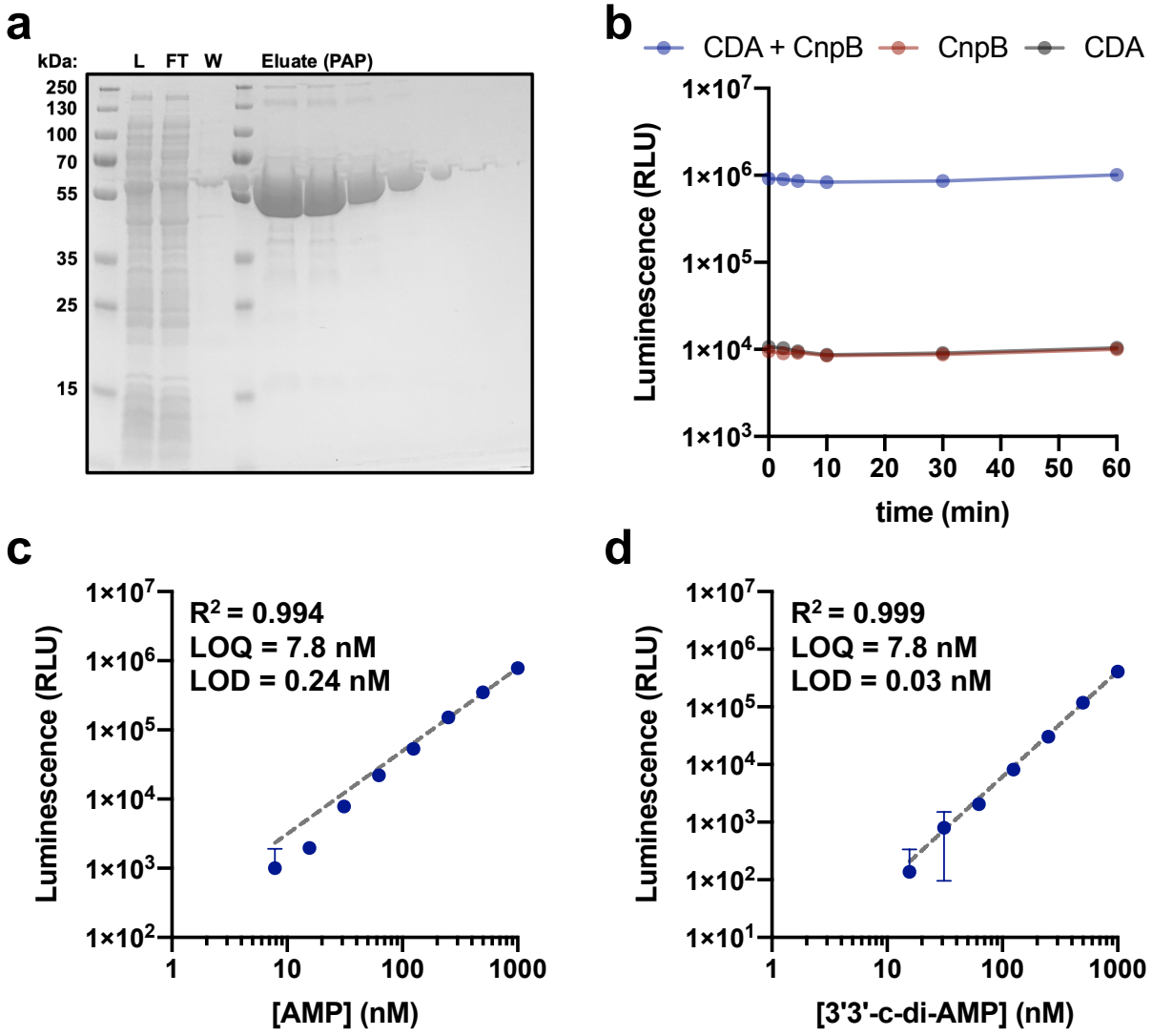

Fig. 4.7: Development of CDA-Luc assay

(a) SDS-PAGE analysis of NiNTA purified PAP. L = lysate; FT = flow through; W = wash. Samples were pooled, desalted, and reanalyzed by SDS-PAGE on the right. **(b)** Stability of CDA-Luc Assay. 1 µM 3'3'-c-di-AMP was treated with or without CnpB overnight and AMP was detected using AMP-Luc assay. Luminescence was monitored over one hour. **(c-d)** Reanalysis of AMP-Luc assay using log-log plot. (c) Standard curve of AMP using AMP-Luc assay. (d) Standard curve of CnpB hydrolyzed 3'3'-c-di-AMP using AMP-Luc assay. In all panels, data are presented as mean ± standard deviation of n =12 (b) or n=3 (c-d) replicates.

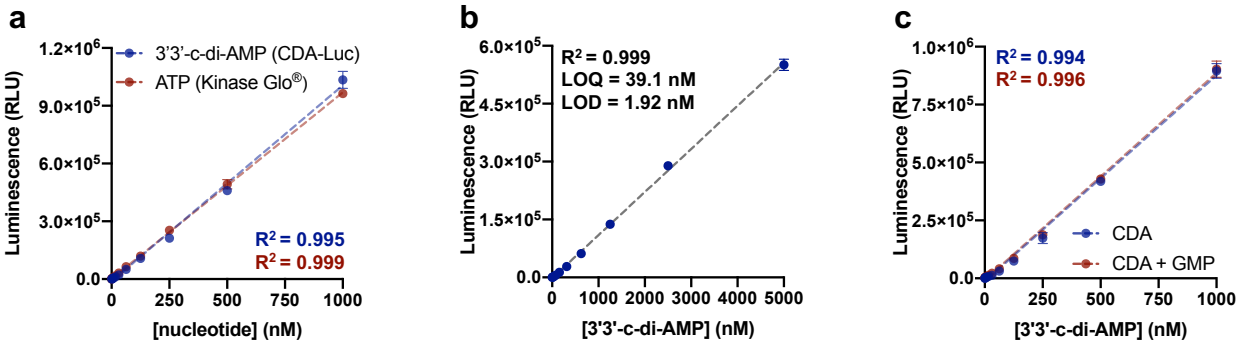

Fig. 4.8: Characterization of CDA-Luc Assay

(a) Overlay of 3'3'-c-di-AMP standard curve generated using AMP-Luc and ATP standard curve generated using Kinase-Glo®. Limit of quantification for 3'3'-c-di-AMP is 31.2 nM and ATP is 7.8 nM. **(b)** Extended standard curve of CDA-Luc assay. **(c)** CDA-Luc standard curve in the presence and absence of 1 µM GMP. In all panels, data are presented as mean ± standard deviation of n=3 replicates.

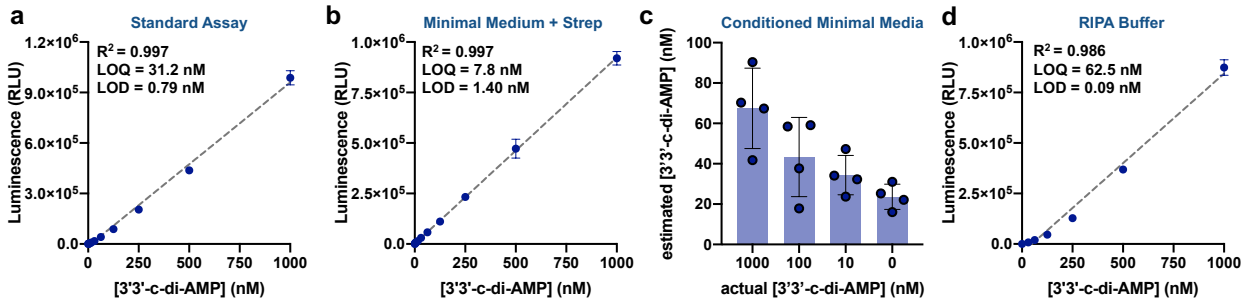

Fig. 4.9: Performance of CDA-Luc in different buffers

(a) CDA-Luc standard curve using standard assay conditions. **(b)** CDA-Luc standard curve in *Listeria monocytogenes* minimal media supplemented with streptomycin. **(c)** Conditioned minimal media derived from Δ*dacA*Δ*oppA L. monocytogenes* was doped with known concentrations of pure 3'3'-c-di-AMP and subjected to CDA-Luc analysis. **(d)** CDA-Luc standard curve in RIPA buffer. In all panels, data are presented as mean ± standard deviation of n=3 (a, b, and d) or n=4 (c) replicates.

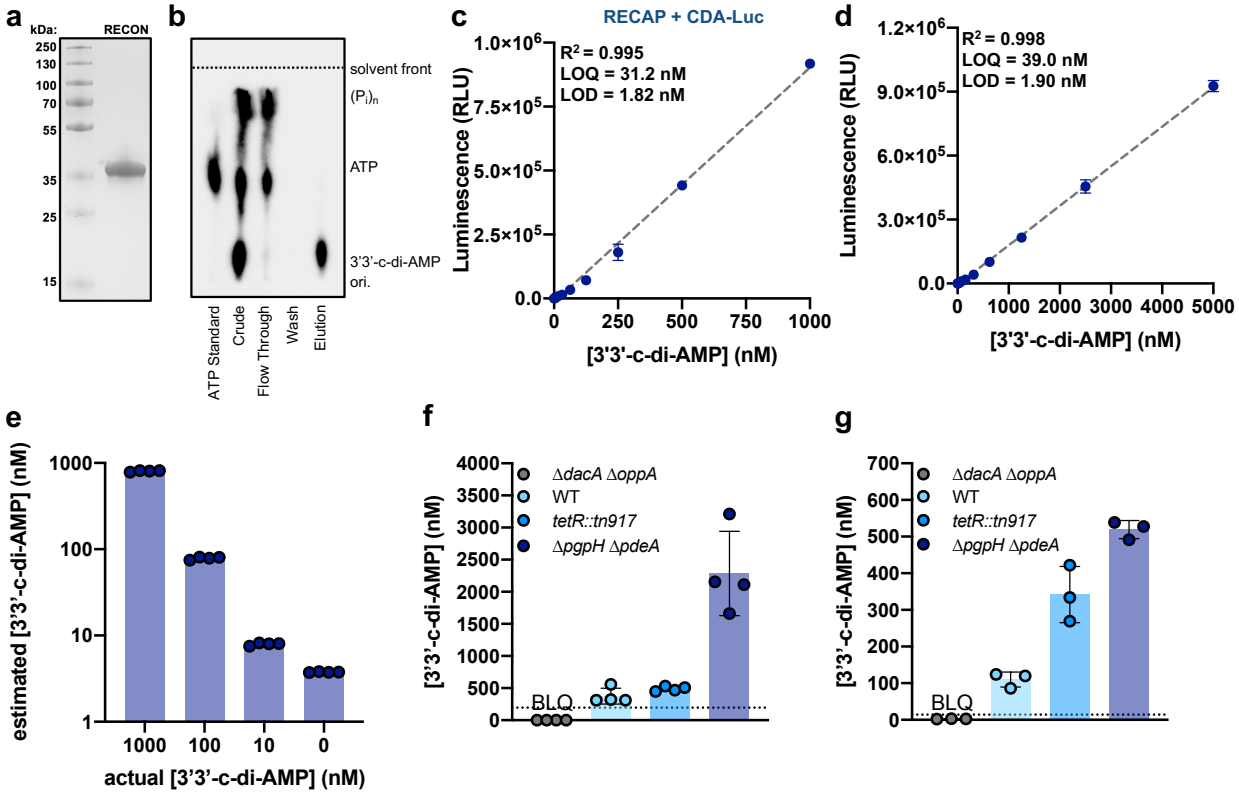

Fig. 4.10: RECON enables affinity purification of c-di-AMP from biological samples
(a) SDS-PAGE analysis of NiNTA purified murine RECON. **(b)** TLC analysis of 3'3'-c-di-AMP using RECON affinity purification. **(c)** CDA-Luc standard curve of 3'3'-c-di-AMP affinity purified using 2 µM RECON. Data are presented as mean ± standard deviation of n=3 replicates. **(d)** CDA-Luc standard curve of 3'3'-c-di-AMP affinity purified from *L. monocytogenes* minimal media using 10 µM RECON. Data are presented as mean ± standard deviation of n=3 replicates. **(e)** Conditioned minimal media derived from Δ*dacA*Δ*oppA L. monocytogenes* was doped with known concentrations of pure 3'3'-c-di-AMP and subjected to RECAP prior to CDA-Luc analysis. Limit of quantification was determined to be 7.8 nM. Data are presented as mean ± standard deviation of n=4 replicates. **(f)** Quantification of intracellular 3'3'-c-di-AMP from lysates of various *L. monocytogenes* strains using RECON affinity purification and CDA-Luc. Dashed lines indicate the limit of quantification (BLQ denotes below the limit of quantification). Data are presented as mean ± standard deviation of n=4 replicates. **(g)** Quantification of secreted 3'3'-c-di-AMP from the growth medium of various *L. monocytogenes* strains using RECON affinity purification and CDA-Luc. Dashed lines indicate the limit of quantification (BLQ denotes below the limit of quantification). Data are presented as mean ± standard deviation of n=3 replicates.

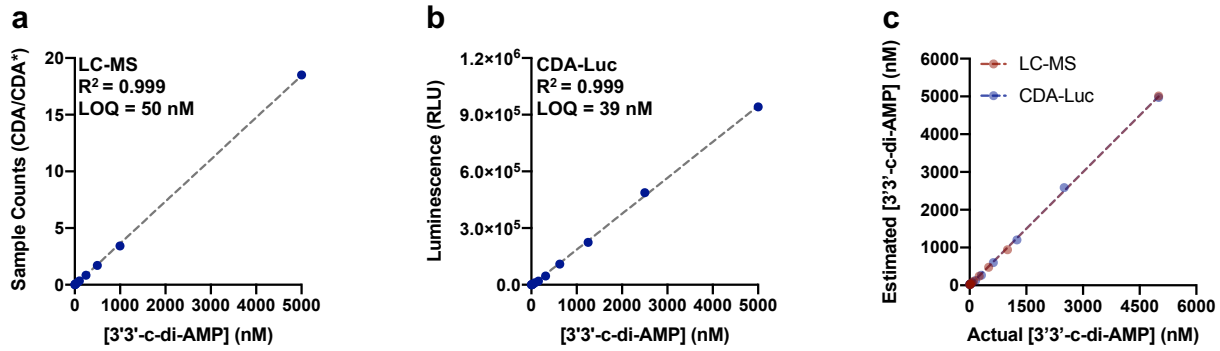

Fig. 4.11: Comparison of CDA-Luc to Mass Spectrometry (LC-MS)
(a) LC-MS standard curve of 3'3'-c-di-AMP. Known concentrations of c-di-AMP were mixed with 500 nM of (C^{13} N^{15}) isotopically labeled c-di-AMP (CDA*) and subjected to LC-MS analysis. One representative standard curve of n=1 replicates is shown. **(b)** CDA-Luc standard curve of 3'3'-c-di-AMP. Data are presented as mean ± standard deviation of n=3 replicates. **(c)** Plot of estimated [3'3'-c-di-AMP] by interpolation into the standard curve vs the actual concentration for LC-MS from (a) and CDA-Luc from (b).

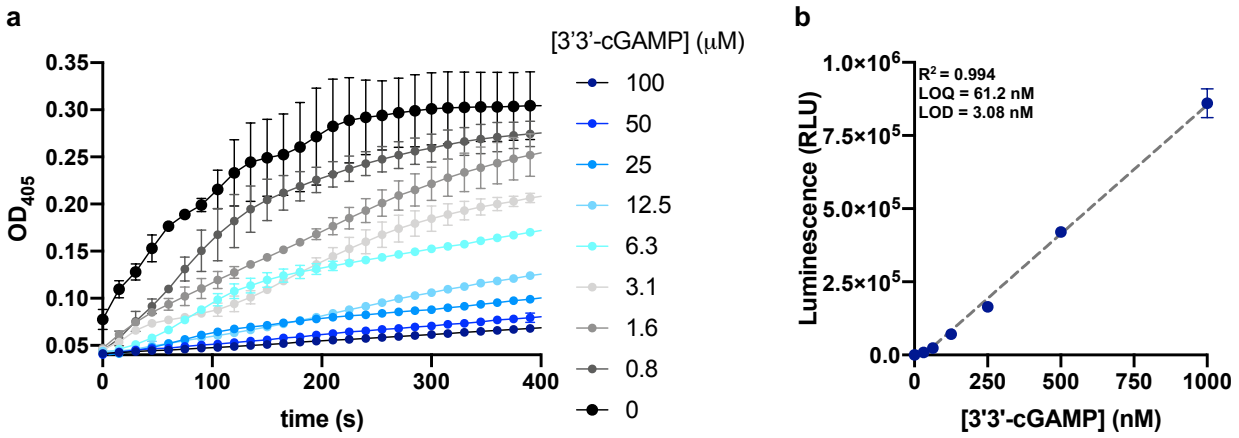

Fig. 4.12: Quantification of 3'3'-cGAMP using CDA-Luc

(a) 15 nM CnpB was incubated with 0.1 mM BNPP and 0.1 mM $MnCl_2$ in pH 8.5 reaction buffer in the presence of increasing concentrations of 3'3'-cGAMP and absorbance at 405 nm was monitored. Data are presented as mean ± standard deviation of n=2 replicates. **(b)** Standard curve of CnpB hydrolyzed 3'3'-cGAMP using AMP-Luc assay. Data are presented as mean ± standard deviation of n=3 replicates.

Chapter 5

Conclusions and future directions

SUMMARY OF FINDINGS

Over the last decade, cyclic dinucleotides have emerged as ubiquitous second messengers among both prokaryotes and eukaryotes[7,75]. CDN signaling systems originated in prokaryotes where they regulate a myriad of physiological processes including central metabolism, cell wall homeostasis, osmoregulation, biofilm formation, motility, virulence and anti-phage immunity. These diverse functions are mediated by a suite of cyclases that synthesize a variety of different cyclic di- and oligo- nucleotide species that in turn regulate the activity of distinct effector proteins that collectively coordinate a shift in cellular function. In prokaryotes, the cGAS/DncV family of nucleotidyl transferases synthesize cyclic oligonucleotides in response to bacteriophage infection[6,9]. These second messengers bind to sensor domains on their cognate receptors resulting in activation of the effector domain, which trigger cell death programs through a variety of mechanisms including membrane disruption, DNA degradation, hydrolysis of cellular cofactors, among others[6,9,17,26]. One such sensor domain, STING, is found fused to NAD^+ hydrolyzing TIR or transmembrane domains[26]. In all of these CBASS operons, the CD-NTases synthesize 3'3'-c-di-GMP which binds to the STING-scaffold domain resulting in its oligomerization and activation of the TIR domain[26]. Over time, these prokaryotic cGAS-STING signaling systems were domesticated by metazoans to defend against microbial infection. Metazoan cGAS was outfitted with DNA sensing capabilities and STING activity was modified to enable induction of autophagy and innate immune gene expression.

In the context of pathogen infection, foreign and damaged self-DNA species are sensed by cGAS resulting in the formation of phase separated compartments for the rapid synthesis of the second messenger 2'3'-cGAMP[29,30]. Binding of cGAMP to STING results in its oligomerization and translocation to the perinuclear Golgi where it recruits the kinase TBK1 to the transcription factor IRF3 in order to activate innate immune gene programs to restrict pathogen replication and spread[4,5,22,23,33,34]. Chromosomal instability, nuclear rupture, and mitochondrial damage which occur in the context of tumorigenesis, tissue damage or injury, and various acquired or genetic autoinflammatory diseases also produce ligands that activate the cGAS-STING pathway[65,67,68]. In some instances these sterile inflammatory responses can be beneficial allowing for the removal of the damaged cell(s) and maintenance of tissue homeostasis; however, misregulation of these pathways have been implicated in the pathogenesis of autoinflammatory diseases including Aicardi-Goutieres syndrome and Systemic Lupus Erythematosus among others[54,68].

Because of their essential role in modulating innate immune signaling, there has been incredible interest in designing novel therapeutics that modulate the activity of cGAS and STING. Purified cyclic dinucleotides administered intratumorally instigate potent tumor regression in mouse models; however, as these molecules contain labile phosphodiesterase linkages they are rapidly cleaved by nucleases and have short half-lives in vivo[44,50,73]. Thus, the first generation of STING agonists have leveraged phosphorothioate bonds to yield non-hydrolysable, synthetic cyclic dinucleotide analogs[50,73]. These molecules are currently in investigation as immune adjuvants in combination with PD-1 blockade for the treatment of melanoma and various blood cancers[44,45].

Despite several independent reports of the antitumor properties of exogenous cyclic dinucleotides, prior to my thesis work, it was not understood how cyclic dinucleotides could traverse the lipid bilayer. Previous work in our laboratory had suggested that this process was carrier mediated, but

it became readily apparent that an unbiased genetic screen would be required to uncover the transport mechanism. Thus, we leveraged the latest advances in CRISPR-interference technology to perform an unbiased, genome-wide screen to identify host proteins required for extracellular CDN mediated immune responses in the human monocytic cell line, THP-1. This screen identified the reduced folate carrier, SLC19A1, as a critical protein required for extracellular but not endogenous CDN-mediated IFN-I activation. In addition to transporting folates, SLC19A1 can transport other molecules including thiamine pyrophosphate and various nucleotide species[78]. Using a combination of genetic and biochemical approaches, we found that SLC19A1 can also moonlight as a CDN transporter in some human immune cell types.

Interestingly, SLC19A1 was dispensable for cGAMP mediated IFN-I activation in all of the murine cell lines that we tested. It is possible that there might be a more dominant cGAMP transporter in murine cells that compensates for the loss of SLC19A1. Alternatively, mSLC19A1 may be incapable of transporting cyclic dinucleotides. There is high homology between human and mouse SLC19A1 at the amino acid level within the transport region. Thus, specific residues involved in cGAMP recognition by SLC19A1 may have been lost in mice; alternatively, a cofactor, absent in murine cells, may be required for efficient transport of cyclic dinucleotides. We did not identify a candidate cofactor in our screen, but it could be essential precluding its identification using our screening strategy. Nevertheless, identification of SLC19A1 as the first cyclic dinucleotide transporter may have important implications for cancer immunotherapy and the pathogenesis of autoinflammatory and infectious diseases.

In order to identify SLC19A1, we utilized a fluorescence reporter of type I interferon activation. Here, the minimal mouse interferon promoter and 5xInterferon-Sensitive Response Element (ISRE) drives the expression of the fluorescent protein tdTomato. Such reporter assays have often been used to monitor the activity of PRR signaling systems. Unfortunately, these systems require several hours for fluorescent proteins to accumulate to sufficient levels to be monitored by microscopy or flow cytometry, precluding their utility for the investigation of PRR signaling kinetics and dynamics. In addition, multiple PRR signaling systems converge at the level of IRF3 and type I interferon making these reporter assays relatively non-specific. Thus, there was a significant need in the field for a sensitive, specific, reversible, and genetically encodable sensor for 2’3’-cGAMP. To fill this need, we engineered a Förster resonance energy transfer (FRET) based biosensor (BioSTING) using murine STING as a scaffold. As an in vitro tool, we demonstrated that BioSTING affords real-time detection of CDN synthase activity and inhibition. Moreover, we demonstrated the utility of recombinant BioSTING as a quantitative tool to measure 2’3’-cGAMP levels from mammalian cell extracts. Indeed, expression of BioSTING in live human cells allowed quantification of bacterial and eukaryotic CDN levels with low nanomolar sensitivity. Finally, we utilize targeting signals to generate BioSTING sensors that localize to distinct cellular compartments, enabling investigation of not only the temporal but also the spatial dynamics of cGAMP signaling. Thus, BioSTING is a versatile tool that will likely enable previously intractable questions in the field of cGAMP signaling over the next several years.

Finally, one of the major area of investigations in our laboratory is understanding the role of cyclic di-AMP signaling in *L. monocytogenes* physiology and pathogenesis. Despite a decade of research in cyclic di-AMP signaling in bacteria, the cellular and environmental factors that influence c-di-AMP flux are poorly understood. This is, in part, due to a lack of methods to sensitively and rapidly

quantify c-di-AMP. To that end, we established a luminescence-based coupled enzyme assay that could easily be employed by general microbiology labs to quantify c-di-AMP. We coupled the c-di-AMP phosphodiesterase, CnpB, with the previously described AMP-Luciferase assay to yield an assay that can quantify c-di-AMP over four orders of magnitude with sensitivity comparable to the current gold-standard LC-MS. We also took advantage of the ability of CnpB to hydrolyze 3'3'-cGAMP to quantitate this cyclic dinucleotide using CDA-Luc. We anticipate that this assay will enable unbiased genetic and chemical screens to identify modulators of c-di-AMP and CBASS activity over the coming years.

FUTURE DIRECTIONS

Since our initial discovery of the cGAMP transport activities of SLC19A1, several addition mammalian CDN transporters have been identified using genetic or chemical screens. Using a genome-wide CRISPR knockout screen in *SLC19A1*-deficicent human monocytes, Lahey and colleagues identified the volume regulated anion channel (LRRC8A) as a cGAMP importer and exporter with particular importance in human endothelial cells[48]. These results were corroborated by Zhou and colleagues who utilized a chemical screen to identify the cGAMP transport activities of LRRC8A in a number of murine cells[47]. In order to function as a transporter, LRRC8A must dimerize with another LRRC8 family resulting in the formation of heterodimers with distinct transport activities. Zhou *et. al.* found that LRRC8A:E complexes are involved in cGAMP transport in murine cells; while, Lahey *et. al*. found that LRRC8A:C complexes are required in human vasculature cells. Additionally, a role for the ATP-regulated P2X7R transporter in extracellular cGAMP responses was also recently demonstrated in some murine cell types[49]. Thus, a thorough characterization of which cell types utilize each transporter will be of great interest moving forward.

It is likely that numerous other transporters for cyclic dinucleotides exist. While cyclic dinucleotide importers can readily be identified using chemical or genetic screens using interferon activation or cell death as a read out, identification of cGAMP exporters will be much more difficult[45–48]. Targeted approaches may be required to screen through specific classes of transporters to identify candidate export proteins using LC-MS, EIA, or cGAMP-Luc based measurements. Going forward, it will also be of importance to clarify the role of cGAMP export during various physiological and disease states. Because the dominant cGAMP hydrolase, ENPP1, is predominantly an extracellular protein, export likely plays a role in the resolution of cGAMP signaling; however, cGAMP export has also been shown to stimulate paracrine STING activation in bystander cells during viral infection[47]. Indeed, examination of the role of cGAMP transporters in the context of pathogen infection, autoimmune diseases, and antitumor immunity will likely be a major area of investigation over the coming years. Along those lines, regulation of import and export activity through post-translation modifications of transporters may be of interest. Identification of regulators of cGAMP transport may yield additional targets for the design of novel immunomodulatory therapeutics.

In prokaryotes, the effects of cyclic dinucleotides are often mediated by many distinct receptors that collectively coordinate a major shift in cellular function. Just as there are multiple cGAMP transport proteins in mammals, there may also be additional cGAMP receptor proteins in metazoans besides STING. In support of this idea, several examples of cGAS-dependent, STING-

independent immune responses can be found throughout the literature[59,134]. To that end, our laboratory has employed a chemical proteomics approach to identify additional cGAMP regulated proteins in eukaryotes. It may also be fruitful to probe the evolutionary 'fossil record' to identify additional metazoan homologs of bacterial CBASS effectors. Proteins identified from this approach could be novel cGAMP-regulated proteins or they could respond to different cyclic di- or oligo-nucleotide species. Indeed, in addition to cGAS-STING, the OAS-RNaseL signaling system also likely directly originated from prokaryotic CBASS systems[6,13,17,26]. Intriguingly, several cGAS-like paralogs have been identified in human and mouse genomes[163]. It is unclear if these proteins have enzymatic activity and, if so, what regulates their activity. This will likely be an interesting avenue of research over the coming years.

In metazoans, cGAS is the dominant dsDNA sensor in most cell types. The existence of PRRs that survey the cell for aberrant dsDNA species has been perplexing because these activities need to be tightly regulated to prevent autoreactivity. The simplest model for self-tolerance is segregation of cGAS from cellular DNA sources. In this model, cellular DNAs are compartmentalized in nuclei and mitochondria where they are sheltered from the activity of cGAS and other DNA sensors that are sequestered in the cytosol. While this model is elegant, it cannot account for self-tolerance during cell division during which the nuclear envelope is broken down exposing chromatin to cytosolic DNA sensors. Thus, there has been considerable interest in investigating the localization of cGAS during healthy and diseased states[64–68]. Recent studies have shown that cGAS is predominantly localized to the nucleus in most cell types[68]. Interestingly, in the nuclear compartment, cGAS was found tightly tethered to DNA yet paradoxically held in an inactive conformation[68]. Several follow-up studies using Cryo-EM have shown that cGAS is tightly anchored to the acidic patch of nucleosomes locking cGAS in an inactive confirmation[164–167]. Thus, it is likely that nuclear cGAS is titrated away from self-dsDNA through nucleosome-mediated sequestration.

Given the tight regulation of cGAS activity, it will be interesting to examine the temporal and spatial kinetics and dynamics of nuclear cGAS activation during various disease states including genotoxic stress and radiation injury using BioSTING FRET responses as a readout. Interestingly, most DNA viruses complete their replication cycle in the nucleus[62]. It has been speculated that nuclear replication shields the viral genomes from cytosolic DNA sensors[62]. Thus, nuclear localization of cGAS may have been an adaptation to monitor this cellular compartment for foreign DNA species. It will be interesting to determine if nuclear cGAS retains the ability to sense viral dsDNA species and how this process is regulated. Alternatively, DNA virus infection may be sensed by cytoplasmic pools of cGAS that respond to cytosolic dsDNA arising from defective packaging of virions or mitochondrial damage during viral infection. Our nuclear and cytoplasmic BioSTING sensors may be useful for future studies aimed at elucidating the temporal and spatial dynamics of cGAMP signaling during viral infection.

Finally, just as there are still many open-ended questions in metazoan cyclic dinucleotide signaling, there is still much left to uncover in the field of bacterial cyclic dinucleotide signaling. In particular, identification of the cellular and environmental factors that govern c-di-AMP dynamics will be of fundamental importance over the coming years. As c-di-AMP is the only essential cyclic dinucleotide in bacteria, a thorough understanding of the features that drive its essentiality and toxicity will be of importance for the design of novel therapeutics to combat

bacterial infections. Moreover, while it is clear that metazoan cGAS is dsDNA sensor, the factors that trigger activation of bacterial CD-NTases remain unclear. Identifying the features of bacteriophage infection that drive CD-NTase activation will be of tantamount importance for the understanding of cyclic oligonucleotide based signaling systems. High throughput drug screens to find agonists of CD-NTase activity independent of bacteriophage infection may be fruitful for the design of novel therapeutics to combat bacterial infection including infection with *V. cholerae* species. In closing, the field of cyclic dinucleotide signaling is still in its infancy with many important discoveries yet to be made.

Literature Cited

1. Janeway, C. A. & Medzhitov, R. Innate Immune Recognition. *Annu. Rev. Immunol.* **20**, 197–216 (2002).

2. McWhirter, S. M. *et al.* A host type I interferon response is induced by cytosolic sensing of the bacterial second messenger cyclic-di-GMP. *J. Exp. Med.* **206**, 1899–1911 (2009).

3. Woodward, J. J., Iavarone, A. T. & Portnoy, D. A. c-di-AMP Secreted by Intracellular Listeria monocytogenes Activates a Host Type I Interferon Response. *Science* **328**, 1703 (2010).

4. Sun, L., Wu, J., Du, F., Chen, X. & Chen, Z. J. Cyclic GMP-AMP Synthase Is a Cytosolic DNA Sensor That Activates the Type I Interferon Pathway. *Science* **339**, 786 (2013).

5. Wu, J. *et al.* Cyclic GMP-AMP Is an Endogenous Second Messenger in Innate Immune Signaling by Cytosolic DNA. *Science* **339**, 826 (2013).

6. Cohen, D. *et al.* Cyclic GMP–AMP signalling protects bacteria against viral infection. *Nature* (2019) doi:10.1038/s41586-019-1605-5.

7. Krasteva, P. V. & Sondermann, H. Versatile modes of cellular regulation via cyclic dinucleotides. *Nat. Chem. Biol.* **13**, 350 (2017).

8. Davies, B. W., Bogard, R. W., Young, T. S. & Mekalanos, J. J. Coordinated Regulation of Accessory Genetic Elements Produces Cyclic Di-Nucleotides for V. cholerae Virulence. *Cell* **149**, 358–370 (2012).

9. Whiteley, A. T. *et al.* Bacterial cGAS-like enzymes synthesize diverse nucleotide signals. *Nature* **567**, 194–199 (2019).

10. Ablasser, A. *et al.* cGAS produces a 2′-5′-linked cyclic dinucleotide second messenger that activates STING. *Nature* **498**, 380 (2013).

11. Zhang, X. *et al.* Cyclic GMP-AMP Containing Mixed Phosphodiester Linkages Is An Endogenous High-Affinity Ligand for STING. *Mol. Cell* **51**, 226–235 (2013).

12. Diner, E. J. *et al.* The Innate Immune DNA Sensor cGAS Produces a Noncanonical Cyclic Dinucleotide that Activates Human STING. *Cell Rep.* **3**, 1355–1361 (2013).

13. Burroughs, A. M., Zhang, D., Schäffer, D. E., Iyer, L. M. & Aravind, L. Comparative genomic analyses reveal a vast, novel network of nucleotide-centric systems in biological conflicts, immunity and signaling. *Nucleic Acids Res.* **43**, 10633–10654 (2015).

14. Kranzusch, P. J. *et al.* Ancient Origin of cGAS-STING Reveals Mechanism of Universal 2′,3′ cGAMP Signaling. *Mol. Cell* **59**, 891–903 (2015).

15. Wang, C. *et al.* Synthesis of All Possible Canonical (3′–5′-Linked) Cyclic Dinucleotides and Evaluation of Riboswitch Interactions and Immune-Stimulatory Effects. *J. Am. Chem. Soc.* **139**, 16154–16160 (2017).

16. Nelson, J. W. & Breaker, R. R. The lost language of the RNA World. *Sci. Signal.* **10**, eaam8812 (2017).

17. Lowey, B. *et al.* CBASS Immunity Uses CARF-Related Effectors to Sense 3′–5′- and 2′–5′-Linked Cyclic Oligonucleotide Signals and Protect Bacteria from Phage Infection. *Cell* **182**, 38-49.e17 (2020).

18. Ye, Q. *et al.* HORMA Domain Proteins and a Trip13-like ATPase Regulate Bacterial cGAS-like Enzymes to Mediate Bacteriophage Immunity. *Mol. Cell* **77**, 709-722.e7 (2020).

19. Gao, J. *et al.* Identification and characterization of phosphodiesterases that specifically degrade 3′3′-cyclic GMP-AMP. *Cell Res.* **25**, 539–550 (2015).

20. Severin, G. B. *et al.* Direct activation of a phospholipase by cyclic GMP-AMP in El Tor Vibrio cholerae. *Proceedings of the National Academy of Sciences* **115**, E6048 (2018).

21. Lau, R. K. *et al.* Structure and Mechanism of a Cyclic Trinucleotide-Activated Bacterial Endonuclease Mediating Bacteriophage Immunity. *Mol. Cell* **77**, 723-733.e6 (2020).

22. Ishikawa, H. & Barber, G. N. STING is an endoplasmic reticulum adaptor that facilitates innate immune signalling. *Nature* **455**, 674–678 (2008).

23. Ishikawa, H., Ma, Z. & Barber, G. N. STING regulates intracellular DNA-mediated, type I interferon-dependent innate immunity. *Nature* **461**, 788–792 (2009).

24. Burdette, D. L. *et al.* STING is a direct innate immune sensor of cyclic di-GMP. *Nature* **478**, 515–518 (2011).

25. Wan, L. *et al.* TIR domains of plant immune receptors are NAD^+-cleaving enzymes that promote cell death. *Science* **365**, 799–803 (2019).

26. Morehouse, B. R. *et al.* STING cyclic dinucleotide sensing originated in bacteria. *Nature* (2020) doi:10.1038/s41586-020-2719-5.

27. Zhang, X. *et al.* The Cytosolic DNA Sensor cGAS Forms an Oligomeric Complex with DNA and Undergoes Switch-like Conformational Changes in the Activation Loop. *Cell Rep.* **6**, 421–430 (2014).

28. Andreeva, L. *et al.* cGAS senses long and HMGB/TFAM-bound U-turn DNA by forming protein–DNA ladders. *Nature* **549**, 394–398 (2017).

29. Du, M. & Chen, Z. J. DNA-induced liquid phase condensation of cGAS activates innate immune signaling. *Science* **361**, 704 (2018).

30. Xie, W. *et al.* Human cGAS catalytic domain has an additional DNA-binding interface that enhances enzymatic activity and liquid-phase condensation. *Proceedings of the National Academy of Sciences* 201905013 (2019).

31. Ergun, S. L., Fernandez, D., Weiss, T. M. & Li, L. STING Polymer Structure Reveals Mechanisms for Activation, Hyperactivation, and Inhibition. *Cell* **178**, 290-301.e10 (2019).

32. Shang, G., Zhang, C., Chen, Z. J., Bai, X.-C. & Zhang, X. Cryo-EM structures of STING reveal its mechanism of activation by cyclic GMP–AMP. *Nature* **567**, 389–393 (2019).

33. Zhang, C. *et al.* Structural basis of STING binding with and phosphorylation by TBK1. *Nature* **567**, 394–398 (2019).

34. Zhao, B. *et al.* A conserved PLPLRT/SD motif of STING mediates the recruitment and activation of TBK1. *Nature* **569**, 718–722 (2019).

35. Margolis, S. R., Wilson, S. C. & Vance, R. E. Evolutionary Origins of cGAS-STING Signaling. *Trends Immunol.* **38**, 733–743 (2017).

36. Gui, X. *et al.* Autophagy induction via STING trafficking is a primordial function of the cGAS pathway. *Nature* **567**, 262–266 (2019).

37. Yamashiro, L. H. *et al.* Interferon-independent STING signaling promotes resistance to HSV-1 in vivo. *Nat. Commun.* **11**, 3382 (2020).

38. Wu, J., Dobbs, N., Yang, K. & Yan, N. Interferon-Independent Activities of Mammalian STING Mediate Antiviral Response and Tumor Immune Evasion. *Immunity* **53**, 115-126.e5 (2020).

39. de Oliveira Mann, C. C. *et al.* Modular Architecture of the STING C-Terminal Tail Allows Interferon and NF-κB Signaling Adaptation. *Cell Rep.* **27**, 1165-1175.e5 (2019).

40. Ablasser, A. *et al.* Cell intrinsic immunity spreads to bystander cells via the intercellular transfer of cGAMP. *Nature* **503**, 530 (2013).

41. Gentili, M. *et al.* Transmission of innate immune signaling by packaging of cGAMP in viral particles. *Science* **349**, 1232–1236 (2015).

42. Bridgeman, A. *et al.* Viruses transfer the antiviral second messenger cGAMP between cells. *Science* **349**, 1228–1232 (2015).

43. Marcus, A. *et al.* Tumor-Derived cGAMP Triggers a STING-Mediated Interferon Response in Non-tumor Cells to Activate the NK Cell Response. *Immunity* **49**, 754-763.e4 (2018).

44. Carozza, J. A. *et al.* Extracellular cGAMP is a cancer-cell-produced immunotransmitter involved in radiation-induced anticancer immunity. *Nature Cancer* **1**, 184–196 (2020).

45. Luteijn, R. D. *et al.* SLC19A1 transports immunoreactive cyclic dinucleotides. *Nature* **573**, (2019).

46. Ritchie, C., Cordova, A. F., Hess, G. T., Bassik, M. C. & Li, L. SLC19A1 Is an Importer of the Immunotransmitter cGAMP. *Mol. Cell* **75**, 372-381.e5 (2019).

47. Zhou, C. *et al.* Transfer of cGAMP into Bystander Cells via LRRC8 Volume-Regulated Anion Channels Augments STING-Mediated Interferon Responses and Anti-viral Immunity. *Immunity* **52**, 767-781.e6 (2020).

48. Lahey, L. J. *et al.* The LRRC8A:C Heteromeric Channel Is a cGAMP Transporter and the Dominant cGAMP Importer in Human Vasculature Cells. *BioRxiv* (2020).

49. Zhou, Y. *et al.* Blockade of the Phagocytic Receptor MerTK on Tumor-Associated Macrophages Enhances P2X7R-Dependent STING Activation by Tumor-Derived cGAMP. *Immunity* **52**, 357-373.e9 (2020).

50. Li, L. *et al.* Hydrolysis of 2′3′-cGAMP by ENPP1 and design of nonhydrolyzable analogs. *Nat. Chem. Biol.* **10**, 1043 (2014).

51. Kato, K. *et al.* Structural insights into cGAMP degradation by Ecto-nucleotide pyrophosphatase phosphodiesterase 1. *Nat. Commun.* **9**, 4424 (2018).

52. Eaglesham, J. B., Pan, Y., Kupper, T. S. & Kranzusch, P. J. Viral and metazoan poxins are cGAMP-specific nucleases that restrict cGAS–STING signalling. *Nature* **566**, 259–263 (2019).

53. Gao, D. *et al.* Cyclic GMP-AMP Synthase Is an Innate Immune Sensor of HIV and Other Retroviruses. *Science* **341**, 903–906 (2013).

54. Li, X.-D. *et al.* Pivotal Roles of cGAS-cGAMP Signaling in Antiviral Defense and Immune Adjuvant Effects. *Science* **341**, 1390–1394 (2013).

55. Wu, J.-J. *et al.* Inhibition of cGAS DNA Sensing by a Herpesvirus Virion Protein. *Cell Host Microbe* **18**, 333–344 (2015).

56. Zhang, G. *et al.* Cytoplasmic isoforms of Kaposi sarcoma herpesvirus LANA recruit and antagonize the innate immune DNA sensor cGAS. *Proceedings of the National Academy of Sciences* **113**, E1034–E1043 (2016).

57. Huang, Z.-F. *et al.* Human Cytomegalovirus Protein UL31 Inhibits DNA Sensing of cGAS to Mediate Immune Evasion. *Cell Host Microbe* **24**, 69-80.e4 (2018).

58. Zhang, J. *et al.* Species-Specific Deamidation of cGAS by Herpes Simplex Virus UL37 Protein Facilitates Viral Replication. *Cell Host Microbe* **24**, 234-248.e5 (2018).

59. Ma, Z. *et al.* Modulation of the cGAS-STING DNA sensing pathway by gammaherpesviruses. *Proceedings of the National Academy of Sciences* **112**, E4306–E4315 (2015).

60. Lau, L., Gray, E. E., Brunette, R. L. & Stetson, D. B. DNA tumor virus oncogenes antagonize the cGAS-STING DNA-sensing pathway. *Science* **350**, 568 (2015).

61. Hancks, D. C., Hartley, M. K., Hagan, C., Clark, N. L. & Elde, N. C. Overlapping Patterns of Rapid Evolution in the Nucleic Acid Sensors cGAS and OAS1 Suggest a Common Mechanism of Pathogen Antagonism and Escape. *PLoS Genet.* **11**, e1005203 (2015).

62. Ni, G., Ma, Z. & Damania, B. cGAS and STING: At the intersection of DNA and RNA virus-sensing networks. *PLoS Pathog.* **14**, e1007148 (2018).

63. Zhou, W. *et al.* Structure of the Human cGAS–DNA Complex Reveals Enhanced Control of Immune Surveillance. *Cell* **174**, 300-311.e11 (2018).

64. Barnett, K. C. *et al.* Phosphoinositide Interactions Position cGAS at the Plasma Membrane to Ensure Efficient Distinction between Self- and Viral DNA. *Cell* **176**, 1432-1446.e11 (2019).

65. Liu, H. *et al.* Nuclear cGAS suppresses DNA repair and promotes tumorigenesis. *Nature* **563**, 131–136 (2018).

66. Gentili, M. *et al.* The N-Terminal Domain of cGAS Determines Preferential Association with Centromeric DNA and Innate Immune Activation in the Nucleus. *Cell Rep.* **26**, 2377-2393.e13 (2019).

67. Zierhut, C. *et al.* The Cytoplasmic DNA Sensor cGAS Promotes Mitotic Cell Death. *Cell* **178**, 302-315.e23 (2019).

68. Volkman, H. E., Cambier, S., Gray, E. E. & Stetson, D. B. Tight nuclear tethering of cGAS is essential for preventing autoreactivity. *Elife* **8**, (2019).

69. Ishii, K. J. *et al.* A Toll-like receptor–independent antiviral response induced by double-stranded B-form DNA. *Nat. Immunol.* **7**, 40–48 (2006).

70. Stetson, D. B. & Medzhitov, R. Recognition of Cytosolic DNA Activates an IRF3-Dependent Innate Immune Response. *Immunity* **24**, 93–103 (2006).

71. Li, T. & Chen, Z. J. The cGAS–cGAMP–STING pathway connects DNA damage to inflammation, senescence, and cancer. *J. Exp. Med.* **215**, 1287–1299 (2018).

72. Gao, P. *et al.* Cyclic [G(2′,5′)pA(3′,5′)p] Is the Metazoan Second Messenger Produced by DNA-Activated Cyclic GMP-AMP Synthase. *Cell* **153**, 1094–1107 (2013).

73. Corrales, L. *et al.* Direct Activation of STING in the Tumor Microenvironment Leads to Potent and Systemic Tumor Regression and Immunity. *Cell Rep.* **11**, 1018–1030 (2015).

74. Corrales, L., McWhirter, S. M., Dubensky, T. W. & Gajewski, T. F. The host STING pathway at the interface of cancer and immunity. *J. Clin. Invest.* **126**, 2404–2411 (2016).

75. Zaver, S. A. & Woodward, J. J. Cyclic dinucleotides at the forefront of innate immunity. *Curr. Opin. Cell Biol.* **63**, 49–56 (2020).

76. Hou, Z. & Matherly, L. H. Biology of the Major Facilitative Folate Transporters SLC19A1 and SLC46A1. in 175–204 (2014).

77. Zhao, R., Diop-Bove, N., Visentin, M. & Goldman, I. D. Mechanisms of Membrane Transport of Folates into Cells and Across Epithelia. *Annu. Rev. Nutr.* **31**, 177–201 (2011).

78. Henderson, G. B. & Zevely, E. M. Structural requirements for anion substrates of the methotrexate transport system in L1210 cells. *Arch. Biochem. Biophys.* **221**, 438–446 (1983).

79. Goldman, I. D. The characteristics of the membrane transport of amethopterin and the naturally occurring folates. *Ann. N. Y. Acad. Sci.* **186**, 400–422 (1971).

80. Yang, C. H., Sirotnak, F. M. & Dembo, M. Interaction between anions and the reduced folate/methotrexate transport system in L1210 cell plasma membrane vesicles: Directional symmetry and anion specificity for differential mobility of loaded and unloaded carrier. *J. Membr. Biol.* **79**, 285–292 (1984).

81. Goldman, I. D., Lichtenstein N S & Oliverio V T. Carrier-mediated transport of the folic acid analogue, methotrexate, in the L1210 leukemia cell. *J. Biol. Chem.* **243**, 5007–5017 (1968).

82. Lin, R., Heylbroeck, C., Genin, P., Pitha, P. M. & Hiscott, J. Essential Role of Interferon Regulatory Factor 3 in Direct Activation of RANTES Chemokine Transcription. *Mol. Cell. Biol.* **19**, 959–966 (1999).

83. Brownell, J. *et al.* Direct, Interferon-Independent Activation of the CXCL10 Promoter by NF- B and Interferon Regulatory Factor 3 during Hepatitis C Virus Infection. *J. Virol.* **88**, 1582–1590 (2014).

84. Jansen, G. *et al.* Sulfasalazine is a potent inhibitor of the reduced folate carrier: Implications for combination therapies with methotrexate in rheumatoid arthritis. *Arthritis & Rheumatism* **50**, 2130–2139 (2004).

85. Goldman, I. D. A model system for the study of heteroexchange diffusion: Methotrexate-folate interactions in L1210 leukemia and Ehrlich ascites tumor cells. *Biochimica et Biophysica Acta (BBA) - Biomembranes* **233**, 624–634 (1971).

86. Henderson, G. B., Grzelakowska-Sztabert, B., Zevely, E. M. & Huennekens, F. M. Binding properties of the 5-methyltetrahydrofolate/methotrexate transport system in L1210 cells. *Arch. Biochem. Biophys.* **202**, 144–149 (1980).

87. Plosker, G. L. & Croom, K. F. Sulfasalazine. *Drugs* **65**, 1825–1849 (2005).

88. Kozuch, P. L. & Hanauer, S. B. Treatment of inflammatory bowel disease: A review of medical therapy. *World J. Gastroenterol.* **14**, 354 (2008).

89. Rajitha, P., Biswas, R., Sabitha, M. & Jayakumar, R. Methotrexate in the Treatment of Psoriasis and Rheumatoid Arthritis: Mechanistic Insights, Current Issues and Novel Delivery Approaches. *Curr. Pharm. Des.* **23**, (2017).

90. Ahn, J., Son, S., Oliveira, S. C. & Barber, G. N. STING-Dependent Signaling Underlies IL-10 Controlled Inflammatory Colitis. *Cell Rep.* **21**, 3873–3884 (2017).

91. van de Weijer, M. L. *et al.* A high-coverage shRNA screen identifies TMEM129 as an E3 ligase involved in ER-associated protein degradation. *Nat. Commun.* **5**, 3832 (2014).

92. Zhao, R. *et al.* Impact of the Reduced Folate Carrier on the Accumulation of Active Thiamin Metabolites in Murine Leukemia Cells. *J. Biol. Chem.* **276**, 1114–1118 (2001).

93. Zhao, R., Gao, F. & Goldman, I. D. Reduced folate carrier transports thiamine monophosphate: an alternative route for thiamine delivery into mammalian cells. *American Journal of Physiology-Cell Physiology* **282**, C1512–C1517 (2002).

94. Visentin, M., Zhao, R. & Goldman, I. D. Augmentation of Reduced Folate Carrier-Mediated Folate/Antifolate Transport through an Antiport Mechanism with 5-Aminoimidazole-4-Carboxamide Riboside Monophosphate. *Mol. Pharmacol.* **82**, 209–216 (2012).

95. Henderson, G. B. & Zevely, E. M. Anion exchange mechanism for transport of methotrexate in L1210 cells. *Biochem. Biophys. Res. Commun.* **99**, 163–169 (1981).

96. Hamblett, K. J. *et al.* SLC46A3 Is Required to Transport Catabolites of Noncleavable Antibody Maytansine Conjugates from the Lysosome to the Cytoplasm. *Cancer Res.* **75**, 5329–5340 (2015).

97. van Diemen, F. R. *et al.* CRISPR/Cas9-Mediated Genome Editing of Herpesviruses Limits Productive and Latent Infections. *PLoS Pathog.* **12**, e1005701 (2016).

98. Horlbeck, M. A. *et al.* Compact and highly active next-generation libraries for CRISPR-mediated gene repression and activation. *Elife* **5**, (2016).

99. Kampmann, M., Bassik, M. C. & Weissman, J. S. Functional genomics platform for pooled screening and generation of mammalian genetic interaction maps. *Nat. Protoc.* **9**, 1825–1847 (2014).

100. Gilbert, L. A. *et al.* Genome-Scale CRISPR-Mediated Control of Gene Repression and Activation. *Cell* **159**, 647–661 (2014).

101. Kampmann, M., Bassik, M. C. & Weissman, J. S. Integrated platform for genome-wide screening and construction of high-density genetic interaction maps in mammalian cells. *Proceedings of the National Academy of Sciences* **110**, E2317–E2326 (2013).

102. Sadlish, H., Williams, F. M. R. & Flintoff, W. F. Functional Role of Arginine 373 in Substrate Translocation by the Reduced Folate Carrier. *J. Biol. Chem.* **277**, 42105–42112 (2002).

103. Huynh, T. N. *et al.* An HD-domain phosphodiesterase mediates cooperative hydrolysis of c-di-AMP to affect bacterial growth and virulence. *Proceedings of the National Academy of Sciences* **112**, E747–E756 (2015).

104. Sureka, K. *et al.* The Cyclic Dinucleotide c-di-AMP Is an Allosteric Regulator of Metabolic Enzyme Function. *Cell* **158**, 1389–1401 (2014).

105. Henderson, G. B. & Zevely, E. M. Affinity labeling of the 5-methyltetrahydrofolate/methotrexate transport protein of L1210 cells by treatment with an N-hydroxysuccinimide ester of [3H]methotrexate. *J. Biol. Chem.* **259**, 4558–4562 (1984).

106. McFarland, A. P. *et al.* Sensing of Bacterial Cyclic Dinucleotides by the Oxidoreductase RECON Promotes NF-κB Activation and Shapes a Proinflammatory Antibacterial State. *Immunity* **46**, 433–445 (2017).

107. Hall, J. *et al.* The catalytic mechanism of cyclic GMP-AMP synthase (cGAS) and implications for innate immunity and inhibition. *Protein Sci.* **26**, 2367–2380 (2017).

108. Mardjuki, R. E., Carozza, J. A. & Li, L. Development of cGAMP-Luc, a sensitive and precise coupled enzyme assay to measure cGAMP in complex biological samples. *J. Biol. Chem.* **295**, 4881–4892 (2020).

109. Bose, D., Su, Y., Marcus, A., Raulet, D. H. & Hammond, M. C. An RNA-Based Fluorescent Biosensor for High-Throughput Analysis of the cGAS-cGAMP-STING Pathway. *Cell Chemical Biology* **23**, 1539–1549 (2016).

110. Webb, M. R. A continuous spectrophotometric assay for inorganic phosphate and for measuring phosphate release kinetics in biological systems. *Proceedings of the National Academy of Sciences* **89**, 4884–4887 (1992).

111. Brune, M., Hunter, J. L., Corrie, J. E. T. & Webb, M. R. Direct, Real-Time Measurement of Rapid Inorganic Phosphate Release Using a Novel Fluorescent Probe and Its Application to Actomyosin Subfragment 1 ATPase. *Biochemistry* **33**, 8262–8271 (1994).

112. Surdo, N. C. *et al.* FRET biosensor uncovers cAMP nano-domains at β-adrenergic targets that dictate precise tuning of cardiac contractility. *Nat. Commun.* **8**, 15031 (2017).

113. Börner, S. *et al.* FRET measurements of intracellular cAMP concentrations and cAMP analog permeability in intact cells. *Nat. Protoc.* **6**, 427–438 (2011).

114. Calamera, G. *et al.* FRET-based cyclic GMP biosensors measure low cGMP concentrations in cardiomyocytes and neurons. *Communications Biology* **2**, 394 (2019).

115. Christen, M. *et al.* Asymmetrical Distribution of the Second Messenger c-di-GMP upon Bacterial Cell Division. *Science* **328**, 1295–1297 (2010).

116. Kulasekara, B. R. *et al.* c-di-GMP heterogeneity is generated by the chemotaxis machinery to regulate flagellar motility. *Elife* **2**, (2013).

117. Mills, E., Petersen, E., Kulasekara, B. R. & Miller, S. I. A direct screen for c-di-GMP modulators reveals a *Salmonella* Typhimurium periplasmic L-arginine–sensing pathway. *Sci. Signal.* **8**, ra57–ra57 (2015).

118. Christen, M. *et al.* Identification of Small-Molecule Modulators of Diguanylate Cyclase by FRET-Based High-Throughput Screening. *Chembiochem* **20**, 394–407 (2019).

119. Petersen, E., Mills, E. & Miller, S. I. Cyclic-di-GMP regulation promotes survival of a slow-replicating subpopulation of intracellular *Salmonella* Typhimurium. *Proceedings of the National Academy of Sciences* **116**, 6335–6340 (2019).

120. Dippel, A. B., Anderson, W. A., Park, J. H., Yildiz, F. H. & Hammond, M. C. Development of Ratiometric Bioluminescent Sensors for *in Vivo* Detection of Bacterial Signaling. *ACS Chem. Biol.* **15**, 904–914 (2020).

121. Roy, R., Hohng, S. & Ha, T. A practical guide to single-molecule FRET. *Nat. Methods* **5**, 507–516 (2008).

122. Rowland, C. E., Brown, C. W., Medintz, I. L. & Delehanty, J. B. Intracellular FRET-based probes: a review. *Methods and Applications in Fluorescence* **3**, 042006 (2015).

123. Shrestha, D., Jenei, A., Nagy, P., Vereb, G. & Szöllősi, J. Understanding FRET as a Research Tool for Cellular Studies. *Int. J. Mol. Sci.* **16**, 6718–6756 (2015).

124. Huang, Y.-H., Liu, X.-Y., Du, X.-X., Jiang, Z.-F. & Su, X.-D. The structural basis for the sensing and binding of cyclic di-GMP by STING. *Nat. Struct. Mol. Biol.* **19**, 728–730 (2012).

125. Chin, K.-H. *et al.* Novel c-di-GMP recognition modes of the mouse innate immune adaptor protein STING. *Acta Crystallogr. D Biol. Crystallogr.* **69**, 352–366 (2013).

126. Day, R. N., Booker, C. F. & Periasamy, A. Characterization of an improved donor fluorescent protein for Förster resonance energy transfer microscopy. *J. Biomed. Opt.* **13**, 031203 (2008).

127. Sun, Y. *et al.* Characterization of an orange acceptor fluorescent protein for sensitized spectral fluorescence resonance energy transfer microscopy using a white-light laser. *J. Biomed. Opt.* **14**, 054009 (2009).

128. Chen, X., Zaro, J. L. & Shen, W.-C. Fusion protein linkers: Property, design and functionality. *Adv. Drug Deliv. Rev.* **65**, 1357–1369 (2013).

129. Koshiba, T. & Chan, D. C. The Prefusogenic Intermediate of HIV-1 gp41 Contains Exposed C-peptide Regions. *J. Biol. Chem.* **278**, 7573–7579 (2003).

130. Roelofs, K. G., Wang, J., Sintim, H. O. & Lee, V. T. Differential radial capillary action of ligand assay for high-throughput detection of protein-metabolite interactions. *Proceedings of the National Academy of Sciences* **108**, 15528–15533 (2011).

131. Hall, J. *et al.* Discovery of PF-06928215 as a high affinity inhibitor of cGAS enabled by a novel fluorescence polarization assay. *PLoS One* **12**, e0184843 (2017).

132. Shin, K.-J. *et al.* A single lentiviral vector platform for microRNA-based conditional RNA interference and coordinated transgene expression. *Proceedings of the National Academy of Sciences* **103**, 13759–13764 (2006).

133. Shu, C., Yi, G., Watts, T., Kao, C. C. & Li, P. Structure of STING bound to cyclic di-GMP reveals the mechanism of cyclic dinucleotide recognition by the immune system. *Nat. Struct. Mol. Biol.* **19**, 722–724 (2012).

134. Collins, A. C. *et al.* Cyclic GMP-AMP Synthase Is an Innate Immune DNA Sensor for Mycobacterium tuberculosis. *Cell Host Microbe* **17**, 820–828 (2015).

135. Dey, B. *et al.* A bacterial cyclic dinucleotide activates the cytosolic surveillance pathway and mediates innate resistance to tuberculosis. *Nat. Med.* **21**, 401–406 (2015).

136. Ozawa, T., Kaihara, A., Sato, M., Tachihara, K. & Umezawa, Y. Split Luciferase as an Optical Probe for Detecting Protein−Protein Interactions in Mammalian Cells Based on Protein Splicing. *Anal. Chem.* **73**, 2516–2521 (2001).

137. Littmann, T., Ozawa, T., Hoffmann, C., Buschauer, A. & Bernhardt, G. A split luciferase-based probe for quantitative proximal determination of Gαq signalling in live cells. *Sci. Rep.* **8**, 17179 (2018).

138. Filonov, G. S. *et al.* Bright and stable near-infrared fluorescent protein for in vivo imaging. *Nat. Biotechnol.* **29**, 757–761 (2011).

139. Chu, J. *et al.* Non-invasive intravital imaging of cellular differentiation with a bright red-excitable fluorescent protein. *Nat. Methods* **11**, 572–578 (2014).

140. Bajar, B., Wang, E., Zhang, S., Lin, M. & Chu, J. A Guide to Fluorescent Protein FRET Pairs. *Sensors* **16**, 1488 (2016).

141. Witte, C. E. *et al.* Cyclic di-AMP Is Critical for Listeria monocytogenes Growth, Cell Wall Homeostasis, and Establishment of Infection. *MBio* **4**, (2013).

142. Whiteley, A. T. *et al.* c-di-AMP modulates *L isteria monocytogenes* central metabolism to regulate growth, antibiotic resistance and osmoregulation. *Mol. Microbiol.* **104**, 212–233 (2017).

143. Huynh, T. N. *et al.* Cyclic di-AMP targets the cystathionine beta-synthase domain of the osmolyte transporter OpuC. *Mol. Microbiol.* **102**, 233–243 (2016).

144. Townsley, L., Yannarell, S. M., Huynh, T. N., Woodward, J. J. & Shank, E. A. Cyclic di-AMP Acts as an Extracellular Signal That Impacts *Bacillus subtilis* Biofilm Formation and Plant Attachment. *MBio* **9**, (2018).

145. Gundlach, J. *et al.* Sustained sensing in potassium homeostasis: Cyclic di-AMP controls potassium uptake by KimA at the levels of expression and activity. *J. Biol. Chem.* **294**, 9605–9614 (2019).

146. Stülke, J. & Krüger, L. Cyclic di-AMP Signaling in Bacteria. *Annu. Rev. Microbiol.* **74**, annurev-micro (2020).

147. Krüger, L. *et al.* Two Ways To Convert a Low-Affinity Potassium Channel to High Affinity: Control of *Bacillus subtilis* KtrCD by Glutamate. *J. Bacteriol.* **202**, (2020).

148. McFarland, A. P. *et al.* RECON-Dependent Inflammation in Hepatocytes Enhances *Listeria monocytogenes* Cell-to-Cell Spread. *MBio* **9**, (2018).

149. Parvatiyar, K. *et al.* The helicase DDX41 recognizes the bacterial secondary messengers cyclic di-GMP and cyclic di-AMP to activate a type i interferon immune response. *Nat. Immunol.* **13**, (2012).

150. Huynh, T. N. & Woodward, J. J. Too much of a good thing: regulated depletion of c-di-AMP in the bacterial cytoplasm. *Curr. Opin. Microbiol.* **30**, 22–29 (2016).

151. Whiteley, A. T., Pollock, A. J. & Portnoy, D. A. The PAMP c-di-AMP Is Essential for Listeria monocytogenes Growth in Rich but Not Minimal Media due to a Toxic Increase in (p)ppGpp. *Cell Host Microbe* **17**, 788–798 (2015).

152. Pham, H. T. *et al.* Enhanced uptake of potassium or glycine betaine or export of cyclic-di-AMP restores osmoresistance in a high cyclic-di-AMP Lactococcus lactis mutant. *PLoS Genet.* **14**, e1007574 (2018).

153. Corrigan, R. M., Bowman, L., Willis, A. R., Kaever, V. & Gründling, A. Cross-talk between Two Nucleotide-signaling Pathways in *Staphylococcus aureus*. *J. Biol. Chem.* **290**, 5826–5839 (2015).

154. Kellenberger, C. A., Chen, C., Whiteley, A. T., Portnoy, D. A. & Hammond, M. C. RNA-Based Fluorescent Biosensors for Live Cell Imaging of Second Messenger Cyclic di-AMP. *J. Am. Chem. Soc.* **137**, 6432–6435 (2015).

155. Yang, J. *et al.* Deletion of the cyclic di-AMP phosphodiesterase gene (*cnpB*) in *M ycobacterium tuberculosis* leads to reduced virulence in a mouse model of infection. *Mol. Microbiol.* **93**, 65–79 (2014).

156. Manikandan, K. *et al.* Two-Step Synthesis and Hydrolysis of Cyclic di-AMP in Mycobacterium tuberculosis. *PLoS One* **9**, e86096 (2014).

157. He, Q. *et al.* Structural and Biochemical Insight into the Mechanism of Rv2837c from *Mycobacterium tuberculosis* as a c-di-NMP Phosphodiesterase. *J. Biol. Chem.* **291**, 3668–3681 (2016).

158. Tang, Q. *et al.* Functional Analysis of a c-di-AMP-specific Phosphodiesterase MsPDE from *Mycobacterium smegmatis*. *Int. J. Biol. Sci.* **11**, 813–824 (2015).

159. Latoscha, A. *et al.* c-di-AMP hydrolysis by the phosphodiesterase AtaC promotes differentiation of multicellular bacteria. *Proceedings of the National Academy of Sciences* **117**, 7392–7400 (2020).

160. Pollock, A. J., Zaver, S. A. & Woodward, J. J. A STING-based biosensor affords broad cyclic dinucleotide detection within single living eukaryotic cells. *Nat. Commun.* **11**, 3533 (2020).

161. Gibhardt, J. *et al.* An extracytoplasmic protein and a moonlighting enzyme modulate synthesis of c-di-AMP in *Listeria monocytogenes*. *Environ. Microbiol.* **22**, 2771–2791 (2020).

162. Tosi, T. *et al.* Inhibition of the Staphylococcus aureus c-di-AMP cyclase DacA by direct interaction with the phosphoglucosamine mutase GlmM. *PLoS Pathog.* **15**, e1007537 (2019).

163. de Oliveira Mann, C. C., Kiefersauer, R., Witte, G. & Hopfner, K.-P. Structural and biochemical characterization of the cell fate determining nucleotidyltransferase fold protein MAB21L1. *Sci. Rep.* **6**, 27498 (2016).

164. Kujirai, T. *et al.* Structural basis for the inhibition of cGAS by nucleosomes. *Science* (2020) doi:10.1126/science.abd0237.

165. Zhao, B. *et al.* The Molecular Basis of Tight Nuclear Tethering and Inactivation of cGAS. *Nature* 1–8 (2020).

166. Pathare, G. R. *et al.* Structural mechanism of cGAS inhibition by the nucleosome. *Nature* (2020) doi:10.1038/s41586-020-2750-6.

167. Michalski, S. *et al.* Structural basis for sequestration and autoinhibition of cGAS by chromatin. *Nature* (2020) doi:10.1038/s41586-020-2748-0.